Fakultät Maschinenbau
fortschritt studieren

RUHR
UNIVERSITÄT
BOCHUM

RUB

Absolute Electrode Potentials
The Thin Film Electrode

Dissertation

zur

Erlangung des Grades
Doktor-Ingenieur

der

Fakultät für Maschinenbau
Ruhr-Universität Bochum

von

Philipp Kerger
aus Saarbrücken

Bochum 2019

Dissertation eingereicht am: 12.11.2019

Tag der mündlichen Prüfung: 16.12.2019

Erstgutachter: PD Dr. Michael Rohwerder

Zweitgutachter: Prof. Dr. Martin Stratmann

Angefertigt

am

Max-Planck Institut für Eisenforschung GmbH

Düsseldorf 2019

Acknowledgments

First and foremost, I would like to thank my supervisor PD Dr. Michael Rohwerder for his guidance and deep interest in my work. I am grateful for our numerous discussions and the great balance between advice and giving abundant freedom to pursue own ideas. I am obliged to him for his support during my time at the Lawrence Berkeley National Laboratory, where I got the chance to come into contact with leading experts in the field of APXPS. In this context, I want to thank Dr. Hendrik Bluhm for giving me the chance to be part of his pioneering group at the Advanced Light Source.

I also thank Prof. Dr. Martin Stratmann who admitted me as a doctoral candidate and agreed to be assessor of my examination committee besides his main occupation as president of the Max-Planck Society.

Furthermore I am thankful to Alexandra and Dirk Vogel, Eberhard Heinen, Petra Ebbinghaus, Dr. Qingyun Hu, Dr. Thomas Utzig, Cauê Corrêa da Silva, Cristiano Giesbrecht Kasdorf, Stefan Evers, Dr. Chun-Hung Wu, Prof. Dr. Andreas Erbe, Jürgen Wichert, Brigitte Kohlhaas, who all contributed to this work individually and helped me to write this work.

Especially I want to thank Daniel Göhl and Dr. Aleksandar Zeradjanin for sharing their profound scientific expertise and patience in discussing fundamental electrochemical questions.

Last but not least, I express my humble regards to my family and friends for their unconditional support and unlimited encouragement throughout all stages.

Contents

Symbols & Constants

Table 1: Main Symbols

Symbol	Meaning	SI Unit
A	area	m^2
a	activity	
C	capacity	F
d_S	specific surface dipole moment	$C\ m^{-1}$
E	energy	J
E_F	*Fermi level*	J
E_V	vacuum reference level	J
E_O	outer reference level	J
F	*Helmholtz* free energy	J or $J\ mol^{-1}$
f	fugacity	
G	*Gibbs* free energy	J or $J\ mol^{-1}$
H	enthalpy	J or $J\ mol^{-1}$
I	intensity	
i	electrical current	A
j	current density	$A\ m^{-2}$
K, k	equilibrium constant	
m	mass	kg
N	number of particles	
n	number of particles in mole	mol
p	pressure	Pa

Continued on next page

Table 1 – *Continued from previous page*

Symbol	Description	SI Unit
Q	charge	C
r	radius or distance	m
S_p	pumping speed	$m^3\ s^{-1}$
k	equilibrium constant	
T	temperature	K
t	time	s
U	inner energy	J or $J\ mol^{-1}$
V	volume	m^3
v	speed	$m\ s^{-1}$
x	mole fraction	
z	multiple of the elementary charge	
α	*real potential*	V
γ	activity coefficient	
λ	vacancy parameter	
ϵ	electrode potential	J
ε_r	relative permittivity of a medium	
μ	chemical potential	J or $J\ mol^{-1}$
ϱ	number density	m^{-3}
σ	cross section	m^2
τ	permeation rate of a leak	$Pa\ m^3\ s^{-1}$
$\bar{\mu}$	electrochemical potential	J or $J\ mol^{-1}$
ν	photon frequency	J
φ	*Galvani-* or inner potential	V
χ	surface potential	V

Continued on next page

Table 1 – *Continued from previous page*

Symbol	Description	SI Unit
ψ	*Volta*- or outer potential	V
ω	angular frequency	s^{-1}
Γ	area normalized desorption rate	$Pa\ m\ s^{-1}$
Λ	interfacial surface excess	m^{-2}
Φ	work function	J

Table 2: Physical & Mathematical constants

Symbol	Meaning	SI Unit
e	elementary charge	C
ε_o	vacuum permittivity or electric constant	$F\ m^{-1}$
F	*Farady* constant	$C\ mol^{-1}$
h	*Planck* constant	$J\ s$
$\hbar$	*Planck* constant, $h\ (2\pi)^{-1}$	$J\ s$
k_B	*Boltzmann* constant	$J\ K^{-1}$
m_e	mass of an electron at rest	kg
R	gas constant	$J\ mol^{-1}\ K^{-1}$
r_{Bohr}	*Bohr* radius	m
π	*Archimedes'* constant or pi	

Abbreviations

Table 3: Abbreviations

Abbreviations	**Full Name**
abs	absolute (electrode potential)
ab	absorbed or absorption
ad	adsorbed or adsorption
APXPS	Ambient Pressure X-Ray Photoelectron Spectroscopy
b	binding (energy)
CE	Counter Electrode
CV	Cyclic Voltammogram
D	Detector
EE	Emersed Electrode
ESCA	Electron Spectroscopy for Chemical Analysis
e	electron
F	*Fermi* (level)
FWHM	Full Width at Half Maximum
g	gas (phase)
GND	Ground (electricity)
IMFP	Inelastic Mean Free Path
IRRAS	Infrared Reflection-Absorption Spectroscopy
k	kinetic (energy)
KP	*Kelvin* Probe
l	liquid (phase)

Continued on next page

Table 3 – *Continued from previous page*

Abbreviations	**Full Name**
MFP	Mean Free Path
M	Metal (electrode)
max	maximum
min	minimum
NP	Number Density
OCP	Open-Circuit Potential
PES	Photoelectron Spectroscopy
RE	Reference Electrode
RHE	Reversible Hydrogen Electrode
RT	Room Temperature
S	Solution
SA	Sample
SGL	Single Layer Graphene
SHE	Standard Hydrogen Electrode
TC	Thermodynamic Cycle
UHV	Ultra-High Vacuum
UPS	Ultraviolet Photoelectron Spectroscopy
WE	Working Electrode
WF	Work Function
XAS	X-ray Absorption Spectroscopy
XPS	X-ray Photoelectron Spectroscopy

Chapter 1

Abstract

The interface is of central importance in many key technologies such as batteries, fuel cells, catalysis, and sensors that mediates device's functionality by chemical composition and structure. Probing the interface requires methods with atomic surface sensitivity. Usually such methods are restricted to operate in ultra-high vacuum (UHV). On the one hand, a surface exposed to UHV constitutes a strict framework, indispensable for targeted exploration, on the other hand, UHV is far removed from reality *in operando*. This dilemma, known as the *pressure gap*, is bridged by the recent development of the *ambient pressure x-ray photoelectron spectroscopy* (APXPS). Therewith, the *pressure gap* narrows about 25 *mbar* and enables *in situ/operando* analyses of the (solid|liquid|gas) interface. Another difficulty in probing interfaces, i.e. an electrode covered with an electrolyte layer, is the loss of surface sensitivity for the (solid|liquid) interface since it is buried under a thick layer of electrolyte. To reveal the (solid|liquid) interface, electrodes covered with just an ultra-thin layer electrolyte are required. In the present thesis a completely new approach is introduced: the *thin film electrode*. For the first time a fully controllable electrode is made accessible to direct absolute electrode potential measurements as well as chemical analysis by means of APXPS. As the first application, the hydrogen electrode will be investigated and correlated to applied-, standard-, and absolute potentials with chemical analysis. The results comprise a value of the absolute electrode potential under standard conditions and the observation of catalytic CO_2/CO reduction.

Chapter 2

Introduction

2.1 Chemical Potential

In classical thermodynamics, the chemical potential μ_i of an electrical neutral particle of the i-th component is the energy required to move a partial number of the corresponding particle from a reference state to the inner of an ensemble of particles. The thermodynamic potentials are the *Gibbs* free energy G, the *Helmholtz* free energy F, the enthalpy H, and the internal energy U. The chemical potential is obtained from the differentials in Eq. 2.1 to 2.4 [1]. The independent variables are the entropy S, temperature T, volume V, pressure p, and the number n of particles in mole.

$$dG = -SdT + Vdp + \sum_i \mu_i dn_i \tag{2.1}$$

$$dF = -SdT - pdV + \sum_i \mu_i dn_i \tag{2.2}$$

$$dH = TdS + Vdp + \sum_i \mu_i dn_i \tag{2.3}$$

$$dU = TdS - pdV + \sum_i \mu_i dn_i \tag{2.4}$$

Even though different thermodynamic potentials are used, equivalent expressions for the chemical potential are obtained [2]. In practice, the *Gibbs* free energy is commonly used, since it is easier to hold an ensemble of particles at constant pressure and temperature than at constant volume or entropy,

see subscripts of Eq. 2.5 to 2.8.

$$\mu_i = \left(\frac{\partial G}{\partial n_i}\right)_{p,T,n_{j\neq i}} \tag{2.5}$$

$$= \left(\frac{\partial F}{\partial n_i}\right)_{V,T,n_{j\neq i}} \tag{2.6}$$

$$= \left(\frac{\partial H}{\partial n_i}\right)_{S,p,n_{j\neq i}} \tag{2.7}$$

$$= \left(\frac{\partial U}{\partial n_i}\right)_{S,V,n_{j\neq i}} \tag{2.8}$$

For an ideal gas i [1] at the pressure p_i and the gas constant R, the chemical potential is given by

$$\mu_i = \mu_i^0 + RTln\left(\frac{p_i}{p_i^0}\right), \tag{2.9}$$

while μ_i^0 and p_i^0 represent an arbitrary reference state. Equilibrium is obtained when the chemical potential of the different components are identical [1, 3]. Thus, in a system with the phases I and II, equilibrium is reached when

$$\mu_i(I) = \mu_i(II) \tag{2.10}$$

is established. Considering the equilibrium of a liquid (l) and its gas (g) of the pure component i at p_i^*, the chemical potential is

$$\mu_i(l) = \mu_i(g) = \mu_i^{0*}(l) + RTln\left(\frac{p_i}{p_i^{0*}}\right), \tag{2.11}$$

while the pure component is chosen as the reference state[1] [1]. According to *Raoult's* law; $p_i/p_o^{0*} = x_i$, the chemical potential of the liquid is

$$\mu_i(l) = \mu_i^{0*}(l) + RTln\left(x_i\right). \tag{2.12}$$

[1] 1 atmosphere.

Under reference conditions, the mole fraction becomes $x_i = 1$, which is fulfilled for $p_i = p_o^{0*}$. So far, it was assumed that particles behave ideally; meaning that an ideal gaseous substance has no interaction and an ideal liquid substance has same interactions, but not no interaction. Real substances [1] behave differently which require the introduction of the activity a and the activity coefficient γ as defined in Eq. 2.13.

$$a_i = \gamma_i x_i \tag{2.13}$$

For a real liquid, where $\gamma \neq 1$ [1], the general expression for the chemical potential of a liquid is

$$\mu_i(l) = \mu_i^{0*}(l) + RTln(a_i). \tag{2.14}$$

With the same concept but using the fugacity f_i [1], the general expression for the chemical potential of a gas is

$$\mu_i(g) = \mu_i^{0*}(g) + RTln(f_i). \tag{2.15}$$

2.2 Electrochemical Potential

In the case that a particle carries an electrostatic charge as a multiple[2] z_i of the elementary charge e, the term $z_i F\varphi$, with the *Faraday* constant F and the electrostatic potential φ, is added to the chemical potential μ_i [1], giving the electrochemical potential in molar units to:

$$\bar{\mu}_i = \mu_i + z_i F\varphi \tag{2.16}$$

2.3 Electrochemical Potential of Free Electrons

In solid-state, a body with the volume V, containing N_e electrons, each with the effective mass m_e^* of a free electron, the maximum energy of free electrons

[2]For one electron: $z_e = -1$.

is defined by the *Fermi level*, given by Eq. 2.17 [4].

$$E_F = \frac{\hbar^2}{2m_e^*} \left(3\pi^2 \varrho\right)^{2/3}, \varrho = N_e/V \tag{2.17}$$

The number of the electron eigenstates per volume within a certain energy range is the density function $D(E)$, which scales with the square root of the energy, Eq. 2.18 [4].

$$D(E) = \frac{1}{2\pi} \left(\frac{2m_e^*}{\hbar^2}\right)^{3/2} E^{1/2} \tag{2.18}$$

At temperatures $T > 0\ K$, thermal energy in terms of $k_B T$ is transmitted to electrons, and eigenstates above the *Fermi level* are occupied. As a consequence, the same amount of unoccupied eigenstates below the *Fermi level* are formed. For that reason, the *Fermi level* is defined as the energy where half of the states are occupied. The probability density that an eigenstate is occupied by an electron at a certain temperature is given by the *Fermi function*, Eq. 2.19 [4].

$$f(E) = \frac{1}{exp\left(\frac{E-E_F}{k_B T}\right) + 1} \tag{2.19}$$

It follows that the electron density ϱ is obtained by:

$$\varrho = \int_0^\infty \varrho(E) dE = \int_0^\infty D(E) f(E) dE \tag{2.20}$$

If the density of electrons is known, Eq. 2.20 can be used to calculate the *Fermi level* $E_F(T)$. Schematically the above context is shown in Fig. 2.1. The thermodynamic meaning of the *Fermi level* becomes clear by reviewing Eq. 2.17: The *Fermi level* depends on the number of electrons, illustrated in Fig. 2.2. If N_e is increased about the difference ΔN_e, E_F is increased about the energy difference $E_F(N_e + \Delta N_e) - E_F(N_e)$, which is the meaning of the chemical potential in Eq. 2.5 to 2.8 when $E_F(N_e + \Delta N_e) - E_F(N_e)$ is divided

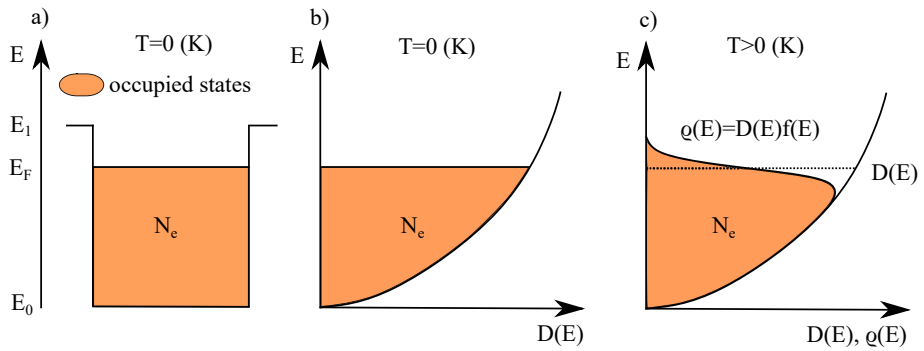

Figure 2.1: Energy states of free electrons at different temperatures: a) Electron in a potential well with the energy barrier of $|E_1 - E_0|$, for $T = 0\ K$. b) Density of states, for $T = 0\ K$. c) Density of states, for $T > 0\ K$. Adapted from e.g. [4].

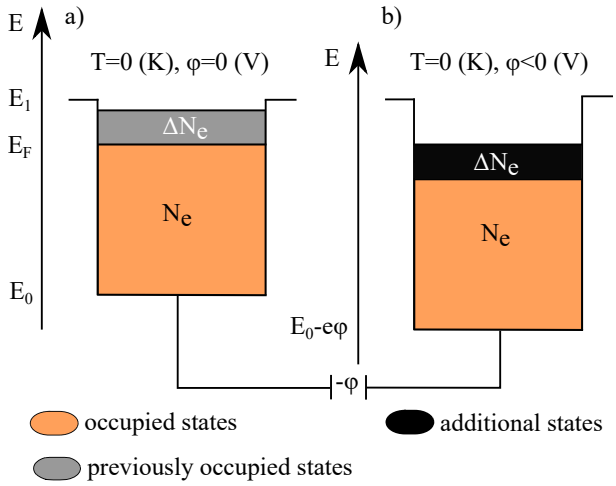

Figure 2.2: The *Fermi level* depends on the number of electrons N_e. Decreasing the potential well about $-e\varphi$ leads to a spill of electrons from a) to b) until the *Fermi levels* are balanced. Adapted from e.g. [4].

by ΔN_e and considered for small values of ΔN_e. Hence, the *Fermi level* is the chemical potential. When the potential well is decreased about $-e\varphi$, the *Fermi level* of the original electron ensemble is lowered. Thus, affects the electrochemical potential, as given for one mole of electrons by Eq. 2.21.

$$\bar{\mu}_e = \mu_e + z_e F\varphi = E_F + z_e F\varphi \tag{2.21}$$

2.4 Galvani Potential

The electrostatic potential φ, considered as the *Galvani-* or inner potential is the inner potential of a phase [5, 6, 7, 8]. The electrical work[3] to move a test charge e from the vacuum at infinity to the inner of the phase is $-e\varphi$. In approaching the inner of the phase, individual contributions can be separated: the inner potential consists of the *Volta* potential, also called the outer potential ψ, and the surface potential χ:

$$\varphi = \psi + \chi \tag{2.22}$$

If the phase is electrically charged ($\psi \neq 0$), the work $-e\psi$ is required to move a test charge right before it enters the interior of the phase. The location, denoted as *just outside* the phase, is set to 10^{-4} *cm* right above the surface in order to avoid electrostatic influence [9, 8]. For a known geometry the outer potential can be calculated. A sphere, carrying the charge Q, the outer potential $\psi_\circ(r)$ at a distance r outside the sphere is given by Eq. 2.23, where ε_0 is the vacuum permittivity.

$$\psi_\circ(r) = \frac{1}{4\pi\varepsilon_0}\frac{Q}{r} \tag{2.23}$$

The surface potential, which exists as a double layer at phase boundaries [7] like (metal|vacuum) or (metal|liquid), requires the work $-e\chi$ to transmit the test charge e, from the location right above the surface, to the interior of the phase.

[3]Not the electrochemical work.

2.5 Reference levels for the Energy and Potential scale

Regarding the considerations of chapter 2.4, suitable reference levels to characterize different particle states on the same energy- or potential scale can be found. It applies that any reference level can be arbitrarily chosen. Its choice is only numerically motivated and the quality of the reference level is rated with regard to its practicability. Since the focus is on electronic states, the test charge of an electron and its chemical entity, e.g. a proton, are used to identify possible reference levels.

The electron at zero potential in rest state at infinity

At this reference level an electron is at rest, unlocated[4] in vacuum at infinity [10, 11], unaffected by an electrical field. This state is associated with the physical zero energy and denoted as $E_V = 0$. Despite of minor importance in applications, it has a fundamental meaning in a theoretical framework.

The electron in a defined potential at rest state

For experimental reasons, in many cases it is not possible to achieve the reference state of E_V. In that case, one may use a reference level that exerts a specific potential on the test charge. From chapter 2.4, such a reference level is given by the outer potential, which is defined as the energy level E_O right before an electron enters the interior of a phase [9, 8] and experiences the full impact of the surface potential. In the case that $\psi = 0$, it follows that $E_O = E_V$.

Chemical entities at defined activities

In electrochemistry, reference electrodes are widely established and

[4] In order to have a defined energy.

measure the potential of an electrode with respect to itself. A stable reference potential is obtained for a redox system in thermodynamic equilibrium which requires constant temperature, fugacitiy and activity of the involved species.

2.6 Identifying the Reference Levels of a Single Electrode

For a test charge e, the required work[5] to transfer e from a defined reference level to the inner of a phase is the electrochemical potential (Eq. 2.21), as shown in Fig. 2.3. The electrochemical potential can be divided into the chemical work μ_e and the electrical work $-e\varphi$, for which the latter splits into the contributions of $-e\psi$ and $-e\chi$. Considering the case of a charged electrode, Fig. 2.3 a), additional[6] electrical work $-e\psi$ is required to add the test charge to the inner of the phase. Thereby, $-e\psi$ is the contribution from the reference level E_V to E_O, see Fig. 2.3 a), b). The remaining work to transfer the test charge from E_O to E_F is $-e\chi$ and μ_e, introduced as the *real potential* α_e [10]. Thus, the electrochemical potential can be written as

$$\bar{\mu}_e = \mu_e - z_e\chi - z_e\psi = \alpha_e - z_e\chi. \tag{2.24}$$

In contrast to electrochemical practice, the physical terminology of the *real potential* corresponds to the negative work function $-\Phi_O$, defined on the same energy level, i.e. Φ_O is obtained for extracting a test charge from the inner of the phase. Thus, Eq. 2.25 and 2.26 identify the reference level of E_O.

$$\alpha_e = -\Phi^O \tag{2.25}$$

$$\alpha_e = -\Phi^\infty - e\psi \tag{2.26}$$

[5]Strictly the electrochemical work.
[6]Referring the non-charged case.

For $-e\psi = 0$ - the non-charged electrode, it can be seen that Eq. 2.26 equals Eq. 2.25; meaning that the vacuum level at infinity coincides with the reference level of the outer potential, shown in Fig. 2.3 b).

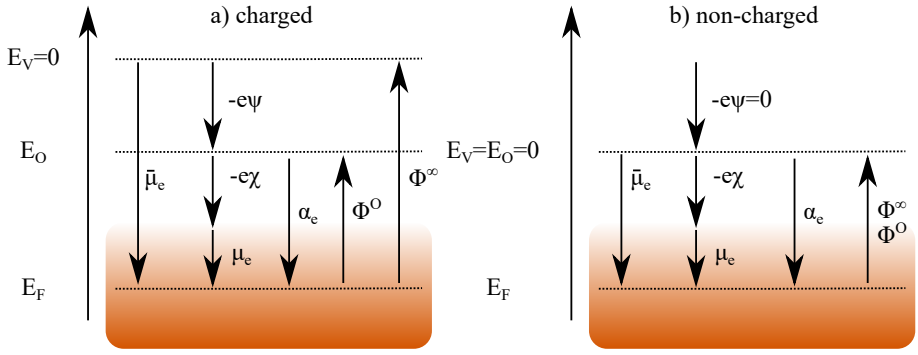

Figure 2.3: Quantities that describe the energy state of the test charge e relatively to a reference state: a) charged electrode; b) non-charged electrode. In case b): the vacuum reference level at infinity coincides with the reference level of the outer potential, denoted with $E_V = E_O$. The electrochemical potential $\bar{\mu}_e$, chemical potential μ_e, outer potential ψ, surface potential χ, *real potential* α_e, work function Φ^O for E_O, and work function Φ^∞ for E_V.

In terms of the electrochemial potential, the non-charged- and charged electrode becomes to:

$$\bar{\mu}_e = \alpha_e \ (non - charged) \tag{2.27}$$

$$\bar{\mu}_e = \alpha_e - e\psi \ (charged) \tag{2.28}$$

$$\bar{\mu}_e = -\Phi^\infty \ (charged) \tag{2.29}$$

Eq. 2.27 to 2.29 identify the reference level of E_V.

In summary: The *real* potential gives the energy independently from the extend of the charge. By contrast, the electrochemical potential gives the energy including the charge. On a physical basis, the corresponding work

function is the energy descriptor for a test charge of the single electrode, outlining the theoretical foundation of modern electrochemistry.

2.7 Electron Equilibrium

Taking two dislike single electrodes (A) and (B), Fig. 2.4, each having individual quantities that describe their energy states, and bringing them into electrical contact, a charge transfer from one to the other electrode is initiated until an electron transfer equilibrium is reached. Herein the transfer direction is determined from the higher (E_{FB}) to the lower (E_{FA}) *Fermi level*, Fig. 2.4. In electrochemial equilibrium, the *Fermi levels* are balanced, such that Eq. 2.30 is achieved by mutual electron and proton exchange.

$$\bar{\mu}_{eA} = \bar{\mu}_{eB} = \Phi_A^{\infty} = \Phi_B^{\infty} \tag{2.30}$$

The charge transfer evokes a negative polarization on electrode (A) and a positive polarization on electrode (B), see Fig. 2.4) b), resulting to a potential difference according to the difference of the outer potentials. From the equilibrium condition in Eq. 2.30, it follows that the outer potential difference is given by Eq. 2.31 and 2.32, illustrated with the red arrows in Fig. 2.4 b).

$$e\Delta\psi_{eA|B} = e\psi_{eA} - e\psi_{eB} = \alpha_{eB} - \alpha_{eA},\ equilibrium \tag{2.31}$$

$$e\Delta\psi_{eA|B} = \mu_{eA} - \mu_{eB},\ equilibrium \tag{2.32}$$

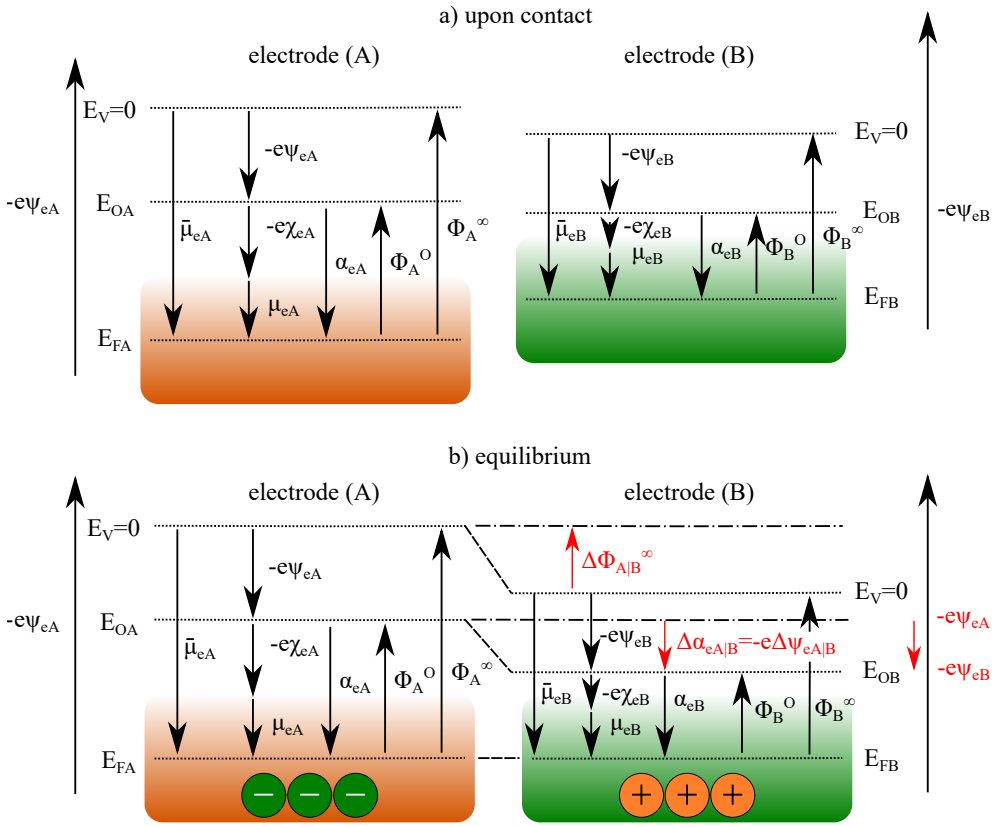

Figure 2.4: The electron transfer equilibrium of two dislike single electrodes (A) and (B): a) upon electrical contact, i.e. independent energy scale; b) in contact, while electron equilibrium is established, i.e. same energy scale.

2.8 The Absolute Electrode Potential

Important contributions to the concept of the absolute electrode were made by *Kanevsky* 1948/50/53 [12, 13, 14], *Parsons* 1954 [10] and 1985 in [15], *Bockris* 1968/83 [16, 17] *Frumkin* 1975/77 [18, 19], *Gomer* 1977 [20], *Kolb* 1981/87 in [21] and [22], *Gerischer* 1983 [23], *Reiss* 1985 [24], *Trasatti* 1986/90/91 [25, 11, 26], and *Hansen* 1987 [27].

Despite numerous attempts have been made to elaborate the definition of the absolute electrode potential,"*,...nobody seems seriously convinced of the*

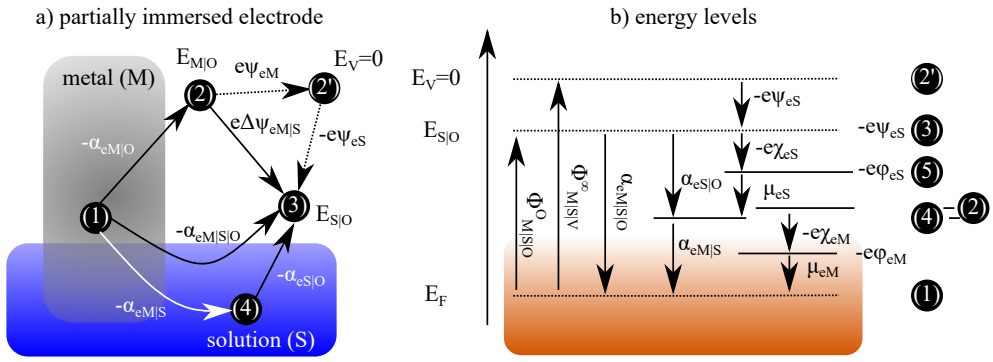

Figure 2.5: a) the partially immersed single electrode in equilibrium with the solution. a) location of energy levels in relation to the electrode and solution. b) energy levels corresponding to the locations in a). Location (5) cannot be drawn in a).

arguments of the others." [11]. It was Trasatti in [11] who clarified that four different absolute electrode potentials can be formulated, each originating from a different reference level.

Starting from the location (1) of the metal electrode (M) in Fig. 2.5 a), a test charge e can be moved from (1) to (3), also to any other location, principally on two different paths:

through the (metal|vacuum) interface: (1)→(2)(→ (2′)) →(3),

through the (metal|solution) interface: (1)→(3) or (1)→ (4)→ (3).

Where on the energy scale in Fig. 2.5 b) - (1) is the *Fermi level* of the metal (M) and the solution (S), (2) the reference level of (M) close to its surface, (2′) the common vacuum reference level at infinity of (M) and (S), (3) the vacuum reference level of (S) close to its surface [13, 28, 14, 18, 29, 19], (4) the free electron in the solution as the reference level [30, 11], and (5) the

inner potential of (S) as the reference level (not shown in Fig. 2.5 a)) [12, 16].

Since the test charge can be moved on a closed loop within a conservative field, the total work done in moving the test charge to (3) yields the same result on either path. Thus, moving on the path (1)→(3), the *real* potential is found by:

$$\alpha_{eM|S|O} = \alpha_{eM|S} + \alpha_{eS|O},\ (1) \rightarrow \mathbf{(3)}, \tag{2.33}$$

and on the path (1)→(2)→(3) by:

$$\alpha_{eM|S|O} = \alpha_{e|M|O} - e\Delta\psi_{eM|S},\ (1) \rightarrow (2) \rightarrow \mathbf{(3)} \tag{2.34}$$

Combining Eq. 2.33 and 2.34, one obtains the expression for $\alpha_{eM|S}$:

$$\alpha_{eM|S} = \alpha_{eM|O} - \alpha_{eS|O} - e\Delta\psi_{eM|S},\ (1) \rightarrow \mathbf{(4)} \tag{2.35}$$

Having identified $\alpha_{eM|S|O}$ and $\alpha_{eM|S}$, all other locations can be reached on any path, giving the Eq. 2.36 - 2.38[7].

$$\alpha_{eM|O} = \Phi^{\infty}_{M|S|V} - e\psi_{eM},\ (1) \rightarrow \mathbf{(2)} \tag{2.36}$$

$$\Phi^{\infty}_{M|S|V} = -\bar{\mu}_{eM} = -\alpha_{eM|O} + e\psi_{eM},\ (1) \rightarrow \mathbf{(2')} \tag{2.37}$$

$$e\varphi_{eS} = \Phi^{O}_{M|O}/e - \Phi^{O}_{S|O}/e - \mu_{eM},\ (1) \rightarrow \mathbf{(5)} \tag{2.38}$$

Since Eq. 2.33 - 2.38 represent energy levels on the absolute scale, having independently maintained their meaning from any other reference electrode, division by the elementary charge e results in a reference free absolute electrode potential ϵ_{abs}, Eq. 2.39.

$$\epsilon_{abs} = E_{abs}/e \tag{2.39}$$

[7]Eq. 2.38 is not obtained straight forward, see [11].

From this point of view, it is clear that Eq. 2.40 to 2.44 shall be considered as absolute electrode potentials.

$$\epsilon^{3}_{abs} = -\alpha_{eM|S|O}/e = \Phi^{O}_{M|O}/e + \Delta\psi_{eM|S},\ \textit{location}\ \textbf{(3)} \tag{2.40}$$

$$\epsilon^{4}_{abs} = \Phi^{O}_{M|O}/e + \Delta\psi_{eM|S} + \mu_{eS}/e - \chi_{eS},\ \textit{location}\ \textbf{(4)} \tag{2.41}$$

$$\epsilon^{2}_{abs} = \Phi^{O}_{M|O}/e,\ \textit{location}\ \textbf{(2)} \tag{2.42}$$

$$\epsilon^{2'}_{abs} = \Phi^{\infty}_{M|S|V}/e = -\bar{\mu}_{eM}/e = \Phi^{O}_{M|O}/e + \psi_{eM},\ \textit{location}\ \textbf{(2')} \tag{2.43}$$

$$\epsilon^{5}_{abs} = \Phi^{O}_{M|O}/e - \Phi^{O}_{S|O}/e - \mu_{eM},\ \textit{location}\ \textbf{(5)} \tag{2.44}$$

Of course, $\epsilon^{2'}_{abs}$ has a particular meaning with regard to *zero* energy[8] and the same in case of the non-charged electrode: $\epsilon^{2'}_{abs} = \epsilon^{2}_{abs} = \epsilon^{3}_{abs}$. However, as *Trasatti* concluded in [11]: the dominant question is which absolute electrode potential can experimentally be accessed? And further, how precise can it be measured; e.g. measuring ϵ^{3}_{abs} at the location (3), but far away from the electrode [27] should give approximately the same numerical value as $\epsilon^{2'}_{abs}$. Thus, the question is answered by the feasibility in realizing the required experimental conditions.

2.9 The Absolute Electrode Potential of the SHE

The standard hydrogen electrode (SHE) is the most important reference electrode, which has been given arbitrarily the reference potential of $0\,V$. Against the relative potential of the SHE, various data for standard electrode potentials of half-cell reactions are tabulated. Thus, knowing the absolute potential of the SHE gives the possibility to establish an absolute scale for half-cell potentials. Considerable effort has been devoted in finding an experimental value for the absolute electrode potential of the SHE. This includes the work of *Reiss, Parsons, Sato, Trasatti, Gomer, Hansen and Kötz*, whose results are summarized in Tab. 2.1.

[8] Still having rest energy.

The different experimental methods can be divided in four main groups, involving a *Schottky* diode in contact with a SHE [31], a *Born-Haber* thermodynamic cycle [32, 25, 33], a *Kelvin* probe measurement on the (electrode|gas(air)) interface close to the electrode and referencing the *Kelvin* probe against a work function of a known standard [34, 35, 36], and a direct work function measurment of an emersed electrode [37].

Each method contains drawbacks in regard to theoretical or experimental assumptions. In the *Schottky* diode method a zero dipole at the p-doped ($InP|Pt$) interface is assumed and it further requires a value for the potential of zero charge at standard conditions that cannot be measured [31]. As reported in [38], the absolutely essential values in the thermodynamic cycle ([32]) for atomization and ionization energies of hydrogen with the absolute proton hydration energy are under discussion [39, 40, 41]. Except for the method of emersed electrodes [37], the absolute electrode potential of the SHE cannot be obtained by a single measurement. So far, it is thought that the emersion method contains the smallest experimental error in measuring the absolute electrode potential, but it suffers from the emersion process and its sample transfer into ultra-high vacuum (UHV). The original electrolyte layer is damaged through desorption and rearrangement of the electrolyte layer [42, 43].

Comparing the different results in Tab. 2.1, the span of values is 0.42 V, which denotes a wide spread on an electrochemical scale. Clearly, this shows experimental difficulties accompanied as well with the theoretical concept of the absolute electrode potential. Except for *Sato's* work [33], all values were published before the year 1990, when *Trasatti* clarified the meaning of the absolute electrode potential in [11], see chapter 2.8. Of course ,all of

the values reported in Tab. 2.1 are absolute electrode potentials. In fact, it is the question about the underlying reference level. For now, the problem in assigning either location (2') or (3) arises from the loosely defined work function, i.e. measured with photoelectron spectroscopic methods: is it the reference level in vacuum at infinity Φ^{∞} or the reference level of the outer potential Φ^{O}? - discussed in [44] and later on in chapter 3.2.2.

Table 2.1: Numerical values for the absolute potential of the SHE. The value indicated by * is measured against the reversible hydrogen electrode. The location column refers to energy levels, elucidated in chapter 2.8. Abbreviation: *Kelvin* probe (KP); work function (WF); calculated (calc); thermodynamic cycle (TC); emersed electrode (EE); x-ray photoelectron spectroscopy (XPS); ultraviolet photoelectron spectroscopy (UPS).

$\epsilon_{abs}(SHE)$ **in (V)**	**Method**	**Location**	**Ref.**
4.43	Schottkey diode	(2') or (3)	[31]
4.44	calc TC	-[9]	[32]
4.44 ± 0.025[10]	calc TC	(3)[11]	[25]
4.5	calc TC	(3)	[33]
4.456 ± 0.025	KP[12]	(2')[13]	[36]
4.73 ± 0.05	KP[14]	(2') or (3)	[34]

Continued on next page

[9]No access on primary source.
[10]IUPAC recommended value.
[11]Based on the used equation it is (3).
[12]KP referenced against the work function of Hg.
[13]It is claimed (2'), but it can also be (3).
[14]KP referenced against the work function of various materials, inter alia Ag, Au.

Table 2.1 – *Continued from previous page*

$\epsilon_{abs}(SHE)$ **in (V)**	**Method**	**Location**	**Reference**
4.7	KP[15], EE	(2') or (3)	[35]
$4.85 \pm 0.15^*$	UPS, XPS, EE	(2') or (3)[16]	[37]

2.10 Cell Potential

Taking an electrochemical cell and arranging the electrode (M), the solutions (S) and the reference electrode (RE) in the following way:

$$(M|S|RE|M),\ \textit{open circuit} \tag{2.45}$$

In this arrangement, the cell potential is easily obtained as:

$$\epsilon_c = \epsilon(cell) = \epsilon_{abs}(M) - \epsilon_{abs}(RE) \tag{2.46}$$

Although only absolute values have been used, it is clear that the cell potential is a relative value and the same cell potential would have been obtained in any other reference system, e.g. in the one of the SHE:

$$\epsilon_c = \epsilon_{SHE}(M) - \epsilon_{SHE}(SHE) \tag{2.47}$$

It is also clear that each electrode can be considered separately. Therefore, the expression for a single electrode can be applied on each electrode. In chapter 2.8, the absolute electrode potential of a single electrode is obtained from Eq. 2.40, reflecting the reference level of location (3). For an electrode (X) immersed in a solution (S), Eq. 2.40 becomes to:

$$\epsilon^3_{abs} = \Phi^O_{X|O}/e + \Delta\psi_{eX|S} \tag{2.48}$$

[15]KP referenced against the work function of SnO_2.
[16]Compare with [44].

Since (M) and (RE) are immersed in the same solution (S), $\psi_{eX|S}$ is the same for both single electrodes and the cell potential yields Eq. 2.49 and 2.50.

$$\epsilon_c = \Phi^O_{M|O}/e + \psi_{eM} - \Phi^O_{RE|O}/e - \psi_{eRE} \tag{2.49}$$

$$\epsilon_c = 1/e \left(\Phi^\infty_{M|S|V} - \Phi^\infty_{RE|S|V}\right) \tag{2.50}$$

The equilibrium condition for the cell potential is $\epsilon_c = 0$. Thus, Eq. 2.49 and 2.50 results into Eq. 2.51 and 2.52, respectively.

$$\Phi^O_{RE|O}/e + \psi_{eRE} = \Phi^O_{M|O}/e + \psi_{eM},\ \textit{equilibrium} \tag{2.51}$$

$$\Phi^\infty_{RE|S|V} = \Phi^\infty_{M|S|V},\ \textit{equilibrium} \tag{2.52}$$

The same equations as obtained in chapter 2.7.

Chapter 3

Methodology

3.1 *Kelvin* Probe

The *Kelvin* probe (KP) technique, developed in 1898 by Lord *Kelvin* [45] and further modified by *Zisman* in 1932 [46], uses a vibrating plate capacitor in combination with a nulling technique to oppose the outer potential difference[1]. The outer potential difference is formed when two different metals, i.e. the plate[2] of the KP and the sample (SA), are brought in electrical contact. Applying the equilibrium condition[3] gives the outer potential difference to:

$$\Delta\psi_{eSA|KP} = \psi_{eSA} - \psi_{eKP} = \Phi^{O}_{SA|O}/e - \Phi^{O}_{KP|O}/e,\ equilibrium \tag{3.1}$$

As described in [47], the plate capacitor with the capacity C, Eq. 3.2, area A, permittivity ε_0, and relative permittivty ε_r vibrates with the phase ωt about Δr around the center position r. An alternating current i_{ac} is influenced in the external circuit, Eq. 3.3, that is used as the measurand in the nulling technique.

$$C = \varepsilon\varepsilon_0 \frac{A}{r + \Delta r\ sin(\omega t)} \tag{3.2}$$

$$i_{ac} = \Delta\psi_{eSA|KP} \frac{dC}{dt} \tag{3.3}$$

$$i_{ac} = \left(\Delta\psi_{eSA|KP} - \Delta\psi_{eapl}\right) \frac{dC}{dt} \tag{3.4}$$

An external bias can be used to compensate the outer potential difference, such that the alternating current vanishes, Eq. 3.4. When i_{ac} is small enough,

[1] Also called the contact potential difference between the KP and the sample, Fig. 3.1.
[2] Or tip [47], the capacity depends on the geometry.
[3] $\Phi^{\infty}_{SA|V} = \Phi^{\infty}_{KP|V}$, see chapter 2.7.

typically in the order of pA, $\Delta\psi_{eSA|KP}$ is determined to $\approx \Delta\psi_{eapl}$.

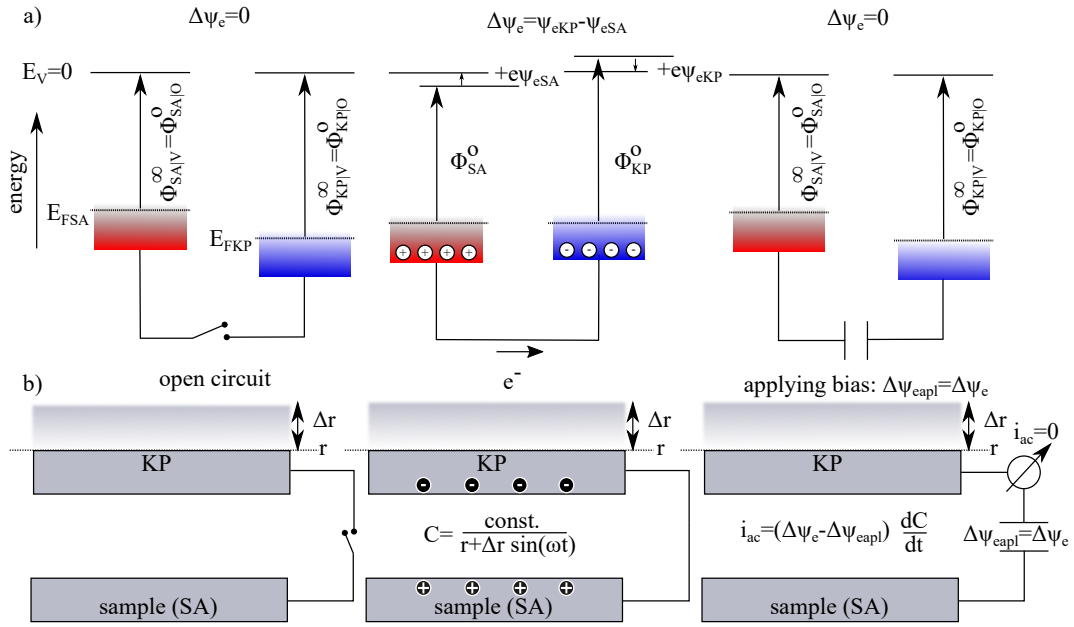

Figure 3.1: Working principle of the *Kelvin* probe (KP). a) energy diagram of the open circuit-, equilibrium-, external compensation mode. b) the tip of the KP is placed in front of the sample (SA) such that a plate capacitor is formed. In the compensation mode, the change in the capacity C, through the variation of the distance about Δr, has no influence on the alternating current i_{ac}.

3.1.1 Measuring Absolute Electrode Potentials with Help of KP

In 1933, it was shown by *Yamins* and *Zisman* that the KP method can also be applied to liquid samples [48]. Later on this idea was modified and extended to immersed and emersed electrodes [34, 35, 42, 36, 37, 43], shown in Fig. 3.2. For emersed electrodes, the absolute electrode potential, Eq. 2.40,

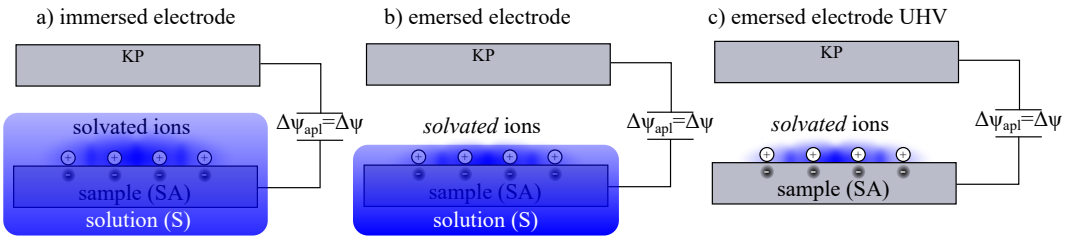

Figure 3.2: Electrodes covered with an electrolyte solution and specifically adsorbed ions. a) the immersed electrode in bulk solution; b) the emersed electrode without excess solution; c) the emersed electrode in UHV with sub-monolayer adsorbed solution [42, 37]. During the emersion process into UHV, the original solution layer a) is *damaged*, compare chapter 2.9 and [42, 43].

can be rewritten as:

$$\epsilon^{3}_{abs} = -\alpha_{eSA|S|O}/e = \Phi^{O}_{SA|S|O}/e = \Phi^{O}_{SA|O}/e + \Delta\psi_{eSA|S},\ \textit{location}\ \mathbf{(3)} \quad (3.5)$$

In the situation of Fig. 3.2, where the KP is placed right above the surface of the solution, equilibrium is maintained by $\Phi^{\infty}_{SA|S|V} = \Phi^{\infty}_{S|V} = \Phi^{\infty}_{KP|V}$ and no work is required to move an electron within the system of (SA|S|KP). Thus, the absolute electrode potential is also given by Eq. 3.6 [42, 43, 47].

$$\epsilon^{3}_{abs} = \Phi^{O}_{SA|O}/e + \Delta\psi_{eSA|S} = \Phi^{O}_{KP|O}/e + \Delta\psi_{eKP|S},\ \textit{location}\ \mathbf{(3)} \quad (3.6)$$

In accordance to Eq. 3.6, a linear relationship, between $\Delta\psi_{eKP|S}$ and the applied potential before or rather during emersion, is found [35, 43]. Since the KP measures $\Delta\psi_{eKP|S}$, the absolute electrode potential still depends on $\Phi^{O}_{KP|O}$. With an additional measurement, $\Phi^{O}_{KP|O}$ can be determined. So far, knowing the work function of $\Phi^{O}_{SA|O}$ is enough: $\Phi^{O}_{KP|O}$ can be calculated from Eq. 3.1. Therefore, two steps are required: a sample[4] transfer into UHV, where the work function $\Phi^{O}_{SA|O}$ can be accessed by means of photoelectron

[4]With no electrolyte layer.

spectroscopy, and the transfer to non-UHV (this can alter the value of $\Phi^{O}_{SA|O}$), where $\Delta\psi_{eSA|S}$ of the emersed electrode is measured. Another possibility is the procedure used in [34, 35, 36]; that provides the work function $\Phi^{O}_{KP|O}$ by calibrating the KP on a reference sample of known work function $\Phi^{O}_{SA|O}$ and the calculation of $\Phi^{O}_{KP|O}$ along with Eq. 3.1. Only if the work function of the reference sample is unaffected from the different experimental conditions, a reliable value for the absolute electrode potential is obtained.

3.2 Photoelectron Spectroscopy

The history of *X-Ray Photoelectron Spectroscopy* (XPS), as it is reported in e.g. [49, 50], goes back to the year 1887 when *Heinrich Hertz* experimentally discovered the photoelectric effect [51]. Further studies about *Hertz'* findings were done by *Hellwachs* and *Lennard* in 1888/89 [52, 53] and later on by *Lennard* who describes the onset of light-induced photoelectrons as the minimal energy required to exceed the threashold, given as the work function [54]. In 1905 *Albert Einstein* [55] gave the quantum theoretical explanation of the photoelectric effect, including the understanding of energy being carried by light in discrete quantized packets along with the *Planck* relation. Besides the theoretical concept, that a photoelectron carries the information of the material from where it was emitted, an experimental milestone was the observation of chemical line-shifts caused by the change in chemical bonding, *Robinson* and *Young* in 1930 [56]. Starting in the 1950s, major steps were done in developing high-resolution spectrometers, which was driven by the work of *Steinhardt* and *Siegbahn* [57, 58]. *Siegbahn* formed the acronym ESCA, which stands for *electron spectroscopy for chemical analysis*. In 1981 *Siegbahn* obtained the *Nobel Price* in physics for his important contributions to the development of the ESCA.

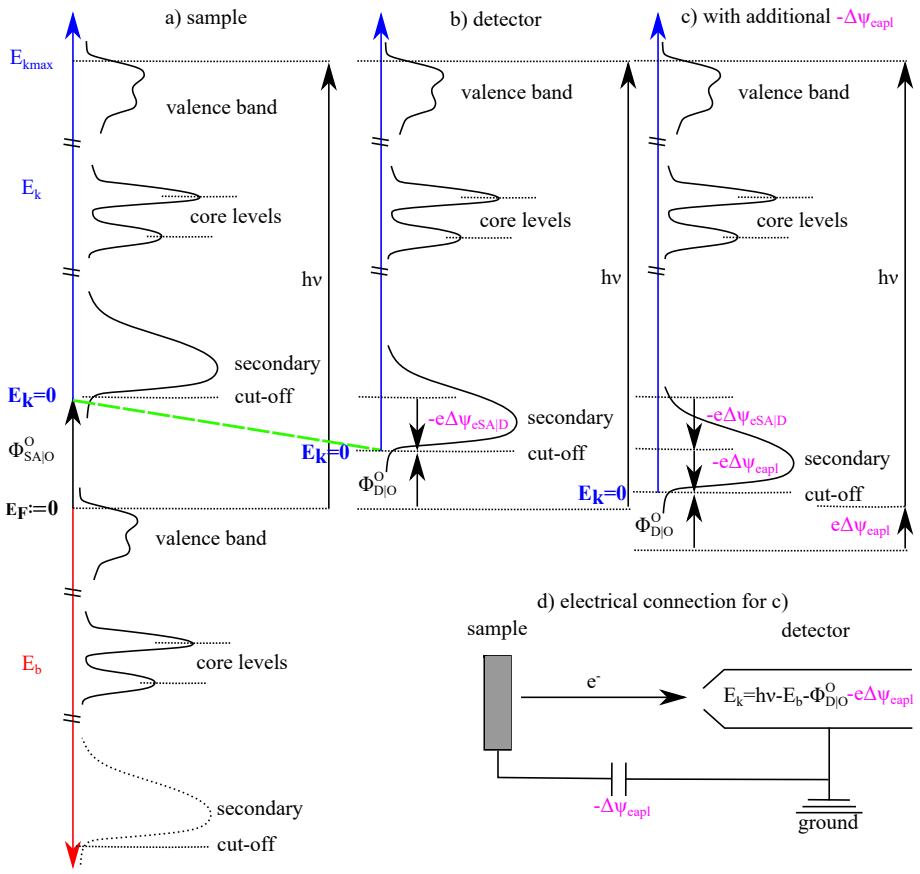

Figure 3.3: The principal of PES for a metallic sample (SA) on two different energy scales: Photoelectrons from different states are detected on the kinetic energy scale. The binding energy can be calculated independently of the work function $\Phi^O_{SA|O}$. a) photoelectrons excited (with $h\nu$) from a state having the binding energy E_b and the kinetic energy $E_k = h\nu - E_b - \Phi^O_{SA|O}$. b) the *Fermi level* of the (SA) and detector (D) are aligned. The kinetic energy of photoelectrons from the (SA) is measured with the (D) to $E_k = h\nu - E_b - \Phi^O_{D|O}$. c) the effect when an additional bias $-\Delta\psi_{eapl}$ is applied between the (SA) and the (D). d) the electrical connection for applying the bias. Note: The secondary cut-off is induced by the measuring process and the photoelectron spectrum is obtained with the *Fermi level* referenced to zero. Adapted from [59].

In XPS or photoelectron spectroscopy (PES) in general, photons with the energy[5] $h\nu$ irradiate the sample whereby photoemission occurs through three steps, e.g. [50]: (1) the absorption of the photon by a valence- or core electron from the atomic shell, resulting in the formation of an ionized atom and a photoelectron. (2) the movement of the photoelectron to the sample surface, including various elastic and inelastic scattering processes for the majority of the photoelectrons. (3) leaving the sample surface with the kinetic energy E_k into the vacuum after overcoming the work function.

The kinetic energy of the photoelectrons are determined e.g. in a biased hemispherical analyzer [60, 61, 62] and the number of electrons being recorded after amplification by an electron multiplier, e.g. channeltron or microchannel plate. Since the sample is electrically connected[6] to the detector (electron multiplier), an outer potential difference [63] between the sample (SA) and detector (D) occurs due to the corresponding difference in work functions, Eq. 3.7.

$$\Delta\psi_{eD|SA} = \Phi^O_{SA|O}/e - \Phi^O_{D|O}/e \tag{3.7}$$

When an incident photon transfers energy $h\nu$ onto an electron, an elastically scattered photoelectron obtains the kinetic energy $E_k = h\nu - E_b - \Phi^O_{SA|O}$ when the original electron had the binding energy E_b relatively to the *Fermi level*, Fig. 3.3 a). Entering the detector, the photoelectron experiences the additional kinetic energy exerted from the outer potential difference, Fig. 3.3 b). In consequence the resulting kinetic energy is independent of the sample's work function [63], Eq. 3.8.

$$E_k = h\nu - E_b - \Phi^O_{SA|O} - \left(\Phi^O_{D|O} - \Phi^O_{SA|O}\right) = h\nu - E_b - \Phi^O_{D|O} \tag{3.8}$$

[5]Lab source usually $Al\ K\alpha$ 1486.71 eV or $Mg\ K\alpha$ 1253.6eV.
[6]By ground.

Photoelectrons obtain the maximum kinetic energy $E_{kmax} = h\nu - \Phi^{O}_{D|O}$ when the binding energy E_b is zero. These photoelectrons are assigned to originate from the *Fermi level* E_F, Fig. 3.3. As part of the calibration, the binding energy at the *Fermi edge* is put to zero, and the detector's work function is empirically determined from the zero offset of the spectrum [64, 65].

Although, Eq. 3.8 is independent of the sample work function, for instance denoted as Φ^{PES}_{SA}, Φ^{PES}_{SA} can be easily extracted from the width of the spectrum [63, 66], with:

$$\Phi^{PES}_{SA} = h\nu - (E_{kmax} - E_{kmin}) = h\nu - (E_F - E_{off}) \tag{3.9}$$

Photoelectrons originating from the cut-off energy E_{off} are difficult to detect since they have zero kinetic energy. Therefore a negative bias, in the range of ≈-3 to $-10\ V$, is applied to the sample in order to accelerate the cut-off photoelectrons for detection [66], Fig. 3.3 d).

Besides the diffuse features in a PES spectrum, e.g. the cut-off arising from inelastic scattered photoelectrons, distinct *peaks* with a line width of $\approx 0.4\ eV$[7] are observed from elastically scattered photoelectrons. These photoelectrons carry chemical information and allow quantification, typically down to 1 *at.* %. Any change in the atomic bond state affects the measured spectrum with regard to binding energy, peak width, peak shape, valence band structure, bonding satelites, and work function [50]. The information depth depends on the inelastic mean free path (IMFP) of the photoelectron, tabulated for many materials e.g. in [67], which is about $0.3 - 10\ nm$ for soft X-rays, as used in XPS.

[7]Defined by the full width at half maximum (FWHM) of the peak height.

3.2.1 Ambient Pressure Photoelectron Spectroscopy

Compared to conventional XPS, *Ambient Pressure X-ray Photoelectron Spectroscopy* (APXPS) does not require UHV conditions and can be operated on some instruments up to 100 $mbar$[8]. More frequently systems can be operated up to 25 $mbar$, more practically are operated at pressures less than 25 $mbar$. The reason for this is the attenuation of intensity by the process of photoelectron scattering at gas molecules. The electron transmission factor I_p/I_o, for photoelectrons with a kinetic energy E_k and the cross section $\sigma(E_k)$, shows an exponential attenuation over the distance r for a specific gas[9] at the pressure p and temperature T, Eq. 3.10 [70].

$$I = \frac{I_p}{I_0} = exp\left(-\frac{r\sigma(E_k)p}{k_B T}\right) \tag{3.10}$$

Photoelectrons with $\sigma(100\ eV)$ and passing a distance of 1 mm in an atmosphere of $p = 10\ mbar$ of water vapor have a cross section[10] of $\approx 10r^2_{Bohr}$ [68], that gives I/I_0 to about 0.001 at room temperature.

Besides the influence on the intensity, gases increase the risk for a breakdown voltage at parts operating at high voltage, i.e. the lens system and detector. According to *Paschen's* law [71], a breakdown voltage can be avoided by increasing the distance between the electrodes, which in turn goes on the expense of a less-favored photoelectron trajectory to the detector. Therefore leading to further intensity loss.

To reduce the intensity loss down to a minimum, a differentially pumped lens system with three stages is used that focus the photoelectrons onto the aperture of the corresponding stage, Fig. 3.4. The sample is placed in the

[8]SPECS Surface Nano Analysis GmbH (2019).

[9]The cross sections for photoelectron scattering are available in literture, e.g. [68, 69].

[10]In units of the *Bohr* radius r_{Bohr}.

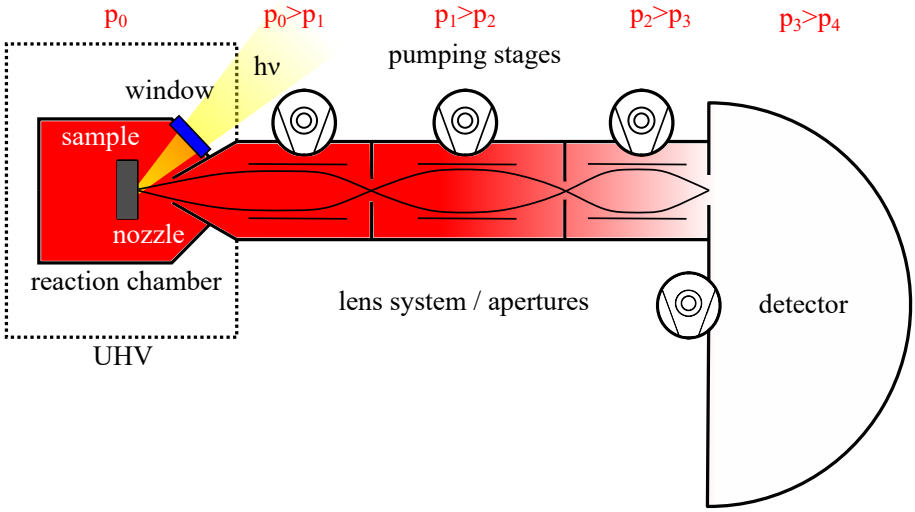

Figure 3.4: Differential pumping of an APXPS instrument: The reaction chamber, including a gas of pressure p_0, is sealed from the surrounding chamber, kept in UHV. Through a silicon nitrite window X-rays can reach the sample surface. The emitted photoelectrons need to pass through the nozzle and the lens system in order to enter the detector. The lens system focuses the photoelectrons, coming from the sample, on the apertures. The initial pressure p_o can be reduced about 7-9 orders of magnitude, resulting to p_4 at the detector.

reaction chamber, facing a nozzle with an aperture of $\approx 0.3\ mm$ in diameter, Fig. 3.5. The reaction chamber is separated from the X-ray source by a X-ray transparent silicon nitrite window[11] that allows to keep UHV conditions in the X-ray source. The nozzle aperture demands a focused X-ray source and a careful alignment of the X-ray geometry: the sample-to-nozzle position and focus of the lens system. Both need to coincide such that a maximum number of photoelectrons find its trajectory to the entrance aperture of the detector.

[11] $\approx 100\ nm$ thick.

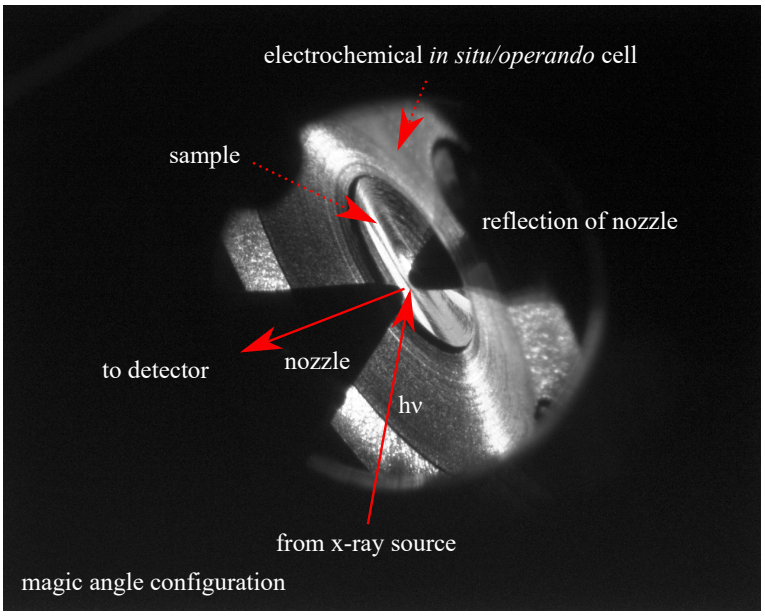

Figure 3.5: Optical photograph of the nozzle from an APXPS instrument in measuring position. The sample-to-nozzle distance is $\approx 0.06\ mm$, corresponding to two times the aperture diameter.

3.2.2 Measuring Absolute Electrode potentials with PES in UHV

Coming back to the question arised in chapter 2.9: How is the photoelectric work function interpreted; is it the electron at rest in the vacuum level at infinity or is it the vacuum level *just outside* the sample? The *IUPAC* definition of the work function is clear about that point since it is defined as *"the minimum work needed to extract electrons from the Fermi level of a metal across a surface carrying no net charge"* [72]. I.e. both reference levels are the same. In practice, the *IUPAC* definition is hard to realize since no net charge cannot be generally assumed. A sample in contact with a dislike terminal causes an outer potential difference.

However, the *IUPAC* definition only compromise the removal of the electron, not the position where to locate the electron. The term location can be easily mistaken with the same term on a length- or energy scale. The context between the energy and the length scale is the *Heisenberg* uncertainty principle. In the present work, the main interest is the determination of work functions and absolute electrode potentials, going ahead with the determination of energies, thus demanding the indeterminacy for the location at the length scale accordingly to the uncertainty principle. However, the energy for an electron is defined being somewhere in vacuum, far away from matter, and not at a certain position in vacuum.

A classical approach was given in chapter 2.4, where the location for the vacuum level *just outside* was given to 10^{-4} cm right above the surface, which is an approximation in order to avoid electrostatic influence [9, 8]. Considering the location *infinite far*, it is clear that the work function Φ^{PES}, measured with PES, depends on the length r of the lens system and detector,

see Fig. 3.4. In other words, the location *infinite* far is experimentally approximated when $r >> 10^{-4}$ cm. Especially at APXPS instruments, where $r \approx 1\ m$, r is large compared to conventional XPS systems since additional space is required for the realization of the differential pumping. Anyhow, that might give the impression that Φ^{PES} rather refers to *infinite* than *just outside*. In truth, Φ^{PES} must be apprehended as the work function $\Phi^{O}_{SA|O}$, *just outside* the sample. Thus, with the method of PES the absolute electrode potential ϵ^{3}_{abs}, and not $\epsilon^{2'}_{abs}$, is measured. This also applies for KP measurements involving a calibration procedure with PES and, generally, on all ϵ_{abs} determinations involving the work function measured with PES. So far, the only exception is the case of the non-charged electrode, where both vacuum levels coincide, see *IUPAC* definition.

As it is discussed in [73, 44], the electron density over the (metal|vacuum) interface results in a dipole, i.e. the surface potential [74, 75, 76], Fig. 3.6 b). For a clean metal surface, the dipole moment points towards the bulk of the metal, generally created by negative charge accumulation at the vacuum side and positive charge accumulation at the metal side. For an electron at distance r from the dipole with the extension L the potential energy E_{pot} is shown in Fig. 3.6 c) [73]. The flat portion is associated with E_O [73] that exists for $r << L$. In the case that $r >> L$, the potential energy declines with $\propto r^{-2}$ to E_V and can be approximated by a point dipole. When the sample and the detector of a PES instrument are in equilibrium, this is the case when $\Phi^{\infty}_{D|V} = \Phi^{\infty}_{SA|V}$, Fig. 3.6 a), the photoelectron leaving the sample loses the kinetic energy $\Phi^{O}_{SA|O}$ and $e\psi_{eSA|V}$, enters the detector on E_V, gains the kinetic energy $-e\psi_{eD|V}$ and $-\Phi^{O}_{D|O}$ such that energy is conserved since no work is required to move an electron from the sample to the detector,

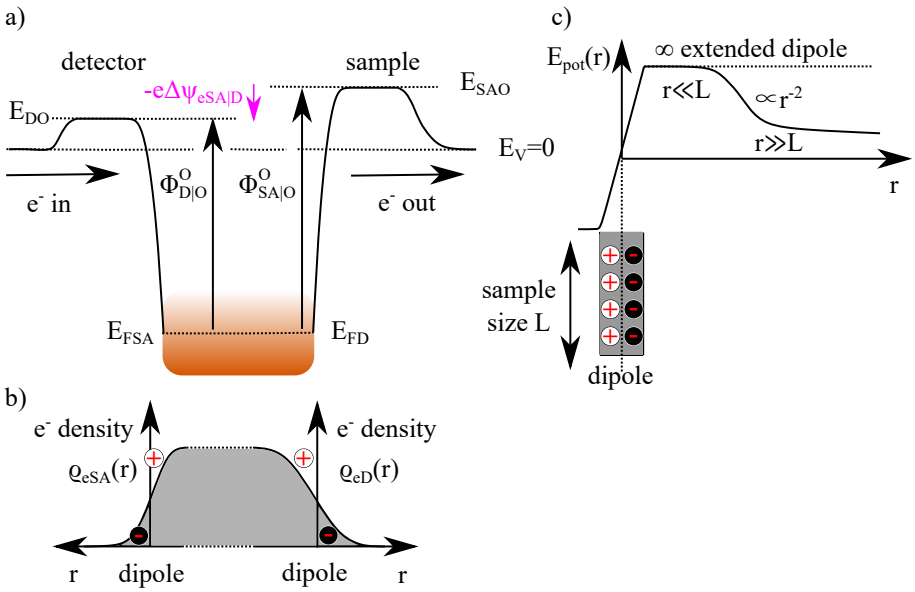

Figure 3.6: The work function measured with PES: a) the *Fermi levels* of the detector and the sample are aligned. A photoelectron leaves the sample to the vacuum level *just outside* the sample E_{SAO}, enters the vacuum level at *infinity* $E_V = 0$, reaches the vacuum level *just outside* the detector E_{DO}, and reenters the common *Fermi level*. b) The electron density distribution at the (vacuum|sample|detector|vacuum) interface results in a surface dipole. c) The potential energy of an electron depends on the distance r and the geometry of the dipole with the extension L. Adapted from [73].

Eq. 3.11.

$$\Phi^{O}_{SA|O} + e\psi_{eSA|V} - e\psi_{eD|V} - \Phi^{O}_{D|O} = 0 \tag{3.11}$$

Photoelectrons arising from the cut-off lose all their kinetic energy at E_{SAO} and fall back to the common *Fermi level*. For this reason, PES measures the work function *just outside* the sample. Therefore,

$$\Phi^{PES} = \Phi^{O}_{SA|O}. \tag{3.12}$$

Using the method of *Neff* and *Kötz* [42, 37], the absolute electrode potential can be determined on electrodes emersed into the UHV, see chapter 3.1.1. Since it was shown that the electrochemical double layer cannot maintained after the process of emersion, *"...investigations of the molecular and electronic structure of electrochemical double layers on emersed electrodes under UHV conditions appear to be highly questionable"* [42]. Anyhow, a $1:1$ correlation between the emersion potential and the work function Φ^{PES} is found [42, 37]. Whether or not an intact electrochemical double layer is maintained, the measured work functions is an absolute electrode potential ϵ^{3}_{abs}, but not directly comparable to an immersed electrode. For a sample (SA) with an adsorbed solution (S), e.g. an electrolyte layer of an emersed electrode, the photoelectron of the (SA) has to cross the interface (SA|S|O). Thus, the work function becomes to:

$$\epsilon^{3}_{abs} = \Phi^{O}_{SA|S|O}/e = \Phi^{O}_{SA|O}/e + \Delta\psi_{eSA|S} \tag{3.13}$$

Eq. 3.13 is identified with a work function change from the clean sample (SA') to the (SA) with the adsorbed solution. Hence,

$$\epsilon^{3}_{abs} = \Phi^{O}_{SA|S|O}/e = \Phi^{O}_{SA'|O}/e + \Delta\Phi^{O}/e. \tag{3.14}$$

Eq. 3.13 can be written as:

$$\epsilon^3_{abs} = \Phi^O_{SA|S|O}/e = \Phi^\infty_{SA|S|V}/e - \psi_{eSA} \tag{3.15}$$

And for the clean (SA'), the photoelectron crosses the interface (SA'|O) such that

$$\Phi^O_{SA'|O}/e = \Phi^\infty_{SA'|V}/e - \psi_{eSA'} \tag{3.16}$$

is obtained. Comparing Eq. 3.14, 3.15 and 3.16, gives the change due to the adsorbed electrolyte layer to:

$$\Delta\Phi^O/e = \psi_{eSA'} - \psi_{eSA} \tag{3.17}$$

In summary: For an emersed electrode covered with a thin film of electrolyte, thin enough that photoelectrons can cross the interface (SA|S|O), the absolute electrode potential ϵ^3_{abs} is directly obtained from the work function by PES.

3.3 *In Situ/Operando* Electrochemistry in Ultra-High Vacuum

Chapter 3.3 is partially reproduced from *Electrochemistry in ultra-high vacuum: The fully transferable ultra-high vacuum compatible electrochemical cell* [77] `https://doi.org/10.1063/1.5046389`. In agreement with the copyright guidelines of the *AIP Publishing* (see **Appendix C** Fig. C.1) this chapter contains parts of text, graphics, and tables of said article. The author's contribution includes the design of the set-up, execution and analysis of experiments, discussion of all experimental results, and article writing.

3.3.1 Engineering: *The Specification Sheet*

The aim is to construct an electrochemical cell (EC) that allows to conduct *in situ* investigations of the electrode surface *in operando*. Preferably, a controllable thin film of electrolyte is desired to form at the electrode surface

that allows the electrolyte and the gas phase to be in thermodynamic equilibrium and further affects the electrochemical potential, see Eq. 2.11, 2.16. In contrast, electrodes emersed in UHV [42, 37], where presumedly only $\approx 1E^{-10}$ $mbar$ of H_2O is present, are barely in the condition of bulk electrolyte.

On a technical background, the compatibility of UHV and electrochemistry is opposed. From an analytical perspective, the *pressure gap* is reduced by the development of the APXPS, but also here technical restrictions must be considered. An electrolyte in equilibrium with its gas phase, will form crystals that produce short circuits in the lens system as well as in the detector. Hence, damaging the most expensive parts of the equipment. For that reason, the required specifications for the EC are the exclusion of electrolyte contamination and further the possibility to operate the EC in UHV as well. In addition, a conventional three electrode set-up should be used, with the working- (WE), reference- (RE), and counter (CE) electrode connected to a potentiostat that is located outside the vacuum chamber. Thus, appropriate electrical feedthroughs are required: three for the WE, RE and CE, two to bias the WE against the ground potential that allows to determine work functions with PES. Considering the choice of materials, exclusively UHV compatible and chemical inert materials are suitable, see [78]. Especially for accurate work function measurements only non-magnetic materials must be used. Generally, the material selection and its application in UHV is conditioned, by the mechanical strength[12], gas permeation[13], low vapor pressure,

[12] At $\Delta p = 1$ atm, a vacuum chamber with a surface of 1 m^2 needs to withstand a force of $1E^6$ N [79].

[13] The permeation rate of a FKM (fluoroelastomers) O-ring for atmospheric air with 60 % humidity is about $4E^{-7}$ $Pa\ m^3/s$, limiting the vacuum to $1E^{-8}$ $mbar$ [79].

clean surfaces[14], thermal compatibility[15], and chemical inertness [79].

In vacuum technology, the equilibrium pressure p_{eq} is obtained when the gas load equals the pump throughput. For a vacuum chamber, specified by its volume V_c, inner- and external surface area, wall thickness, and leaks, the pump speed (S) can be chosen accordingly to the desired equilibrium pressure, classified in Tab. 3.1.

Table 3.1: The pressure classification in vacuum technology. Abbreviations: Number density (NP), mean free path (MFP), low vacuum (LV), medium vacuum (MV), high vacuum (HV), ultra-high vacuum (UHV). Reproduced from [79].

p range	**p** $(mbar)$	**ND per** (cm^{-3})	**MFP** (m)
1 atm	1013.25	$2.7E^{19}$	$6.8E^{-8}$
LV	300...1	$1E^{19}...1E^{16}$	$1E^{-8}...1E^{-4}$
MV	$1...1E^{-3}$	$1E^{16}...1E^{13}$	$1E^{-4}...1E^{-1}$
HV	$1E^{-3}...1E^{-7}$	$1E^{13}...1E^{9}$	$1E^{-1}...1E^{3}$
UHV	$1E^{-7}...1E^{-12}$	$1E^{9}...1E^{4}$	$1E^{3}...1E^{8}$

The gas load depends on the sum of leak rates τ_i that is composed of individual contributions from simple leaks[16] τ_L, permeation through walls[17] τ_P, and outgassing from metal surfaces τ_M(t) and seals $\tau_S(t)$. If the total leak

[14]Low surface roughness, i.e. little molecular adsorption and lower degassing.
[15]Bake-out for UHV is required and low thermal expansion is wanted.
[16]E.g.: Crack, hole.
[17]Becomes significant in UHV [79].

rate is known, the equilibrium pressure can be calculated from Eq. 3.18 [79].

$$p_{eq} = \frac{1}{S}\sum_i \tau_i = \frac{1}{S_p}\left(\tau_L + \tau_P + \tau_M(t) + \tau_S(t)\right) \tag{3.18}$$

Since leaks and permeation[18] are static, the leak rate $\tau_L + \tau_P$ is obtained by Eq. 3.19 and can be determined by measuring the pressure increase Δp over a short time Δt [79].

$$\tau_{LP} = \tau_L + \tau_P = \frac{\Delta p\ V}{\Delta t}\ ,\ \Delta t\ small \tag{3.19}$$

Even leaks in the UHV region can be measured. From the atmospheric side a tracer gas[19] intrudes with the speed of sound[20] through simple leaks [80], further, being detected with a mass spectrometer. On the same time scale gas permeation can be neglected.

The maximum tolerable leak rate τ_{max} of the EC, including all feedthroughs, can be formulated, firstly, on a technical restriction and, secondly, as the required time to perform experiments. The technical restriction is the maximum operational pressure of the X-ray source. To limit the risk in occurring flashovers, at an anode voltage of 15 kV, the maximum operational pressure is $1E^{-7}$ $mbar$. Leaks in the EC lead to electrolyte loss that limits the time to prepare and perform experiments in UHV. An acceptable time to introduce, i.e. to evacuate, the EC is 1 day, while the experiments are assumed to last 5-6 days, giving a total time of 7 days in UHV. The electrolyte volume is 100 μl.

With these considerations, the seal of the EC needs to be engineered to meet the most severe restriction. Comparing the different restrictions, it

[18]It is assumed that the diffusion conditions stay constant.
[19]Typically He.
[20]For He: 970 m/s [80].

can be seen from Tab. 3.2 that τ_{max} is technically limited. Assuming that τ_{max} is caused by a simple leak, a geometrical equivalent hole diameter can be calculated from Eq. 3.20 [80], where v_{th} is the thermal speed of water vapor leaving the EC. Hence, a maximum hole diameter of $2.5E^{-7}$ m can be allowed, see Tab. 3.2.

$$d_\tau = \sqrt{\frac{4\tau}{\pi \, \Delta p \, v_{th}}} \tag{3.20}$$

Table 3.2: Technical engineering of seals in UHV: calculated for: $\Delta p = 1$ atm (EC interior/UHV), $v_{th} = 585$ ms^{-1} (H_2O vapor) [79], $S_p = 300$ ls^{-1}. Indicated by *: $S_p = 80$ ls^{-1}. Ideal gas behavior is assumed. Colored entries are based on measurements. Abbreviations: technical (tech); experimental (exp); mass spectrometer (MS); pressure gauge (PG).

Condition	$\boldsymbol{\tau}$ **(mbar l** $\boldsymbol{s^{-1}}$**)**	$\boldsymbol{p_{eq}}$ **(mbar)**	***Hole*** $\oslash$ **(m)**
tech. restriction τ_{max}	$3.0E^{-5}$	$1.0E^{-7}$	$2.5E^{-7}$
exp. restiction τ_{max}	$2.2E^{-4}$	$7.5E^{-7}$	$6.9E^{-6}$
UHV τ_{min}	$3.0E^{-10}$	$1.0E^{-12}$	$8.0E^{-10}$
Δp with PG τ_{LPMS} *	$8.0E^{-7}$ *	$1.0E^{-8}$ *	$4.1E^{-8}$ *
Δp with MS[21] τ_{LP}	$6.0E^{-8}$	$2.0E^{-10}$	$1.1E^{-8}$

In order to realize a seal that fulfills the requirements of τ_{max}, the area of the seal and surface roughness is relevant with respect to d_τ, and careful machining is required. This required an iteration process through subsequent

[21] At mass 18.

EC designs, steadily having been improved. So far, the latest generation of ECs outperform the stated requirement. The leak rate of the EC[22] was determined in two ways:

Firstly, measuring the pressure with a pressure gauge (PG) while the EC[23] was evacuated in the load lock (LL), with $S_p = 80\ ls^{-1}$. After 24 hours of evacuation, the pressure was compared to the equilibrium pressure of the empty LL and the leak rate was calculated with Eq. 3.18. The theoretical time to evacuate the LL can be calculated with Eq. 3.21 [79] and is much smaller than 1 s.

$$t_{evac} = \frac{V_{LL}}{S_p}\ ln\frac{p}{p_{eq}} \ll 1\ s \tag{3.21}$$

Since water adsorbs on the surface, considerably longer evacuation times are observed in practice. The desorption time can be calculated with Eq. 3.22 [79]. With the area normalized specific desorption rate of water on stainless steel $\Gamma = 2.7E^{-6}\ mbar\ ms^{-1}$ [79], the time constant $t_o = 1\ h$ [79], the surface area $A = 0.3\ m^2$, and $p_{eq} = 1E^{-8}\ mbar$, the desorption time is about 100 hours. Hence the leak rate, determined in the LL, is still influenced by adsorbed water, thus and τ_{LPMS} was measured in approximation, see Tab. 3.2.

$$t_{des} = \frac{\Gamma A t_0}{S_{pLL} p_{eq}} \approx\ 100\ h \tag{3.22}$$

Secondly, the EC was transferred into another chamber ($S_p = 300\ ls^{-1}$). Here, the leak rate was determined using a mass spectrometer with a detection limit of $\pm 1E^{-14}\ mbar$. In the meanwhile, the EC was used in UHV for 500 hours, long enough to assume that $\tau(t) \approx 0$. The pressure increase was obtained from the signal at mass 18, but also others[24], and is compared to

[22] With the same EC and without modifications.

[23] Previously, the EC was assembled in a glove box with ≈ 100 % relative humidity.

[24] At the masses 80, 81 and 64 (all from H_2SO_4), with intensities below the detection limit.

the equilibrium pressure of the empty chamber. In this way, the leak rate of τ_{LP} was determined, see Tab. 3.2.

3.3.2 The Set-up

A new experimental set-up for *in situ/operando* investigations of redox reactions is introduced. This set-up in combination with UHV methods from the field of surface science, provides completely new possibilities to investigate electrochemical redox reactions. Two types of cells are distinguished conceptionally: In the permeation configuration, the WE is electrochemically polarized on one side of a membrane (entry side), leading to atomic hydrogen uptake, i.e. allowing proton and electron exchange between the entry and the other side (exit side) of the membrane. Here it is found that the applied potential on the entry side shows a 1 : 1 correlation with the measured potential on the exit side [81]. The concept of the *window cell* requires an ultra-thin, electron transparent window, such as single layer graphene (SLG), for XPS, or X-ray transparent silicon nitride windows for X-ray absorption spectroscopy (XAS). In this case, the (solid|liquid) interface can directly probed under applied potentials. In both configurations the applied potential is measured with a palladium hydride (PdH_X) RE, with so far unseen precision and long-term stability. The cell is constructed with regard to transferability within a UHV system that allows sample preparation. A modular construction allows a straightforward changeover between the different configurations. As a first application, an approach based on atomic hydrogen is presented. Further application concepts are discussed. The set-up functionality is demonstrated by the example of *in situ/operando* investigation of the palladium oxide reduction.

3.3.3 Background: *The Electrode in the Dry*

Recently it was found that an electrode potential applied on one side (entry side) of a palladium sample can lead to an even change of the work function on the other side (exit side) of that sample [81]. As shown in Fig. 3.7, the work function of a palladium sample in dry nitrogen atmosphere, whose entry side is exposed to electrolyte and polarized to different potentials, indeed shows a $1:1$ dependence on these applied potentials. According to Eq. 3.23, the measured electrode potential ϵ_{SHE}, can be expressed by absolute electrode potentials, e.g. $\epsilon^{2'}_{abs}$.

$$\epsilon_{SHE} = \epsilon^{2'}_{abs} - \epsilon^{2'}_{abs}(SHE) = 1/e \left(\Phi^{\infty}_{WE|S|V} - \Phi^{\infty}_{RE|S|V}(SHE)\right) \tag{3.23}$$

In terms of electrochemistry: defined by the *Nernst* equation the electrode

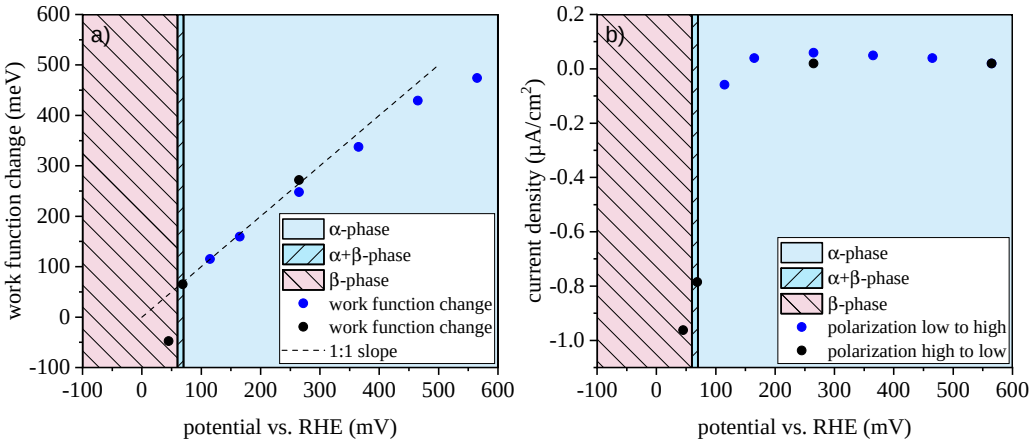

Figure 3.7: a) Kelvin Probe (KP) measurements of the work function change (exit side) and b) current density ($j(\epsilon)$ curve) correlation, both depending on the applied potential (entry side). On the entry side, 100 μm thick polycrystalline palladium (99.95 %) is exposed to 0.1 M H_2SO_4. The atmosphere on the exit side is dry nitrogen with a relative humidity (r.h.) of < 0.1 %. All measurements were performed at room temperature.

potential of a PdH_X electrode depends sensitively on the hydrogen activity in the palladium, as it is indicated by the different phases of the PdH_X, Fig. 3.7. Applying an electrode potential on the entry side, which is low enough for hydrogen absorption, leads to a corresponding potential on the exit side. Due to a high hydrogen solubility and -diffusion, electrochemical equilibrium is achieved between both sides of the membrane.

At potentials higher than 300 mV vs. RHE, i.e. at very low hydrogen activities, longer times are required to equilibrate the entry and the exit side. Since long enough waiting times were not always sufficiently maintained, deviations can be observed from the ideal behavior (1 : 1 slope). This also becomes noticeable by changing the polarization direction, which was firstly done for the blue- and secondly for the black circles, Fig. 3.7. Although the exit side was exposed to dry nitrogen atmosphere, water in the order of 0.1 $mbar$ is present and adsorbed on the exit side. In contrast to UHV conditions, this is orders of magnitude higher and leads to the formation of sub- or monolayers of water on the exit side [82]. This water layer seems to play a crucial role in the establishment of the double layer on the hydrogen- and oxygen electrode.

Applying the knowledge from *the electrode in the dry* towards a UHV compatible cell, which is in addition transferable, gives a powerful tool to investigate surface reactions with the whole arsenal of analytical techniques for in *in situ/operando* investigations. A successful implementation consists of a well-sealed cell and a stable three-electrode set-up.

3.3.4 The Reference Electrode

Here, the major task was to find a robust and long-term stable RE which allows to miniaturize the cylindrical cell dimensions down to 12×10 mm.

Since no commercially available RE would satisfy the requirements, a PdH_X RE ($X = \alpha + \beta$) with previously unknown precision and long-term stability was developed. Of course, the literature about the PdH_X RE is broad, but no long-term stability with sufficient precision is reported yet. Based on [83, 84, 85], the common use is restricted to around $1 - 2$ hours [83, 85] with the precision of $\pm 1.2\ mV$ [83] in which the plateau reproducibility is $\pm 10\ mV$ [84]. On the other hand, the so-called *internally* charged electrode can achieve much longer times while the binary PdH_X phase is continuously maintained by varying the galvanostatic current as a feedback loop from the electrical resistance of the electrode [86]. Using this technique allows long-term usage for 330 hours with the precision of $\pm 4\ mV$ [87]. Interestingly, in this work it was found that also *initially* charged electrodes demonstrate long-term stability with even enhanced precision by around one order of magnitude, Fig. 3.8 a)-c). Using a standard electrochemical glass cell, both is achieved: long-term stability with more than 843 hours and great precision with a standard deviation σ_X between 0.5 and 0.16 mV. Due to practical reasons, the measurement was paused and continued as indicated by the different sections. Over all sections, there was no need to exchange the electrolyte. A possible pH shift can be excluded due to the non-detectable electrolyte evaporation. For each section, Fig. 3.8 b) and c) shows the corresponding σ_X value and slope from linear fitting. The sections 1 and 2 show the transient in the process of establishing a stable RE potential. Considering the sections 2 to 7, the slope is $4.2E^{-7}\ mV/s$, measured over 843.3 hours. Extrapolating the $\alpha + \beta$ phase towards the onset of the α phase gives a long-term stability of around 3200 hours. In section 7, after 1343 hours, it was decided to end the measurement: The nitrogen flow was stopped and lab air could enter the system. As a consequence, oxygen gas discharged the PdH_X RE,

which increased the potential. For clarification, under normal operation the *in situ/operando* cell is hermetically sealed and no oxygen can enter it, i.e. the RE will not be destabilized. This is why the PdH_X RE is expected to show an even better performance in the *in situ/operando* cell than in the standard electrochemical glass cell. In summary, section 1 and 2 of the tran-

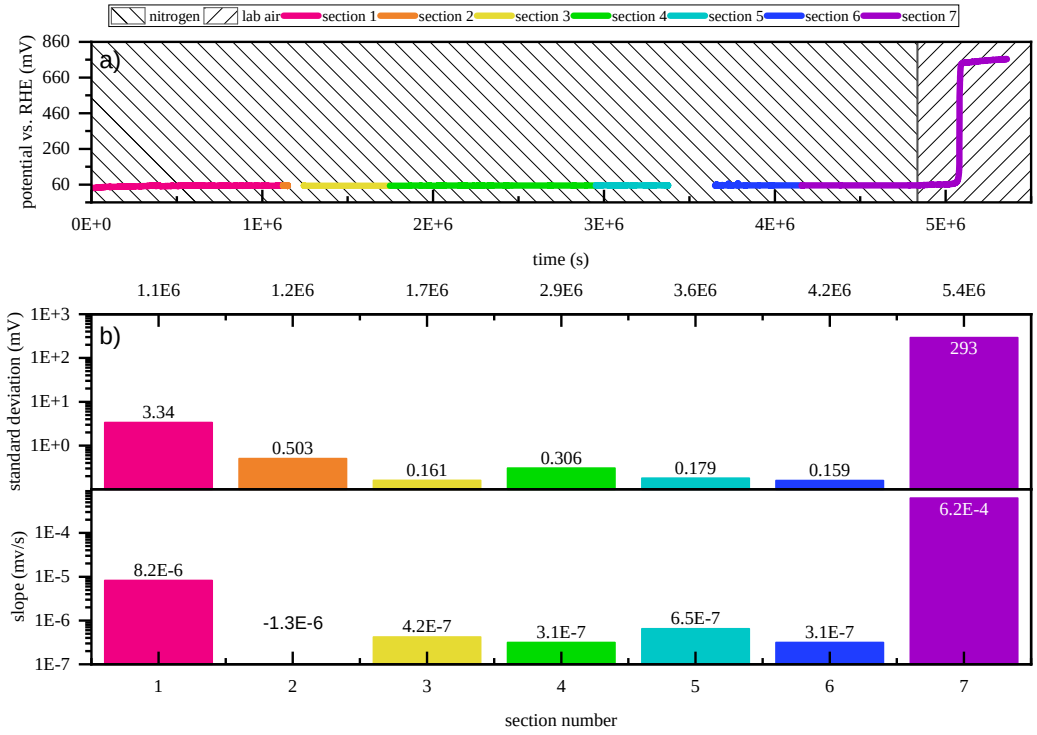

Figure 3.8: Long-term stability and precision of the *initially* charged PdH_X electrode, in 0.1 M H_2SO_4, at room temperature: a) OCP transient, b) statistical evaluation.

sient characterize the stabilization of the PdH_X RE. Section 7 describes a destabilization of the PdH_X RE, caused by oxygen, while the overall process represents a discharge, going ahead with an oxygen reduction reaction. Formally, this process is understood to proceed in a one- or two-step reaction,

with their corresponding standard potentials, Eq. 3.24 and 3.25.

$$O_2 + 4H^+ + 4e^- \rightleftharpoons 2H_2O,\ one\ step,\ \epsilon_0 = 1.23\ V\ vs.\ SHE \tag{3.24}$$

$$\begin{aligned} &O_2 + 2H^+ + 2e^- \rightleftharpoons H_2O_2,\ first\ step,\ \epsilon_0 = 0.682\ V\ vs.\ SHE \\ &H_2O_2 + 2H^+ + 2e^- \rightleftharpoons 2H_2O,\ second\ step,\ \epsilon_0 = 1.77\ V\ vs.\ SHE \end{aligned} \tag{3.25}$$

It is also clear that another reaction has to be considered in order to describe the equilibrium between the absorbed hydrogen H_{ab}, the adsorbed hydrogen H_{ad}, and the hydrogen protons H^+ dissolved in the electrolyte, Eq. 3.26.

$$H_{ab} \rightleftharpoons H_{ad} \rightleftharpoons H^+ + e^- \rightleftharpoons \frac{1}{2}H_2,\ \epsilon_0 = 0\ V\ vs.\ SHE \tag{3.26}$$

Whereas Eq. 3.24 and 3.25 describe the electrode processes on the oxygen electrode, Eq. 3.26 describes the hydrogen electrode in acidic solutions. Since the cell has a modular structure, different kinds of WEs can be used. Therefore, different kinds of reactions appear to be possible. In accordance to enable an easy WE exchange, the cell body, including the RE and CE, is an independent part of the cell construction. Recently, the cell is designed to fit on a SPECS[25] sample holder type SH 2/12 (see Fig. 3.9 3 b)), allowing full transferability and offering great advantages, compared to a static, non-transferable cell, build in place: The cell can be introduced through a LL chamber, separated from other chambers. After the evacuation of the LL, transferring the cell into the preparation chamber offers all conceivable opportunities of surface manipulation, such as cleaning by sputtering or depositing additional electrode material onto the WE. Since the whole cell is UHV compatible, the electrode surface can be modified precisely under the well-defined conditions available in surface science. After the cell is transferred into the analytical chamber, a wide span of complementary methods

[25]SPECS Surface Nano Analysis GmbH.

are available, such as XPS, infrared reflection-absorption spectroscopy (IR-RAS) and KP, which can be used to investigate the electrode surface. As mentioned before, it is easy to exchange the WE, allowing to explore other scientific fields. Hereafter, some examples are given on how the modular structure of the cell can be used with different kinds of WEs. Basically, two groups can be found: *permeation cells*, where the sample (i.e. WE) is a membrane, permeable for hydrogen, and *window cells*, where the sample (i.e. WE) is a window for the applied analytical technique.

3.3.5 *Permeation Cell*

As can be seen from Fig. 3.9, the cell consists of a conventional three-electrode set-up in which the *Fermi level* alignment of the WE and the UHV chamber is allowed when the WE is connected to the ground (GND) of the instrument. On the entry side of the WE, the potential is controlled by a RE, such as a PdH_X RE and a CE, e.g. also PdH_X. Here, the hydrogen uptake is controlled potentiostatically, leading to adsorption (ad) and absorption (ab) on the palladium membrane. The adsorbed hydrogen on the exit side can react with the atmosphere, leading to reactions products such as water. In the permeation configuration, the sample serves as membrane which allows electron exchange on the WE and proton exchange through the WE. For instance, metallic membranes can be used, wherein hydrogen dissolves in the metal. Here, the $Pd-H$-system is of great interest since it shows great hydrogen solubility and fast hydrogen transportation. Using PdH_X as the RE and PdH_{X-Y} as the WE gives great advantage with regard to a possible pH shift of 59 mV per decade. Since a pH shift in the electrolyte would affect both electrodes in the same way, the measured potential can still be referenced against the PdH_X (see Fig. 3.7). Strictly speaking, the intrinsic potential measurement is not affected by a pH change within the cell, because

the polarization of the exit side occurs via the entry side by the change in hydrogen activity $a(H)$ which depends according to the *Nernst* equation for the hydrogen electrode just on the potential difference to the RE, Eq. 3.26 and 6.5. Furthermore, for each H^+ reduced at the WE to H at the CE, an H from the $Pd-H$ phase is oxidized to H^+, i.e. the pH is effectively stabilized.

$$\epsilon = \epsilon_0 + \frac{RT}{F} ln\left(\frac{a(H^+)}{a(H_{ad})}\right) = \epsilon^* + \frac{RT}{F} ln\left(\frac{a(H^+)}{a(H_{ab})}\right) \tag{3.27}$$

In equilibrium, the applied potential at the entry side leads to a corresponding potential on the exit side, Fig. 3.7. This potential formation is understood in the same context as it is described with the electrode processes on the PdH_X RE, Eq. 3.24 - 3.26. In addition, this is also observed for sandwich samples, such as Fe/Pd, e.g. [81, 88]. The oxygen and the hydrogen electrode are of significant economic importance: fuel cells, water electrolysis, metal-air batteries as well as oxygen driven corrosion can be investigated at a fundamental level, on the scale of the electrolytic double layer. Controlling the atmosphere on the exit side, in the range from UHV up to several millibars, an ultra-thin layer of electrolyte can be formed on the exit side [82]. Thus, giving the opportunity to investigate the oxygen- or hydrogen electrode under full potential control. For instance, APXPS is a great tool to perform such investigations since it provides both: adjustable atmosphere and insights into the electronic structure and chemical state present at the surface. Anyhow, this cell is not only restricted for APXPS measurements, it can be used in combination with any analytical surface science tool.

3.3.6 Experiment: Reduction of Palladium Oxide

In order to demonstrate the functionality of the set-up under UHV conditions a fundamental and straightforward experiment will be discussed in the following: Firstly, one side of the polycrystalline palladium membrane (99.95 %

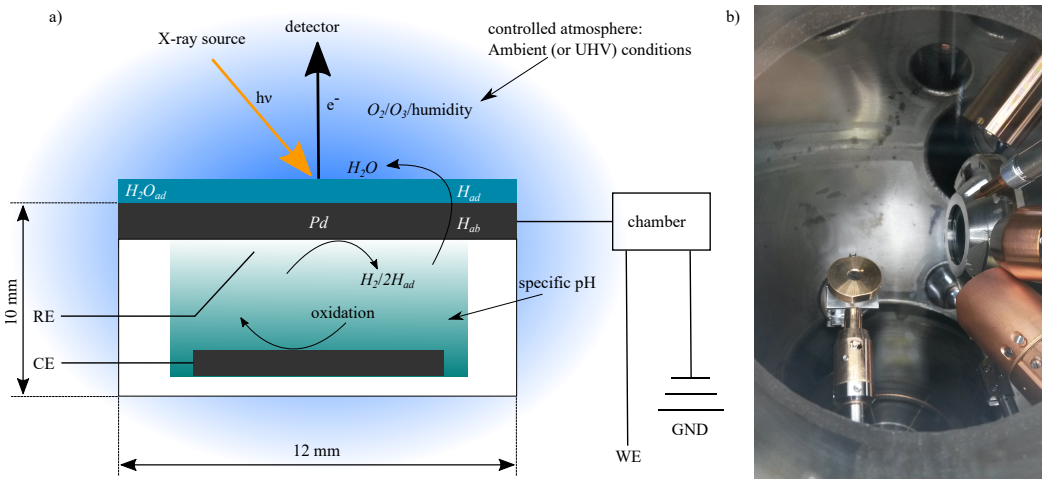

Figure 3.9: *In situ/operando* cell, membrane configuration: a) schematical drawing of the ongoing processes during an electrochemical polarization. b) the *in situ/operando* cell within the analysis chamber of an APXPS instrument.

purity) was anodically polarized in 0.1 M H_2SO_4, at 2000 mV vs. RHE for 2 min. This step was done with an external electrochemical set-up. Secondly, the oxidized side of the palladium membrane was mounted into the transferable EC, as the exit side, to be analyzed by XPS, Fig. 3.10. Spectra were taken, at first, at the OCP (open-circuit potential), not hydrogen loaded, and, at second, while the sample was polarized underneath the reduction peak f) visible in the cyclic voltammogram (CV) shown in Fig. 3.11.

Fig. 3.10 shows the transient of the palladium oxide during its reduction at a potential of 375 mV vs. RHE. In the beginning, each spin orbital consist of two peaks of which the peak at higher binding energies belongs to the oxidized specie. Between 156 and 208 min, the oxidized specie is no more visible, but the lower peak, in relation to the broken line shifts, Fig. 3.10 b). At 1364 min, the palladium is fully reduced, but an 0.5 eV position shift, with

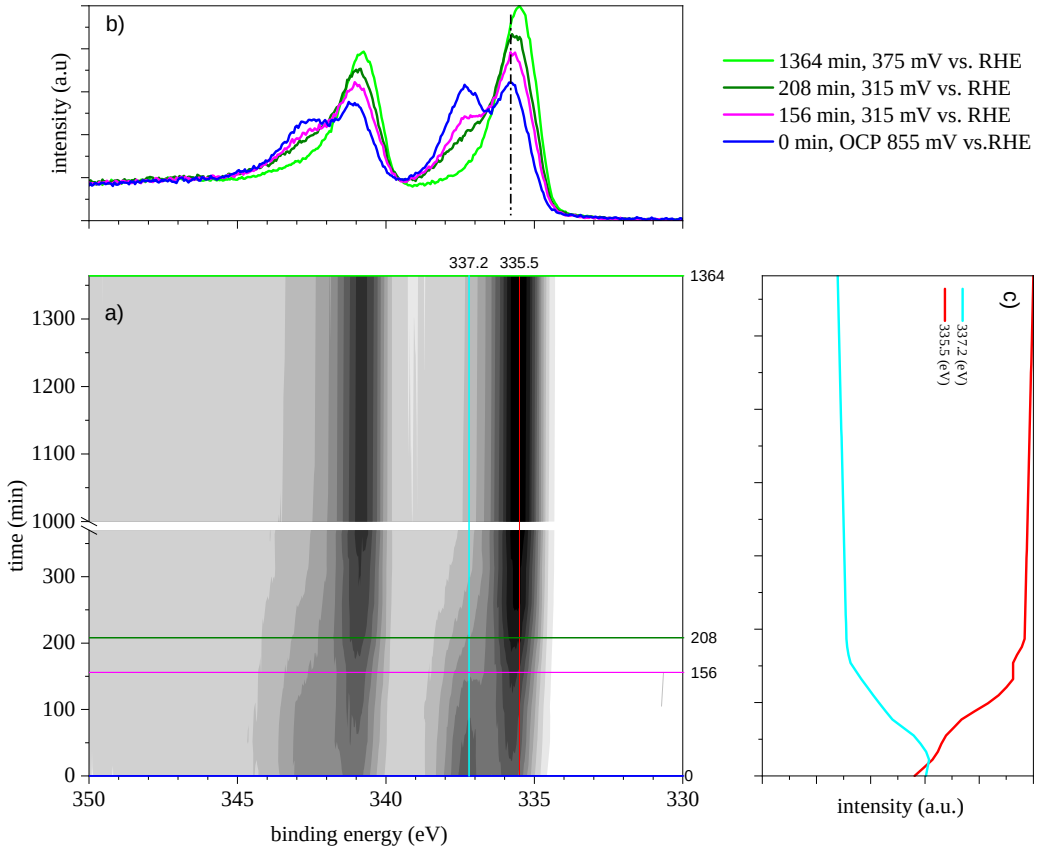

Figure 3.10: Time resolved XPS spectra (monochromatic $Al\ K\alpha$) of 0.5 mm thick palladium membrane at room temperature in UHV ($3E^{-9}$ $mbar$ 2nd generation): a) contour plot of the $3d$ spin orbital in gray scale. Time 0 min is the reference time at the OCP. At times$>$ 0, the WE was polarized to 375 mV vs. RHE, while each 22 min a new XPS spectrum was taken. b) isochronous cross sections for different times and potentials. c) isoenergetic cross sections for different binding energies.

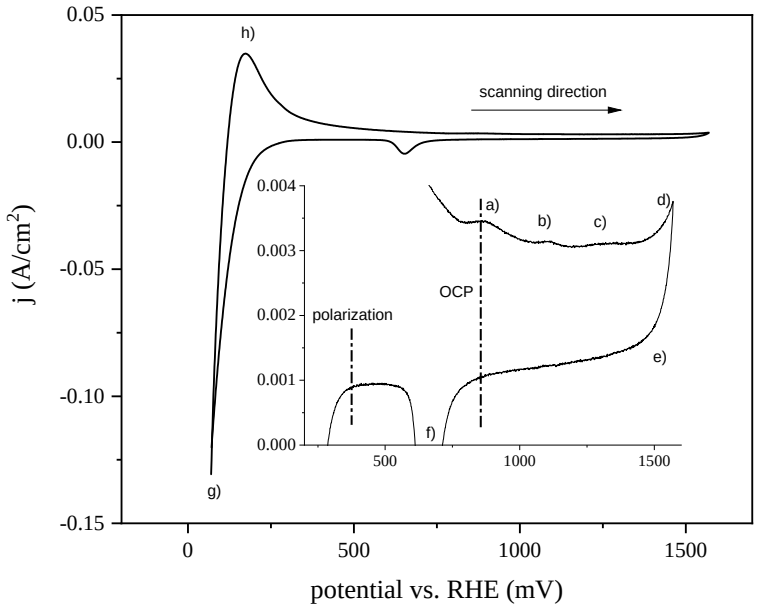

Figure 3.11: CV of the palladium membrane (measured *ex situ* in a standard electrochemical cell): 0.1 M H_2SO_4, scan rate 0.05 V/s, step size 0.001 V. The insert shows a zoom in. The broken lines show the potentials on the entry side of the cell during the measurement, see the spectra shown in Fig. 3.10. a) to d) surface oxide formation, d) to f) surface oxide reduction, g) hydrogen evolution/-absorption, h) hydrogen oxidation/-desorption.

respect to the metallic component at 335.0 eV, can still be observed. The reason for that is not fully clear yet, maybe contamination during long-term experiment plays a role.

When equilibrium is reestablished, the potential at the entry and exit sides are identical in terms of hydrogen activity, i.e. only oxides that are favored to exist under such an equilibrium are present at the exit side. From the XPS spectrum it is difficult to identify the specific palladium oxide. However, it is also likely that mixed oxides were simultaneously present at the surface. Similar XPS spectra of palladium oxides are found in [89], where the palladium foil was electrochemically oxidized at specific times and potentials, followed by XPS analysis. Other investigations were performed in [90], where a new 2D surface oxide was found, formed by heat treatment during molecular oxygen exposure. In addition, the corresponding binding energies are close to each other, as listed in Tab. 3.3. In this work, a precise assignment was, however, not tried as the focus was to elucidate the electrochemical principle and functionality of the cell.

Table 3.3: Binding energies of palladium oxide species. Preparation (Prep.) by: (1) electrochemical oxidation of a palladium foil; (2) heat treatment with molecular oxygen of $Pd(111)$ single crystal.

Species	**Prep.**	$\boldsymbol{Pd\ 3d_{5/2}\ (eV)}$	$\boldsymbol{O\ 1s\ (eV)}$	**Ref.**
PdO_{ad}	(1)	335.6	-	[89]
PdO	(1)	335.3	532.7	[89]
PdO_2	(1)	337.9	-	[89]
Pd_5O_4	(2)	337.9	-	[90]

The data obtained here clearly show that the redox reaction occurring at the exit side can be followed by XPS *in situ*, i.e. an *in situ* investigation by XPS of an electrochemical reaction was performed here. Independently from the actual palladium oxidation state, H, diffusing from the entry to the exit side, reduced the palladium oxide, where PdO is reduced along with the reaction in Eq. 3.28 and PdO_2 along with the reaction in Eq. 3.29.

$$PdO + 2H^+ + 2e^- \rightleftharpoons H_2O + Pd \tag{3.28}$$

$$PdO_2 + 4H^+ + 4e^- \rightleftharpoons 2H_2O + Pd \tag{3.29}$$

The applied potential determines the net direction of the redox reaction. Hence, it is possible to trigger the reduction of palladium oxide potentiostatically. Such an *in situ/operando* investigation was realized here for the first time. Apparently, this feature can be transmitted to other reactions, such as the oxygen- and the hydrogen electrode, Eq. 3.24 to 3.26, see e.g. [91].

3.3.7 *Window Cells*

Another approach for *in situ/operando* investigations are *window cells*. Simply by exchanging the membrane from the permeation cell by a window one obtains a *window cell*. This can be done either by a graphene or by a silicon nitride window, Fig. 3.12. In that configuration, the window provides the separation of the high- and low-pressure side and simultaneously is the electrode or can act as the carrier for the electrode material. Since both X-rays and photoelectrons can pass through the graphene, the emitted photoelectrons can be analyzed by the detector. For electrons with a kinetic energy of 66 eV, the transmission through a single layer graphene (SLG) is 27 % [92]. In order to prevent the SLG window from rupture, a perforated silicon nitride window can be used as a supportive material on the SLG window. It was shown in [93] that SLG can sustain pressure differences in the exceedance of

6 orders of magnitude, allowing atmospheric measurements up to 1500 *mbar*. Besides the impressive mechanical strength, graphene also shows impermeability for liquids and gases [94, 95]. Therefore, graphene can be used as a window material for an electrochemical cell.

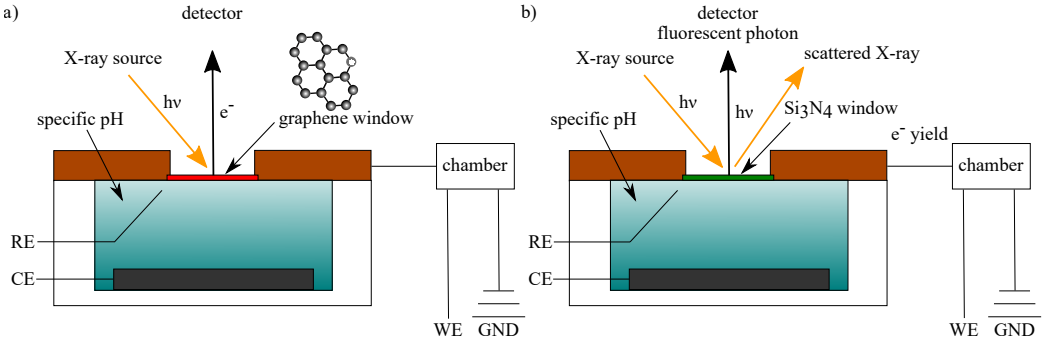

Figure 3.12: *Window cell* configuration for, a) the graphene- and b) the silicon nitride window.

3.3.8 Summary

A novel *in situ/operando* cell was developed which is UHV tight and transferable between different UHV chambers. The cell can be handled just like a normal sample. Thus, *Ar*-sputtering or deposition of other materials, e.g. creating a sandwich sample, is possible. The cell can be used without any modifications of the analytical system. Therefore it is an attractive alternative to other *in situ/operando* set-ups. Further, the UHV equipment is not contaminated with electrolyte, causing damage or the necessity of running a bake-out. From the scientific viewpoint, the cell allows to fully control not only the potential of electrodes covered by just ultra-thin electrolyte layers but also to measure the full $j(\epsilon)$ correlation for electrochemical reactions, such as oxygen reduction on that same electrode. This is a breakthrough of greatest importance in respect to *in situ* monitoring of redox reactions via the whole arsenal of UHV- and electrochemical techniques in combination.

It allows to:

- measure absolute electrode potentials.
- measure $j(\epsilon)$ curves on electrodes covered by ultra-thin electrolyte layers, even down to the sub-monolayer range.
- use analytical surface science tools without any restrictions.
- reveal the chemical species and states.
- characterize the full electrode, as the electrolyte layer is very thin and controllable from clusters over monolayers to nanometers.

Based on the modular structure, the cell can easily be turned into the *window cell* configuration. Thus opening up further possibilities. One single cell can be assembled, tested, and if necessary, transported to different facilities, and so undergo several surface analytical methods which can be then correlated. Thus, the user can perform *plug and play* experiments. In comparison to static assemblies [93, 96], this means a significant simplification in conducting experiments. With regard to time and purity, considering residual gases, there is no need to vent the analysis chamber in respect to adapt the present configuration towards the users' needs. Particularly at synchrotron facilities, beamtime is a valuable resource. Therefore, preserving time for additional data acquisitions is of substantial advantage.

Chapter 4

The Hydrogen Electrode on Palladium

4.1 Sample Preparation

Polycrystalline palladium samples of 99.95 % purity were annealed in HV for 2 h at 600 $°C$. Afterwards, both sides of the palladium membrane were grounded and polished. The last polishing step was accomplished with a 1 micron diamond suspension, resulting in a membrane thickness of 0.08 mm. Sample cleaning was performed going through ultrasonic baths in steps of acetone absolute, detergent and ultrapure water. The EC (see chapter 3.3) was assembled in a glove box, at less than 70 ppm of O_2, purged with wet N_2 at near 100 % r.h.. The electrode arrangement is identical as shown in Fig. 3.9. The EC was evacuated in the LL of the APXPS, and the leak rate, as reported in chapter 3.3.1, was determined. Sample preparation in UHV, i.e. Ar-sputtering, was performed to clean the WE electrode on demand.

4.2 Work Function in UHV

A potential vs. SHE was applied on entry side of the palladium membrane and controlled potentiostatically. As a consequence of the hydrogen charging and some loss into the UHV, the initial base pressure raised from $2.3E^{-10}$ at (352 mV) to $6E^{-10}$ $mbar$ at (51 mV), which indicates very low hydrogen loss. After an equilibration time of 18 h, the exit side of the palladium membrane was sputtered for 10 min with 5 keV Ar ions at a pressure of $1E^{-7}$ $mbar$. With a time difference of 15 min, required to start the X-ray source, the work function was measured firstly with XPS and secondly with UPS. In successive steps, the sample was polarized from 352 mV to 51 mV.

At each potential the above procedure was repeated. All XPS spectra were obtained using a monochromatic *Al* $K\alpha$ light source[1]. The energy scale has been calibrated on the *Fermi edge* of a sputtered *Ag* reference sample. The UPS spectra were obtained using a *He I* light source[2].

Fig. 4.1 shows the work function dependency on applied potential for two independent measurements. For comparision, the work function of UHV-annealed polycrystalline palladium is 4.6 eV for foils [97], 4.95 ± 0.05 eV for thin films [97], generally accepted to 5.00 eV [98, 99] or 5.01 eV [100], i.e. $\approx$ 5 eV [101]. Annealing palladium films at different temperatures results in work functions ranging from 4.9 to 5.22 eV [102]. In the situation here, the value of 5.0 eV for UHV-annealed polycrystalline palladium is assumed at low hydrogen activities. At high hydrogen activities and potentials lower than 200 mV, the work function increases about 0.276 eV and 0.233 eV for XPS- and UPS measurements, respectively. From [103] it is known that UPS can result in a lower work function of up to 0.5 eV, qualitatively confirming the results obtained here. Besides that, traces of impurities in the UHV can lead to surface adsorption, and thus alter the work function [104]. In surface science, a rough estimate of the required time to form one monolayer is 1 s at a pressure of $1E^{-6}$ $mbar$. Therefore it takes about 2300 s to form a monolayer at the pressure of $4.3E^{-10}$ $mbar$. Indeed, this is not enough time to perform one high-resolution work function measurement. For this reason, the *time effect* on the work function measurement was investigated on a second sample, Fig. 4.2 and 4.3. For that sample a similar procedure was used, including polarization and *Ar*-sputtering. Different from before, time resolved work function measurements were performed. Followed by the

[1] $h\nu = 1486.71$ eV.
[2] $h\nu = 21.2$ eV.

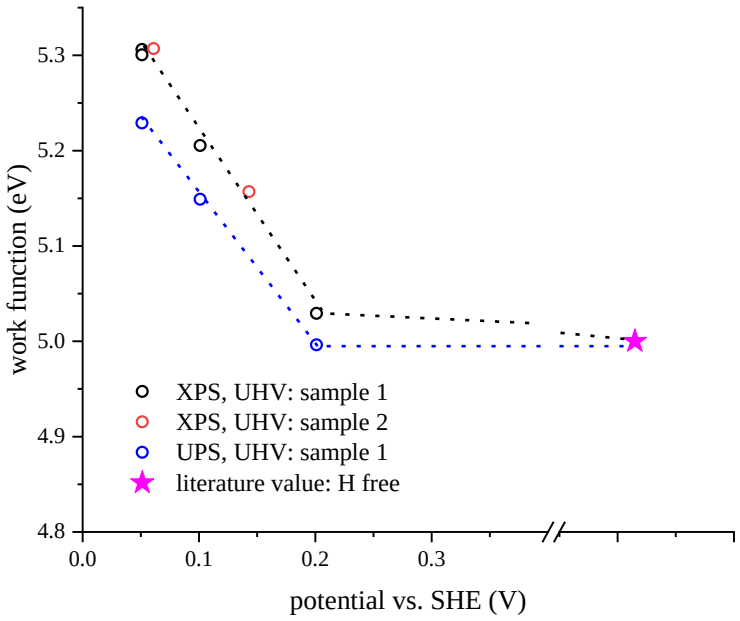

Figure 4.1: Work function of the hydrogen electrode for two independent measurements in UHV, right after *Ar*-sputtering.

polarization to 143 mV, the potential was changed at time zero to 61 mV and the cut-off was continuously tracked with a tradeoff in resolution, Fig 4.2. With a time lag of about 1000 s, the work function starts to increase linearly on a logarithmic time scale, Fig. 4.3. The next day, while the sample was continuously polarized in UHV, the work function of the non-sputtered sample was measured again and it is found that the previous increase equals about two times the present decrease, Fig. 4.3. Repeating the work function measurement on the freshly sputtered sample gave the result at 61 mV, as shown in Fig. 4.1 and labeled as *sample 2*. A comparison of the results from *sample 1* and *2* indicates a high degree of reproducibility.

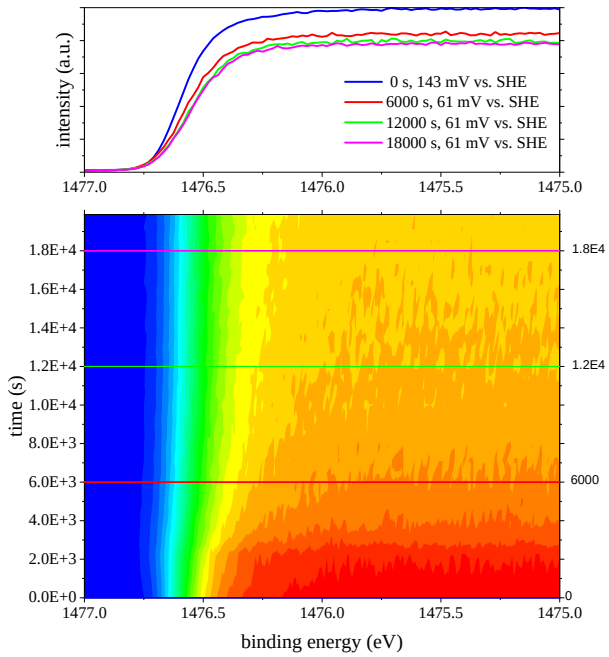

Figure 4.2: Time dependent XPS measurement of the cut-off and the effect of polarization.

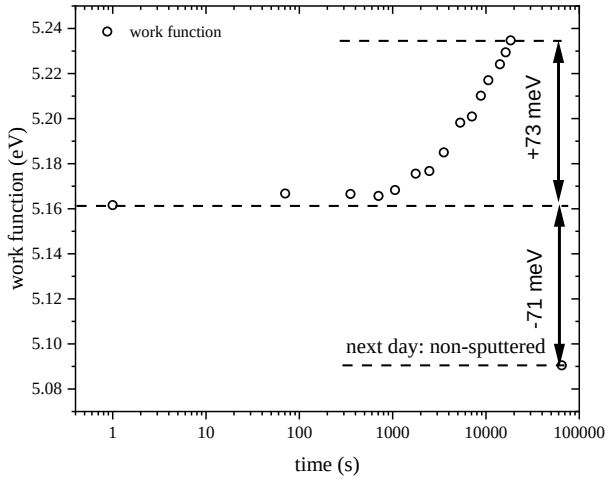

Figure 4.3: Time dependent XPS measurement of the work function in response to a sudden polarization change ($143 \rightarrow 61\ mV$) introduced at time zero.

4.3 Effect of Carbon Species

As mentioned in chapter 4.2, trace amounts of residual gases in the UHV can alter the work function [104]. Typically, a residual gas of an UHV chamber, when measured with a mass spectrometer, is found to be mainly composed of H_2, CO, CO_2, where minor portions are detected for H_2O and its OH fragment [79]. Hydrocarbons are effectively extracted by turbo molecular pumps [79] and minimized by the usage of dry scroll pumps. Both applies for the UHV system used in this work. Anyway, exposing a clean surface to UHV leads to trace impurities on the surface after a certain time. CO is known to adsorb on palladium single crystals [105, 106]. CO_2 adsorption is found on palladium dispersed on various supports, while in presence of H_2 the CO_2 uptake was enhanced [107]. Infrared spectroscopic measurements showed that adsorbed CO and $HCOO^-$ are formed by surface interaction of H_2 and CO_2 [107]. In application, palladium is well known as an excellent catalytic converter for CO into CO_2, which is commonly used in a three way catalytic converter for exhaust gases, see [108].

Indeed, the $C\ 1s$ spectra in Fig. 4.4 show a response, i.e. a change as a function of applied potentials, and thus on the hydrogen activity. Since the palladium sample was sputtered several times, without leaving the UHV system, the carbon source must be the UHV system itself; therefore considered as internal carbon contamination. Fig. 4.4 shows distinct $C\ 1s$ peaks, labeled by its peak number p_i. Comparing the overlay from spectrum (1) and (3), one sees an increase of the peaks p_2 and p_3 when the potential is decreased, Fig. 4.4.

Another source of carbon, which is assigned to external carbon, can be identified when the sample is introduced from outside into the UHV system and

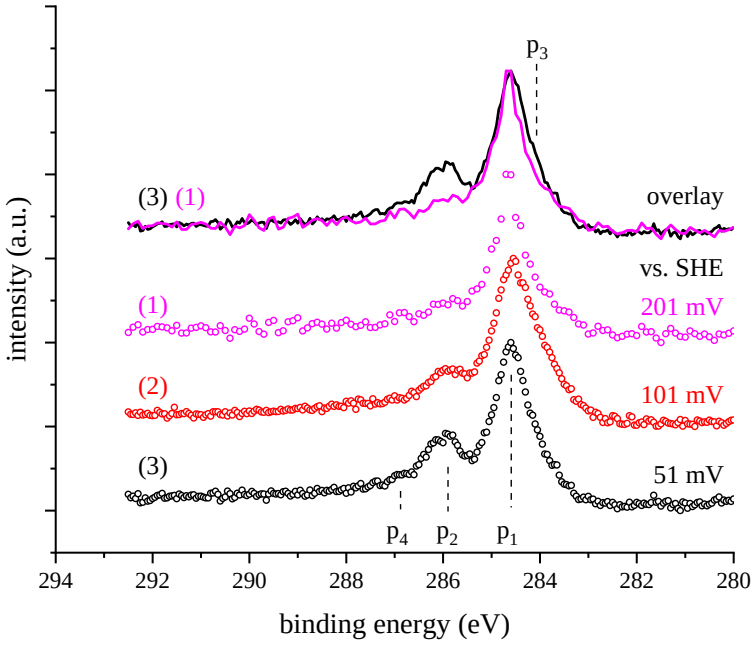

Figure 4.4: Internal carbon from UHV: $C\ 1s$ spectra that show impact on the applied potential. The number in brackets corresponds to the chronological order of the measured spectra.

no Ar-sputtering is performed. The new peak p_5, assigned to external carbon, is found. Anyway, the C $1s$ shows a similar dependency on the applied potential: p_5, p_n including p_2 and p_3 decrease when the potential is raised, Fig. 4.5.

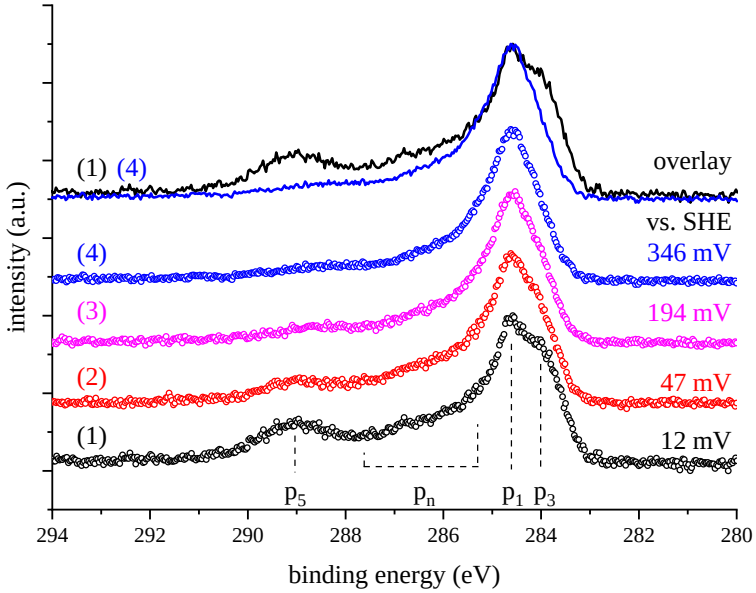

Figure 4.5: External carbon: C $1s$ spectra that show a dependency on the applied potential. The number in brackets corresponds to the chronological order of the measured spectra.

The reversibility of the C $1s$ spectra, as a reaction on the applied potential, was checked by re-polarizing the sample from 352 mV back to 10 mV. Comparing the spectrum (1) and (5) in Fig. 4.6, partial reversibility is found, where the differences are rather in the intensity than in the presence of the peaks.

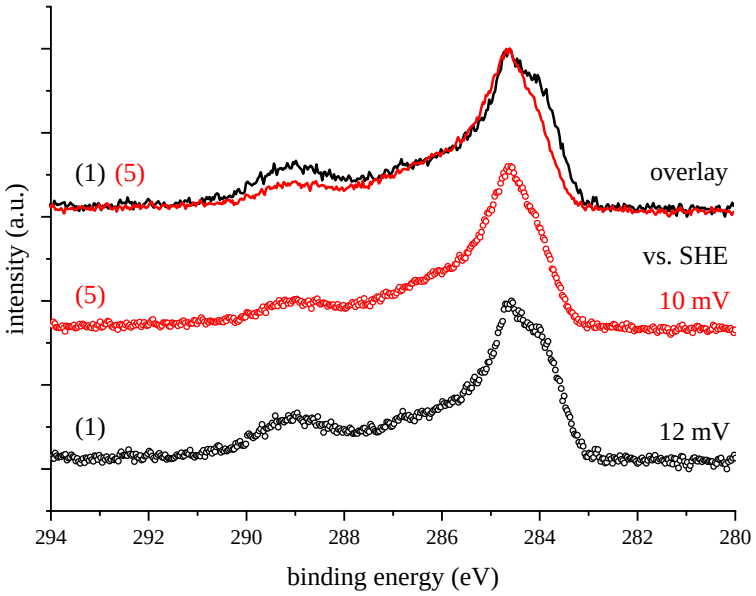

Figure 4.6: External carbon: C $1s$ spectra that show partial reversibility in the formation of carbon species at similar potentials. The spectrum at 12 mV is the same as shown in Fig. 4.5. The spectrum at 10 mV was taken after polarization to 346 mV. The number in brackets corresponds to the chronological order of the measured spectra.

4.4 Hydrogen Electrode in Water Vapor

The hydrogen electrode as the *"electrode in the dry"* originates from KP measurements in *"dry"* nitrogen gas at 1 atm [81]. Even though these measurements were performed in controlled conditions, a direct comparison to UHV conditions is not possible. Besides impurities, referring to external carbon, *"dry"* nitrogen still contains trace amounts of water in the order of 0.25 $mbar$. For that reason, it was decided to approach these conditions in a first experiment for the non-sputtered sample in UHV, in a second experiment for the non-sputtered sample in 0.25 $mbar$ water vapor, reflecting *"dry"* conditions from the KP measurements in [81], and in a third experiment for

the Ar-sputtered sample in 0.25 $mbar$ H_2O $mbar$ vapor.

A leak valve was used to supply water vapor. The leak valve is connected via an evacuable[3] and bakeable gas line to a glass flacon. Ultrapure water was filled into the glass flacon and degassed by the freeze-pump-thaw technique. In the last degassing cycle, the frozen water was degassed to a pressure of $4E^{-6}$ $mbar$ while cooled with liquid nitrogen.

At low hydrogen activities, i.e. applied potentials down to $\approx 300\ mV$ vs. SHE, three days under continuous polarization were waited for each potential step to establish equilibrium across the entry- and exit side of the palladium membrane. At potentials lower than 300 mV, equilibrium is reached faster, and only two days were waited.

In order to start the experiment at low hydrogen activities, an initial dehydrogenation process was performed: By means of the $C\ 1s$ spectra in Fig. 4.7, when the WE was the first time polarized to 745 mV, clear differences appear on the first and second day. No further differences are observed on the third day, elucidating that equilibrium is established.

The first experiment was started at 745 mV and subsequently polarized more cathodically. After an initial work function increase, a $1:1$ relation on the applied potentials is obtained, Fig. 4.8.

At the last polarization step, the second experiment was started by dosing 0.25 $mbar$ of water vapor into the reaction chamber. In consequence, the work function is shifted about -61 meV on the axis intercept. From there on, the potential was subsequentially raised. Also here a $1:1$ relation is found, leveling out at 4.39 eV, Fig 4.8.

[3]By turbo molecular pump.

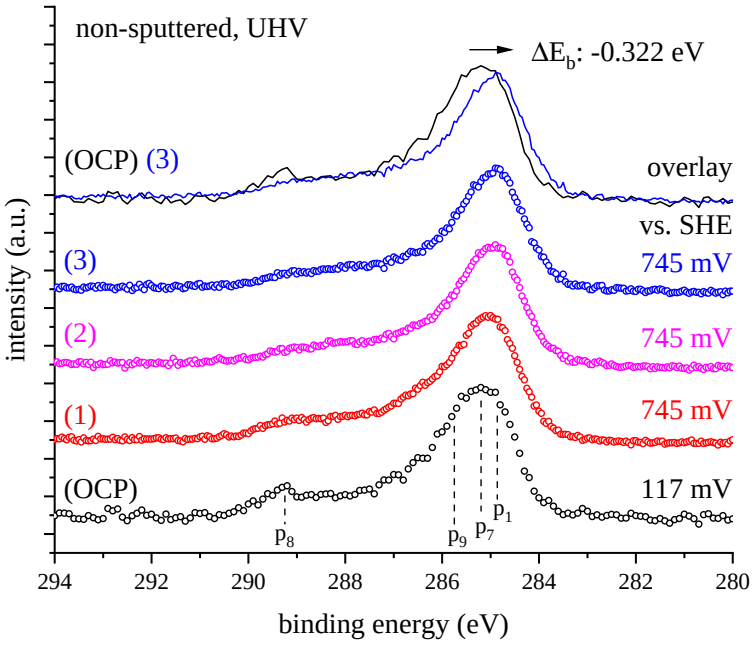

Figure 4.7: Dehydrogenation and the effect on the C $1s$ spectra due to polarization. (OCP) before polarization. Days after the start of 745 mV polarization: (1) first -, (2) second -, and (3) third day.

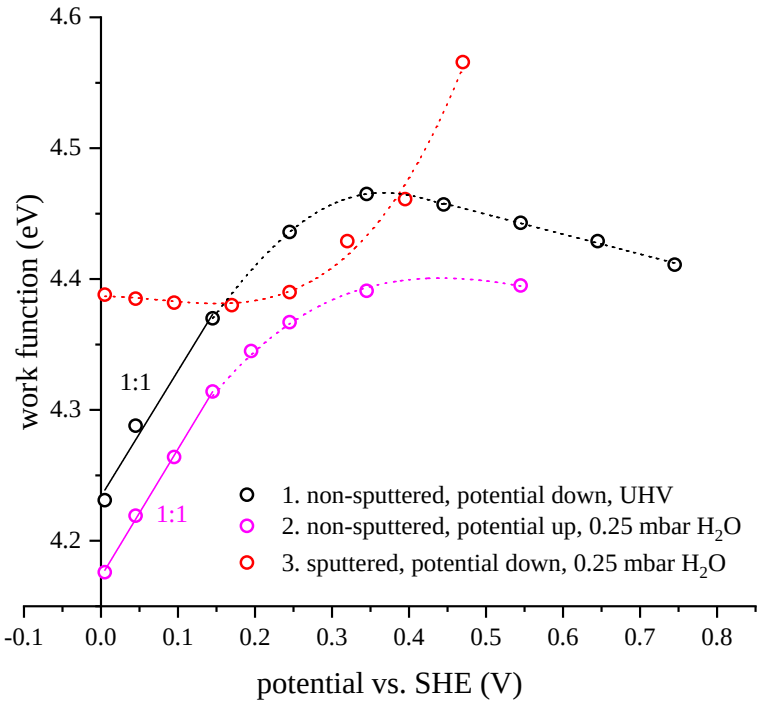

Figure 4.8: The work function of the hydrogen electrode at different potentials. Firstly measured on the non-sputterd sample in UHV. Secondly measured on the non-sputtered-sample in 0.25 *mbar* water vapor. Thirdly measured on the sputtered sample in 0.25 *mbar* water vapor.

In the third experiment, the EC was transferred from the reaction cell into the UHV of the preparation chamber, where Ar-sputtering was performed while the sample was polarized to 456 mV. Again back in the reaction chamber, water vapor was dosed to 0.25 $mbar$. Initially the work function decreased until its infection point at $\approx 200\ mV$, followed by a slight increase and reaching the intercept at the value pair of (4.39 eV;0 mV).

A general trend for work functions is found by comparing the results from the Ar-sputtered sample (UHV/water) and non-sputtered samples (UHV/water): Carbon species, water or hydroxyl adsorption lower the work function of about 0.45 eV to 0.6 eV, see Fig. 4.1 and 4.8.

The $C\ 1s$ spectra for high and low potentials are shown in Fig. 4.9. Considering the overall intensity, it is found that water exposure increases the total carbon amount, whereas the carbon amount stays the same in UHV. On the sputtered electrode, referring to internal carbon, the carbon is significantly altered and only a minor influence is found in dependency of the applied potential, i.e. hydrogen activity. For the non-sputtered electrode a similar trend as before is found: The increase of hydrogen activity shifts the main peak position to higher binding energies and further produces carbon species with a binding energy in the range of $286 - 290\ eV$. In general, water seems to have a moderating influence on the overall change of the $C\ 1s$ spectra.

On the $Pd\ 3d_{5/2}$ spectrum, characterized as the most intense peaks among the XPS Pd peaks, a clear difference is found upon Ar-sputtering, Fig. 4.10. For the sputtered sample, the peak at $335.0 - 335.1\ eV$, coinciding with the peak position p_1 for clean palladium, see **Appendix A** Fig. A.1, is reduced while the peak p_2 at 335.6 eV becomes clearly visible, attributed to PdO_{ad} in [89]. In the present case, p_2 is attributed to water adsorption.

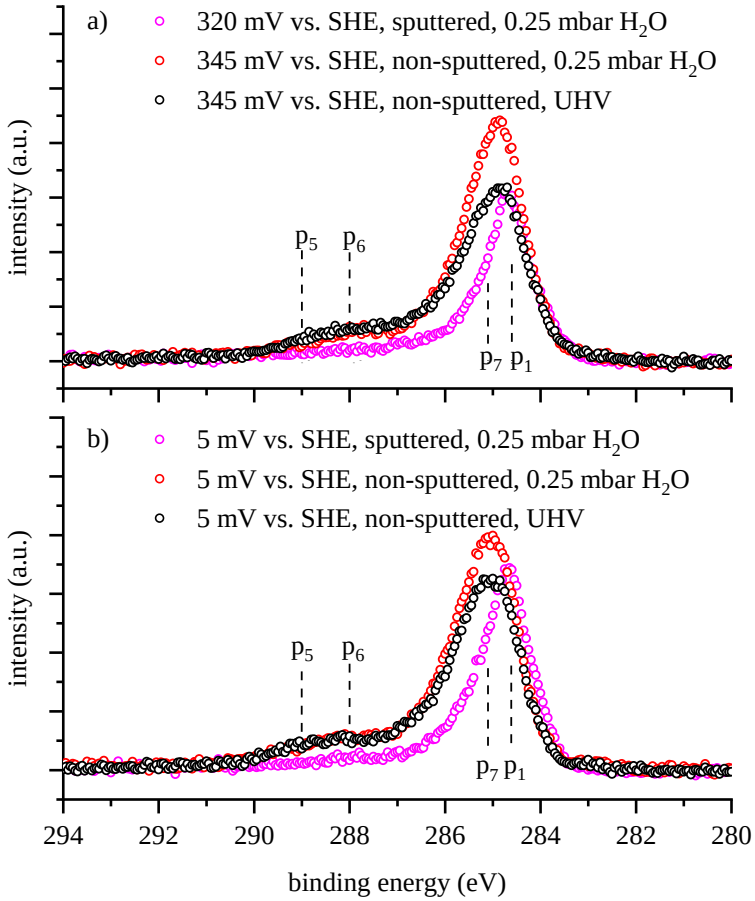

Figure 4.9: *C* 1*s* spectra under different conditions: a) low hydrogen activity, b) high hydrogen activity.

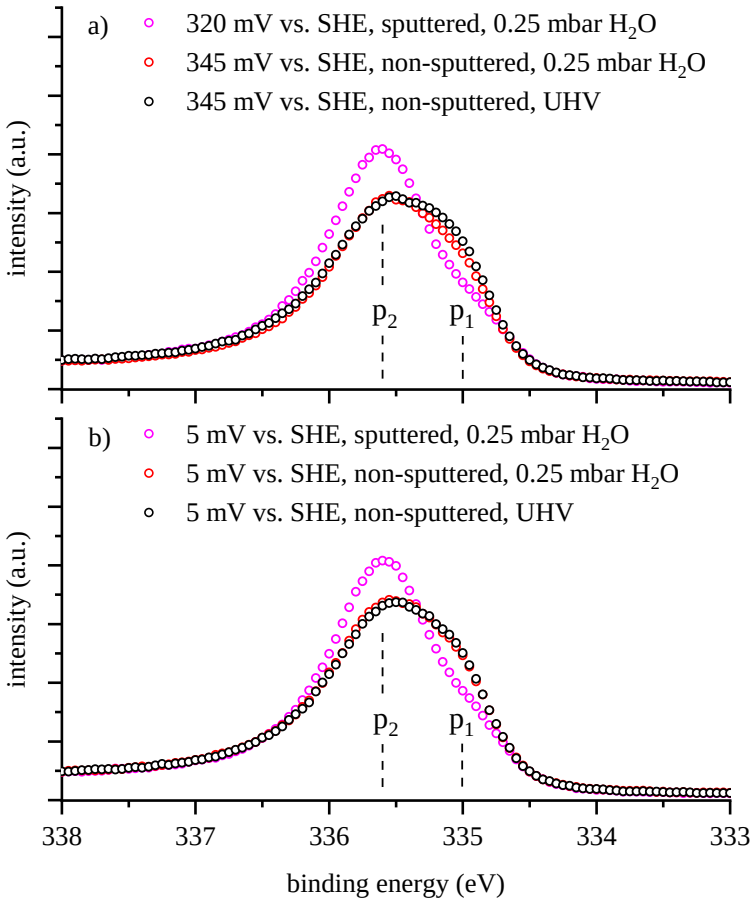

Figure 4.10: *Pd* $3d_{5/2}$ spectra under different conditions: a) low hydrogen activity, b) high hydrogen activity.

The $O\ 1s$ matches the peak position of the $Pd\ 3p_{3/2}$ at $\approx 532\ eV$. Thus, it is difficult to resolve the $O\ 1s$ of water related species from the high metallic *background* of the $Pd\ 3p_{3/2}$. As a result of the *j-j coupling*, the $Pd\ 3p_{1/2}$ and $_{3/2}$ spin orbital have a fixed ratio of $1:2$. To separate the $O\ 1s$ contribution from the $Pd\ 3p$, the method of incremental difference spectra, implemented in *CasaXPS* [109], is applied. Here, the incremental step is set to 0.1. The zeroth increment starts at 0, referring to 100 % of spectrum A, and ends at 100, referring to 100 % of spectrum B.

Fig. 4.11 compares the $Pd\ 3p$ spectra of the non-sputtered (spectrum A) and sputtered sample under the influence of water vapor (spectrum B). When measured with water vapor, the incremental difference spectra in Fig. 4.11 reveal an increased amount of oxygen containing species, labeled as p_1 and p_2. At the $480th$ increment, the $3p_{1/2}$ contribution is canceled out, meaning that the palladium contribution to the $O\ 1s$ is fully compensated. Further, on the $518th$ increment, the peak p_1 becomes more pronounced. The water amount shown by the incremental difference spectra is underestimated here: Since for the non-sputtered sample, an already adsorbed water layer is realistic, it partially cancels out by the incremental difference spectra. A calculation of the difference spectra with a water- and carbon-free palladium reference spectrum results in a more explicit water signal but would have an additional carbon contribution to the $O\ 1s$ that is minimized in the other way.

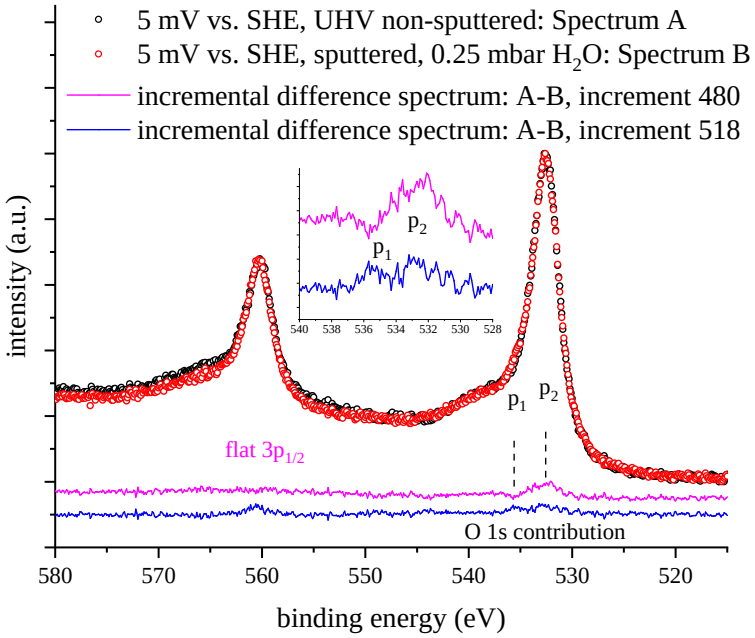

Figure 4.11: *Pd* 3*p* spectra under the influence of water vapor.

Chapter 5

The Hydrogen Electrode on Iron Oxides

5.1 Iron Oxides: Reference Spectra

Numerous studies have been done on the Fe/O system, and extensively investigated with XPS [110, 111, 112, 113, 114]. Regarding the different oxides, Fe_2O_3, Fe_3O_4, and FeO exist only under well defined conditions of temperature and oxygen pressure [115]. The most challenging part to obtain reliable reference spectra consists in a proper sample preparation. Some impairments have to be accepted due to *ex situ* sample preparation and in-UHV investigation. From the perspective of thermodynamics, conventional XPS in UHV does not allow to observe the different oxides under equilibrium conditions. Up to now, data collected in thermodynamic equilibrium cannot be found in the literature. With the help of the APXPS, O_2 can be used to form the corresponding equilibrium oxide while chemical states can be traced with spectral information as well as identified in the same manner. Further, different iron oxides can be formed from just one sample. Thus, enabling full comparability.

First, 99.95 % pure polycrystalline iron was grinded and polished in several steps. The last step, performed with a 1 micron diamond suspension, resulted in a mirror like finish. *Type K* thermocouples were used to measure the sample temperature, not directly on the sample but close to the sample on a mask that holds the sample. An IR laser, focusing on the backside of the sample holder, was used to heat the sample. All XPS spectra were obtained

using a monochromatic *Al* $K\alpha$ light source[1], with the energy scale calibrated on the *Fermi edge* of a sputtered *Ag* reference sample.

To remove native oxides and carbon contamination, the sample was heated in UHV to 750 $°C$. Further on, the sample was cooled to 100 $°C$, and the metallic iron spectrum of the $2p$ spin orbital was measured, Fig. 5.1 and 5.2. Heating the metallic iron sample to 637 $°C$ at a pressure[2] of $2E^{-8}$ $mbar$ O_2 led to the formation of non-stoichiometric $Fe_{1-x}O$. After 3 hours at stable conditions, the $Fe_{1-x}O$ spectrum was measured, Fig. 5.1 and 5.2. Cooling the sample while the O_2 pressure was maintained, the stoichiometric Fe_2O_3 was measured at 100 $°C$, Fig. 5.1 and 5.2.

From the phase diagram in [110], $Fe_{1-x}O$ is thermodynamically stable at temperatures above 570 $°C$ and oxygen pressures at less than $1E^{-17}$ $mbar$. For that reason, the observed $Fe_{1-x}O$ should not exist. Anyway, as it is reported in [116], $Fe_{1-x}O$ is obtained at 700 $°C$ by an oxygen treatment at 1 $torr$ for 10 min. Transformation to Fe_3O_4 proceeds at tempertures as low as 402 $°C$. Besides that, it is found that a LEED[3] pattern of $Fe_{1-x}O$ is formed on a (100) surface exposed to $55E^{-6}$ $torr$ s at room temperature and subsequentially heated to 550 $°C$ [117]. It is also found that this $Fe_{1-x}O$ is stable at room temperature [117]. Even much higher oxygen exposures, in the range of $1E^{-6}$ $torr$ and at room temperature, followed by an UHV anneal at 550 $°C$ results in the formation of a thin film of $Fe_{1-x}O$ [118]. Obviously, the literature is inconsistent about the formation condition but consistent about the XPS spectra of the different oxides. Based on line shapes, peak positions, and satellite structures of the different oxides, the *in*

[1] $h\nu = 1486.71$ eV.
[2] Measured at p_1, see Fig. 3.4.
[3] Low-energy electron diffraction.

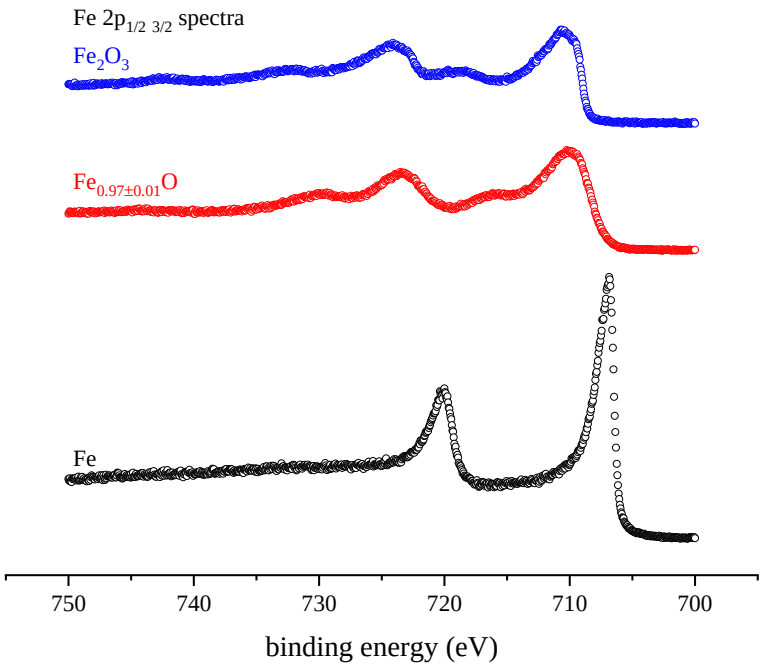

Figure 5.1: APXPS spectra of the Fe $2p$ doublet under different conditions in equilibrium with the gas phase or UHV: Fe: Metallic iron in UHV at 100 $°C$. $Fe_{0.97\pm0.01}O$: Wüstite in $2E^{-8}$ $mbar$ O_2 at 637 $°C$. Fe_2O_3: Hematite in $2E^{-8}$ $mbar$ O_2 at 100 $°C$.

situ/-equilibrium spectra in Fig. 5.1 are consistently in agreement to those reported literature [110, 111, 112, 113, 114].

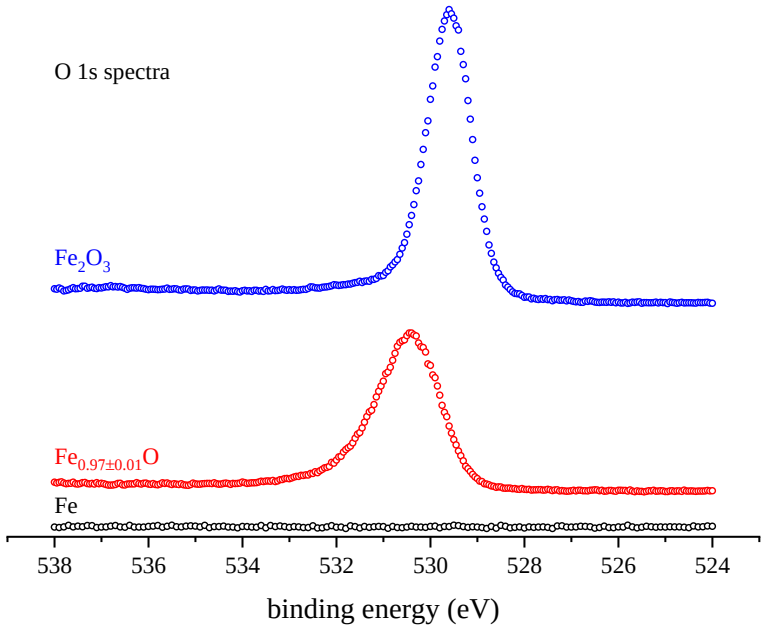

Figure 5.2: APXPS spectra of the iron O $1s$ under different conditions in equilibrium with the gas phase or UHV: Fe: Metallic iron in UHV at 100 $°C$. $Fe_{0.97\pm0.01}O$: Wüstite in $2E^{-8}$ $mbar$ O_2 at 637 $°C$. Fe_2O_3: Hematite in $2E^{-8}$ $mbar$ O_2 at 100 $°C$.

Comparing the O $1s$ in Fig. 5.2, there is a clear chemical shift indicating the different iron oxides. Unfortunately, only few information for the O $1s$ peak position is available. Compared to the results in [113], the peak maximum of the O $1s$ of $Fe_{1-x}O$ is at the same position (529.9 eV). When compared to the O $1s$ of Fe_2O_3, 530.0 eV is reported in [113], whereas 530.5 eV is observed here. The values in [113] indicate that there is almost no difference to $Fe_{1-x}O$. Indeed, a shift of 0.5 eV to higher binding energies might be an effect of charge accumulation on the sample. However, the same effect

should be obtained on the Fe $2p$ spectrum. This is not the case. The values from [113] are *ex situ* data and might not be transferable on *in situ/-equilibrium* conditions.

From the peak area of the Fe $2p$ and O $1s$, the stoichiometry for the $Fe_{1-x}O$ can be calculated to $Fe_{0.97\pm0.01}O$. Literature values are in the range of 0.84 to 1.1 [113, 114].

5.2 Sample Preparation

A polycrystalline palladium membrane of 99.95 % purity was used as substrate for the iron electrode. Both sides of the palladium membrane were grinded and polished. The last polishing step was accomplished with a 1 micron diamond suspension, resulting to a membrane thickness of 0.08 mm. Sample cleaning was performed going through ultrasonic baths in steps of acetone absolute, detergent, and ultrapure water.

The iron electrode was prepared by physical vapor deposition on one side of the palladium substrate. To ensure a good adhesion, the palladium membrane was heated for 2 h at 600 $°C$ in HV to remove any surface contamination, followed by iron deposition at 150 $°C$. The iron layer thickness was controlled with a quartz microbalance[4]. A closed iron layer was obtained on top of the palladium, confirmed by XPS see Fig. 5.3. According to the quartz microbalance, the iron layer is 10 nm thick.

The EC (see chapter 3.3.2) was assembled in a glove box with less than 70 ppm of O_2, and purged with wet N_2 at near 100 % r.h.. The electrode arrangement is identical as shown in Fig. 3.9. After sealing the EC, it was ready to be transferred into the APXPS instrument. UHV conditions were

[4]Calibrated for iron.

maintained. In order to oxidize the iron layer, the sample was polarized to 584 mV vs. SHE while treated with a mixture of O_2/O_3 in the ratio of $50:1$ at 20 $mbar$. This treatment was repeated a second time but polarized to 734 mV vs. SHE. As shown in Fig. 5.4, the oxidation process leads to significant changes in the $Fe\ 2p$ spectra, still showing the metallic component and features from the $Fe_{1-x}O$ and Fe_2O_3 reference spectra that indicates the presence of the a mixed oxide Fe_3O_4, but favorably turned towards Fe_2O_3.

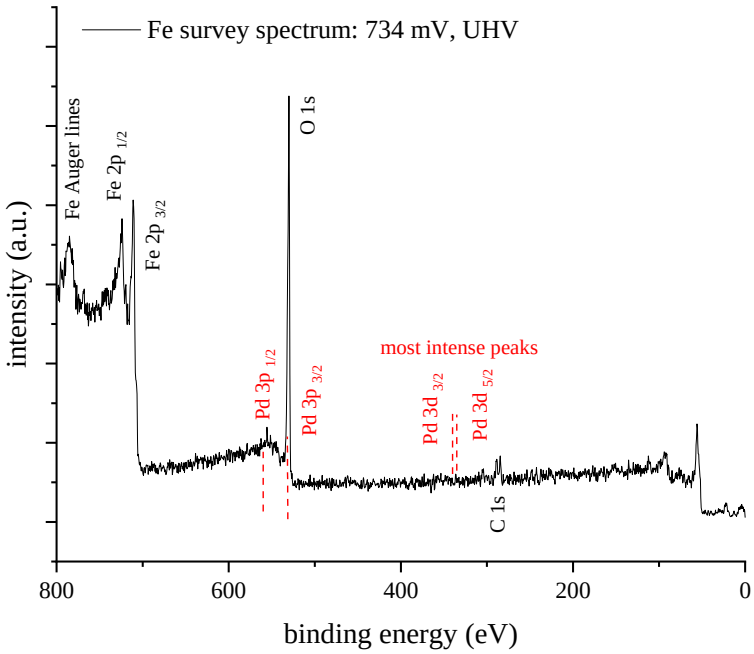

Figure 5.3: APXPS survey spectrum of a closed, 10 nm thick iron layer on top of a palladium membrane. The dashed red lines indicate presumptive palladium peak positions, if they were present.

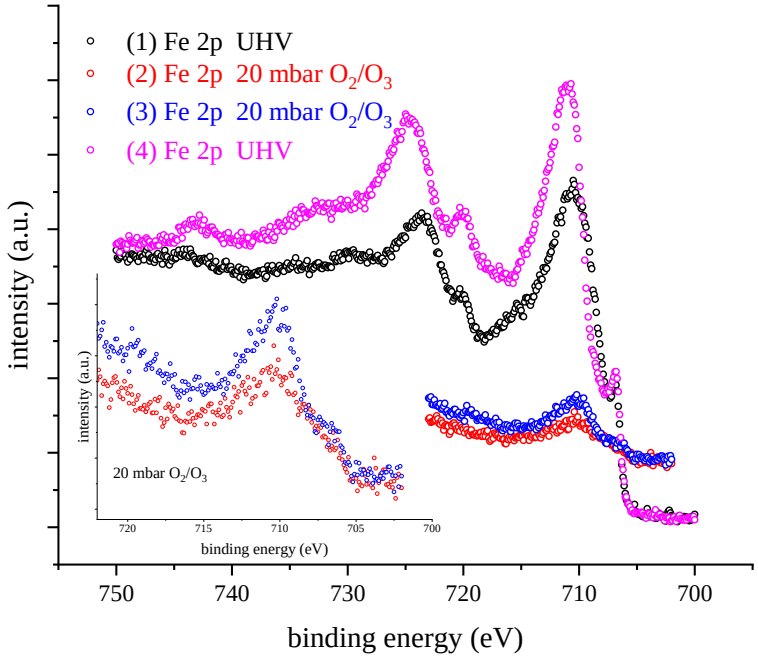

Figure 5.4: APXPS spectra of a 10 nm thick iron layer on top of a palladium membrane while polarized to 734 mV vs. SHE: before (1), during (2) (beginning), (3) after 6.8 h, and (4) UHV after the treatment with a mixture of O_2/O_3 gas in the ratio of 50 : 1 at a total pressure of 20 $mbar$. The insert shows spectrum (2) and (3). The intensity loss is due to electron scattering on the gas molecules.

5.3 Work Function in UHV

After the second treatment in O_2/O_3, the sample was polarized subsequently from 734 to -116 mV vs. SHE in UHV. For each potential step, the sample was allowed to equilibrate for two days. In equilibrium, the iron $2p$ doublet, *Fermi edge*, and the cut-off energy was measured with the APXPS.

In dependency of the applied potential, the work function shows three different regions, Fig. 5.5: the first region from ≈ 0.8 to 0.4 V shows a linear relation with a slope of 1.02 ± 0.0621 eV/V, followed by a second region (transition), followed by a thrid region with a linear relation and a slope of 0.969 ± 0.06 eV/V. At 0 mV vs. SHE, a linear fit of the third region gives a work function of 4.4 ± 0.00473 eV on the intersection. Significant changes in the Fe $2p$ doublet spectra are observed, Fig. 5.6. Here, a peak model of only three independent components are used to approximate the complex line shape of the measured Fe $2p$ doublet, including photoemission peaks, satellites, and multiplet splitting [119]. In comparision to [120], 12 peaks are required to fit the first spin orbital over the range from 705 to 715 eV. In order to exclude arbitrariness by using 12 or at least 24 peaks over the full range of the $2p$ orbital, a different and more significant peak model has to be used.

In fact, the measured iron reference spectra entail the full set of information, whose line shapes for Fe, $Fe_{0.97\pm0.01}O$ and Fe_2O_3, shown in Fig. 5.1, are used to fit the mixed iron oxide spectra. Fitting was performed with *CasaXPS* [109], including the use of the *U 2 Tougaard* background [121] for inelastic photoelectron scattering. The fitting comprises a linear combination of the pure components. Each component represents a chemical state of Fe^{z+}. Fe_2O_3 is a stoichiometric phase with a chemical state of $z = 3$. $Fe_{0.97\pm0.01}O$

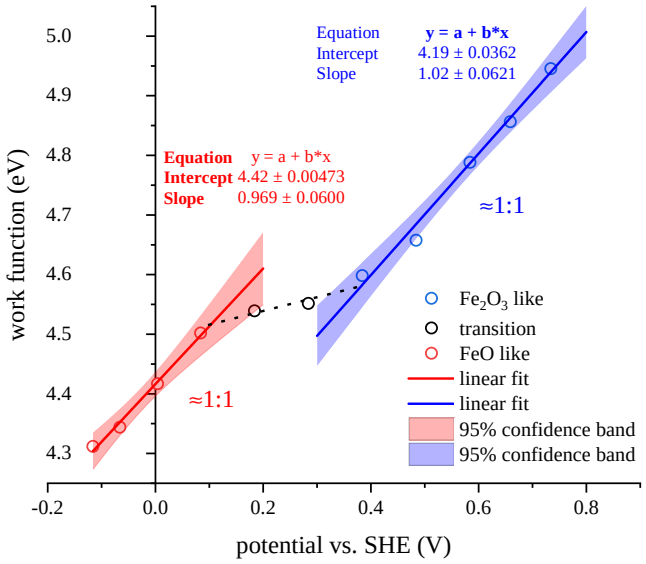

Figure 5.5: The work function measured by XPS as a function of the applied potential. Subsequent polarization from high to low values.

is a non-stoichiometric phase, consisting of two chemical states $z = 2$ and $z = 3$ in combination. Since the net charge must be zero in any combination, the chemical states of $Fe_{1-x}O$ must be composed of $Fe^{2+}_{1-3x} + Fe^{3+}_{2x}$. In order to obtain a true quantification for the electrode composition, a correction for mixed chemical states is performed, giving the result shown in Fig. 5.7. Comparing Fig. 5.5 and 5.7, a plateau at $\approx 0.25\ V$ exists where a correlation of work function and electrode composition is found. This behavior even becomes more clear by comparing the Fe_2O_3/FeO ratio with the work function, Fig. 5.8. Unambiguously a linear relationship is found.

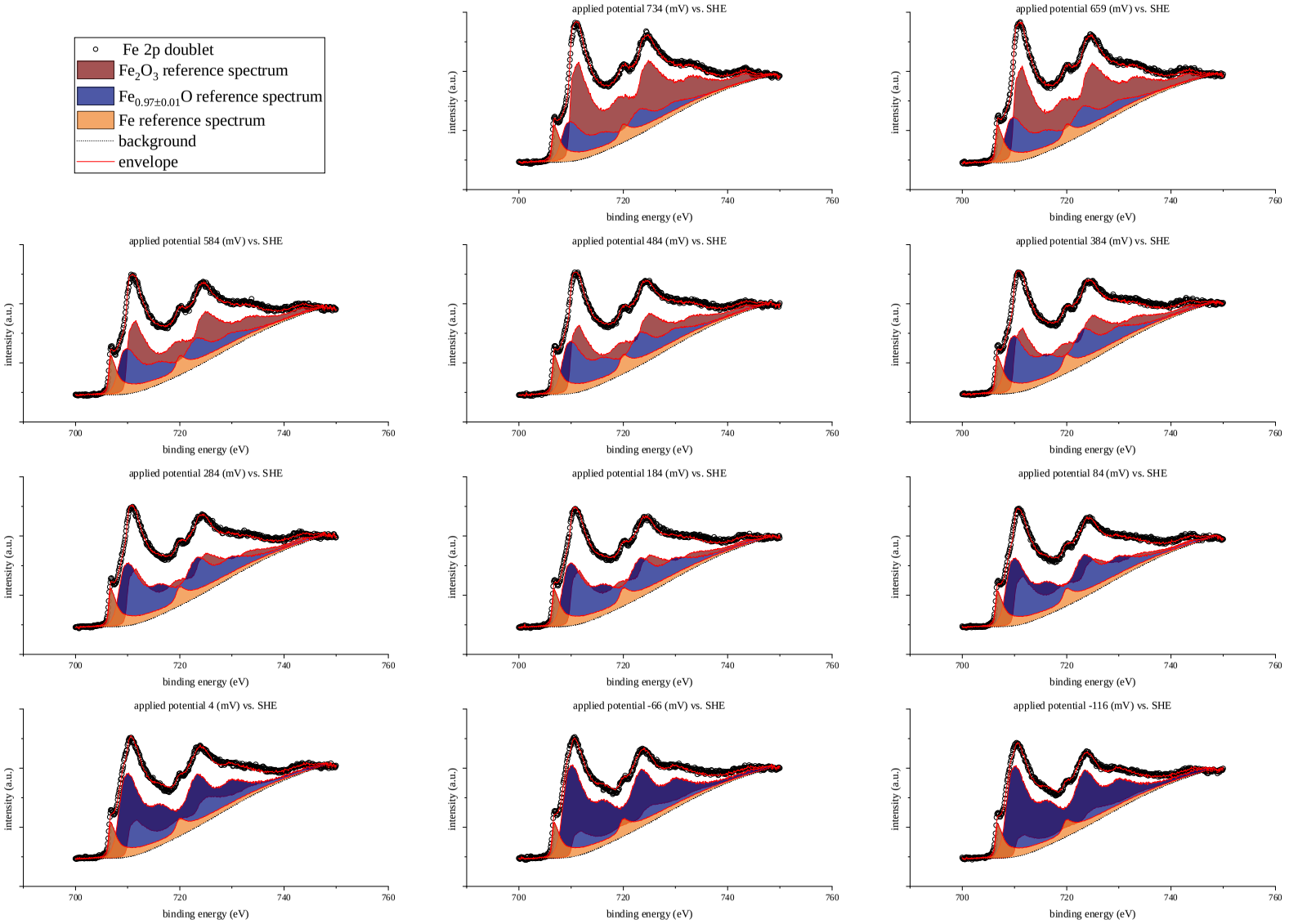

Figure 5.6: APXPS spectra of the $Fe\ 2p$ doublet in UHV during polarization. Fitting is performed with the reference spectra shown in Fig. 5.1. The measured spectra are linear combinations of the reference spectra.

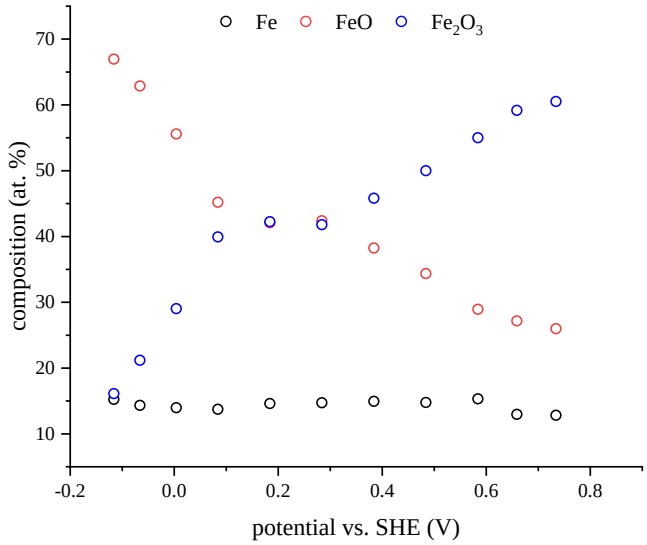

Figure 5.7: Quantification of the true electrode composition.

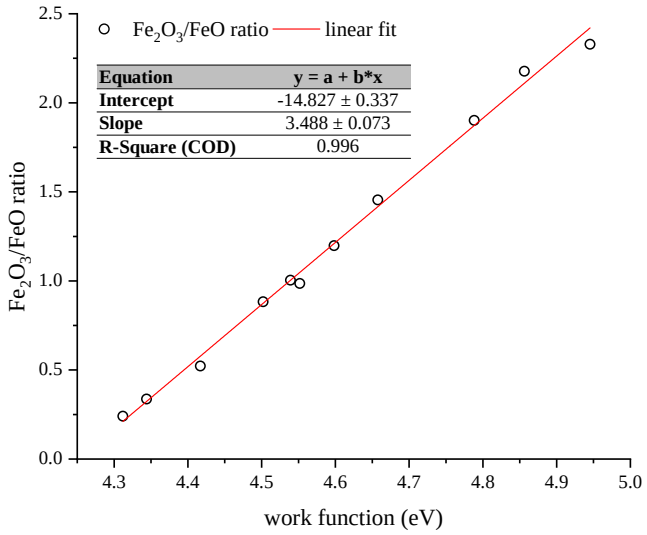

Figure 5.8: Work function and the true electrode composition correlation.

Chapter 6

Discussion

6.1 The Hydrogen Electrode on Palladium

The modern understanding of kinetics on the hydrogen electrode was shaped by *Tafel* [122], *Erdey-Gruz* [123], *Volmer* [123], and *Frumkin* [124, 125]. Based on these pioneering works, the reaction mechanism of the hydrogen electrode was found to proceed on two different pathways; denoted as the *Volmer-Tafel* and the *Volmer-Heyrowsky* mechanism, where the overall reaction is:

$$H_2 \rightleftharpoons 2H_{aq}^{+} + 2e^{-} \tag{6.1}$$

Because hydrogen gas and protons are in equilibrium, the hydrogen electrode is also called the gas electrode. In cathodic direction of the *Volmer-Tafel* mechanism, Eq. 6.2, atomic hydrogen is formed on the electrode surface in the *Volmer* step and further recombines to molecular hydrogen gas in the *Tafel* step. Whereas the *Volmer* step is a pure electron transfer reaction, the Tafel step is a chemical reaction [8].

$$\begin{aligned} H_{aq}^{+} + e^{-} &\rightleftharpoons H_{ad}, \;\; \textit{Volmer step} \\ H_{ad} + H_{ad} &\rightleftharpoons H_2, \;\; \textit{Tafel step} \end{aligned} \tag{6.2}$$

For the majoritiy of electrodes a pure transfer reaction as the *Volmer-Heyrowsky* mechanism is found to proceed on electrodes [8]. In cathodic direction, the *Volmer-Heyrowsky* mechanism proceeds by *Volmer* step, followed by the *Heyrowsky* step where molecular hydrogen is formed from a proton and an ad-

sorbed hydrogen, Eq. 6.3.

$$\begin{aligned} H_{aq}^{+} + e^{-} &\rightleftharpoons H_{ad}, \;\; \textit{Volmer step} \\ H_{aq}^{+} + H_{ad} + e^{-} &\rightleftharpoons H_2, \;\; \textit{Heyrowsky step} \end{aligned} \tag{6.3}$$

The hydrogen electrode on palladium, shows significant hydrogen absorption. Therefore, the electrode mechanism of the palladium hydrogen electrode includes an additional absorption step, Eq. 6.4 e.g. [126, 81].

$$H_{aq}^{+} + e^{-} \rightleftharpoons H_{ad} \rightleftharpoons H_{ab} \; \textit{absorption reaction} \tag{6.4}$$

In equilibrium, the *Nernst* equation can be applied. Hence, the electrode potential of the palladium hydrogen electrode is given by Eq. 6.5 [127, 81, 77], depending logarithmically on the hydrogen activity of ad-/absorbed species.

$$\epsilon = \epsilon_0 + \frac{RT}{F} ln\left(\frac{a(H_{aq}^{+})}{a(H_{ad})}\right) = \epsilon^{*} + \frac{RT}{F} ln\left(\frac{a(H_{aq}^{+})}{a(H_{ab})}\right) \tag{6.5}$$

As will be discussed, one key factor in establishing a hydrogen electrode is the presence of an electrolyte layer. On the entry side (Pd exposed to bulk electrolyte), the situation is well defined by the hydrogen activity in the electrolyte and the PdH_X phase. *Nernstian* behavior is found here, see **Appendix B** Fig. B.1. On the exit side (Pd exposed to the XPS instrument), the conditions were varied from UHV up to 0.25 *mbar* water vapor.

In the following, the hydrogen electrode on palladium is discussed in a first scenario, where no electrolyte is present at the exit side and H_{aq}^{+} is vanishing (UHV), and in a second scenario, where H_{aq}^{+} is formed on the exit side as a result of water adsorption from the gas phase at 0.25 *mbar* water vapor.

6.1.1 Hydrogen Influence (No Water)

When the sputter-cleaned palladium surface (exit side) is exposed to UHV, a work function increase on the exit side was measured when the hydrogen

activity was raised, i.e. the applied potential was lowered on the entry side, Fig. 6.1. The same influence of hydrogen was found by classical UHV studies: dosing *Langmuirs* of H_2 onto palladium films/foils, the work function was found to increase about 0.183 eV, resulting in work function of 5.18 eV [97]. Similar results were obtained by studies of palladium thin-films on glass substrates, where an increase of ≈ 0.22 V was measured at an equilibrium pressure of 0.016 $mbar$ of H_2 [128]. On single crystals a maximum work function increase of 0.36 eV, 0.18 eV, and 0.23 eV was found on $Pd(110)$, $Pd(111)$, and the stepped $Pd(110/111)$ surface, respectively [101]. Typically, the work function depends on the area specific surface dipole moment d_S, the vacuum permittivity ε_0, and the elementary charge e, where Φ_0 is the work function of the clean surface and Φ_{ad} the work function due to adsorption, Eq. 6.6, e.g. [129, 130, 131].

$$\Phi_{ad} = \Phi_0 - \frac{e\ d_S}{\varepsilon_0} \tag{6.6}$$

For a specie adsorbing with a negative dipole moment, pointing from the vacuum towards the surface, and hence enforcing the *natural* surface dipole moment of a *jellium* surface, the work function is raised. A decrease in work function is obtained for a positive dipole moment. Throughout the literature, atomic hydrogen adsorption is accompanied with an increase of work function [97, 101, 132, 133, 134, 135, 128]. A net electron transfer from the palladium to the adsorbed hydrogen causes a negative surface dipole moment [136, 101]. Hence, a work function increase. Depending on the adsorption site and -height, the work function increase is strongly affected when the hydrogen is located at atop/bridge positions, and almost unaffected when located at hollow sites, at similar heights compared to the surrounding palladium atoms [135]. A complicating factor is that hydrogen can penetrate the surface. Hypothetically, positively charged hydrogen species [128] located

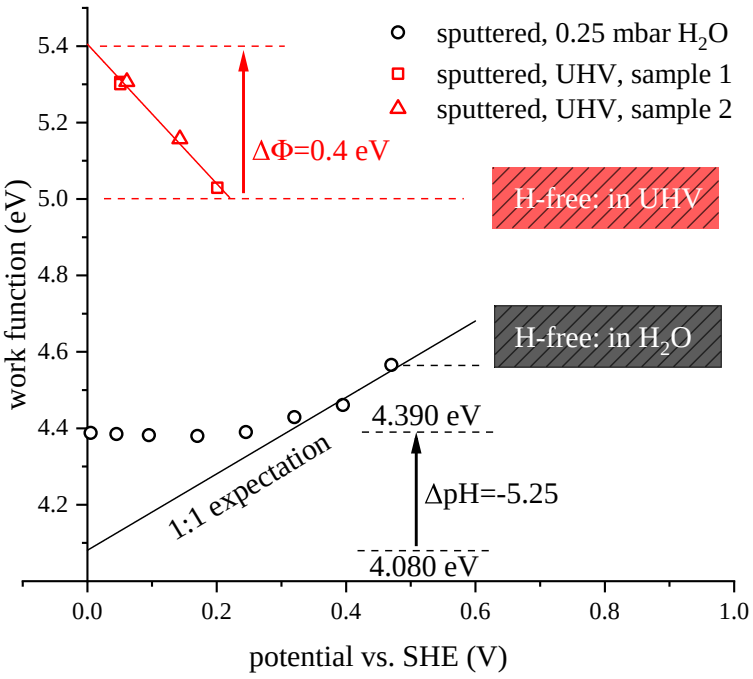

Figure 6.1: The hydrogen electrode on palladium.

in the subsurface [133, 137, 135] can also lead to a work function increase.

6.1.2 Hydrogen and Water Influence

In the situation where the sputter-cleaned palladium surface (exit side) is exposed to water vapor of 0.25 *mbar* while the hydrogen activity is controlled from the entry side, a complete different work function response is observed, see Fig. 6.1. Starting at a high potential, i.e. low hydrogen activity, and decreasing the potential results in a work function change: first, a decrease with an approximate $1:1$ response, second, the minimum work function at $\approx 0.2\ V$, third, ending with a slight increase.

Water adsorption is the crucial step in the formation of the hydrogen electrode. In classical electrochemistry, the electrode surface is burried under a thick layer of electrolyte, not accessible to XPS analysis. At 0.25 *mbar* water

vapor, the adsorbed water layer on the exit side corresponds to approximately one monolayer [82]. In principle XPS shows monolayer sensitivity. On palladium the $O\ 1s$ peak is at the same position as the $Pd\ 3p_{1/2}$, which makes it difficult to reveal its presence. With the help of the incremental difference spectra, Fig. 4.11, the $O\ 1s$ could be separated from the palladium background. The peak position of the clean $Pd\ 3p_{3/2}$ was measured as 532.2 eV, see **Appendix A** Fig. A.1, whereas the main peak in Fig. 4.11 is located at 532.6 eV, indicating a chemical shift. In comparison to the measured water gas phase, see **Appendix A** Fig. A.2, peak p_1 is attributed gaseous water. The exact position of p_1 depends on the sample work function [138]. Peak p_2 is attributed to adsorbed water species. A further distinction between different water-related species, as well as structure analysis, is hardly possible. From the APXPS study in [139], the $O\ 1s$ manifests a first broad peak ($\approx 536 - 532\ eV$) of liquid water and a second broad peak ($\approx 538 - 535\ eV$) of gaseous water.

Other APXPS investigations were done on water adsorption on metals. Despite it is known that water in the range of millibars cannot be dosed without carbon deposition, $O\ 1s$ spectra are frequently interpreted without showing any $C\ 1s$ spectrum. In this way a critical interpretation is excluded. For that reason, these investigations are not considered here. The source for carbon contamination ($CO_2,\ CO,\ -CH_x$) can be residual impurities in the water and carbon redeposition, originating from internal surfaces of the UHV system.

Clearly the carbon affects the $O\ 1s$ peak. For that reason, Fig. 4.8 compares the non-sputtered sample in UHV with the sputtered sample in 0.25 $mbar$ water vapor. In this way, the carbon related contribution to the $O\ 1s$ is

minimized. Anyway, the observed work function response is totally different and clearly attributed to water adsorption.

The process of water adsorption, structure studies of adsorbed water, and possible water dissociation is complex, such that frequently simulations are required. Some concepts are given in [33] to which the following refers. Adsorbed water molecules form covalent bonds with the metal substrate. Water molecules act as a *Lewis* base and provide the electron. The metal acts as a *Lewis* acid and receives the electron. Since the bond energy of water molecules with the metal[1] is close to the energy of the hydrogen bond[2], hexagonal water structures are formed, e.g. on $Pd(111)$ at 100 K [140]. In such structures, water molecules remain intact, where the majority of molecules is oriented parallel to the surface [140]. Conventionally, structure studies are performed at extremely low temperatures and might not be suitable for the present situation. In some cases, adsorbed water can partially dissociate, i.e. form hydroxyl radicals and protons, or even completely dissociate into oxygen radicals in addition. Including an interaction with the substrate, also ad-/absorbed species can form, i.e. potentially being important for hydrogen uptake by palladium samples. In all cases, the surface dipole moment is modified. Thus, affecting the work function.

When water adsorption is considered independently and dissociation products are excluded, simplistic electronegativity considerations suggest water adsorption to occur in a way that the molecular dipole moment points towards the vacuum. Indeed, such a behavior is not observed in general. With the interfacial excess on palladium[3] to $\Lambda = 9.8E^{18}\ m^{-2}$ [82], the work func-

[1] $0.4 - 0.7\ eV$ [33].
[2] $0.2 - 0.4\ eV$ [33].
[3] Corresponds to one monolayer.

tion of palladium without adsorption to $\Phi_0 = 5.0\ eV$, and the work function of palladium with water adsorption to $\Phi_{ad} = 4.6\ eV$, see chapter 6.1.1, an estimate for the water structure on palladium can be made using Eq. 6.7.

$$\Phi_{ad} = \Phi_0 - \frac{\Lambda d}{\varepsilon_0} \tag{6.7}$$

As a reference, the dipole moment of gaseous water molecules is considered to be $d^* \approx 6.18E^{-30}\ Cm$ [33]. With this approach, the dipole moment of one monolyer water on palladium is 0.06 d^*. Thus, giving the indication for adsorbed water to be aligned almost parallel to the palladium surface. As a comparison, the dipole moment of adsorbed water on a $Ag(100)$ surface is estimated to 0.12 d^*, and interpreted as water aligned almost in parallel to the metal surface [33].

Including partial water dissociation ($H_2O \rightleftharpoons OH^- + H^+$), ad-/absorption, and recombination processes, a neutral pH of adsorbed water is not a necessary boundary condition rather than a neutral net charge of the (metal|water) interface. Even a complete water dissociation ($H_2O \rightleftharpoons O^{2-} + 2H^+$) should not be excluded: Peak p_2 of the palladium $Pd\ 3d_{5/2}$ spectra in Fig. 4.10, coincides with the expectable position of PdO_{ad} [89].

When the hydrogen activity is changed at the entry side, the electrode equilibrium on the exit side has to adapt. Adaption processes, i.e. the *Volmer-Tafel-* or *Volmer-Heyrowsky* mechanism but mainly $H_{ab} \rightarrow H_{ab} \rightarrow H^+ + e^-$, are initiated and lead to a new equilibrium accordingly to the *Nernst* equation, Eq. 6.4. It follows that an increase of H^+_{aq} activity raises the electrode potential, whereas an increase of H_{ad} or H_{ab} activity loweres the electrode potential. Depending on the excess of either of specie, the electrode potential is dominated in either direction with respect to the applied potential.

In comparison to KP measurements[4], Fig. 3.7, and XPS measurements on non-sputtered samples, Fig. 4.8, a 1 : 1 relation between the applied potential on the entry side and the work function on the exit side is expected. From previous work [81], such a behavior is found for potentials between 0 and 400 mV vs. SHE. Referring to the sputtered sample in 0.25 $mbar$ water vapor, Fig. 6.1, the deviation of the expected 1 : 1 relation is proposed to be explained with an increased H^+_{aq} activity. Thus, understood as an acidification of the adsorbed water layer. Since the palladium electrode behaves as a pH electrode with a slope of 59 $mV/decade$ (e.g. **Appendix B** Fig. B.1), an acidification by $\Delta pH = -5.25$ can be calculated, see Fig. 6.1. A 1 : 1 relation is expected only for a pH-stabilized surface.

6.2 Catalytic Hydrogenation

In order to obtain a stabilized surface pH, an auxiliary equilibrium reaction is required. Species that may be part of such a reaction are CO_2 and CO. As mentioned previously, any UHV system contains residual gases that can provide these species. Based on [141, 142], the solvation of CO_2, deprotonation, and protonation proceeds by the mechanism shown in Eq. 6.8a - 6.8a, where k_i is the equilibrium constant[5].

$$CO_2 + H_2O \rightleftharpoons H_2CO_3,\ k_1 = \frac{[H_2CO_3]}{[CO_2]} \tag{6.8a}$$

$$H_2CO_3 \rightleftharpoons H^+ + HCO_3^-,\ k_2 = \frac{[H^+][HCO_3^-]}{[H_2CO_3]} \tag{6.8b}$$

$$CO_2 + H_2O \rightleftharpoons H^+ + HCO_3^-,\ k_2^* = \frac{[H^+][HCO_3^-]}{[CO_2]} \tag{6.8c}$$

$$HCO_3^- \rightleftharpoons H^+ + CO_3^{2-},\ k_3 = \frac{[H^+][CO_3^{2-}]}{[HCO_3^-]} \tag{6.8d}$$

[4] 1 atm of *"dry"* nitrogen with the r.h. < 0.1 % corresponds to < 0.23 $mbar$ water vapor.
[5] For simplicity rather concentrations than activities are assumed.

Water at ambient condition, i.e. with a partial pressure of $1E^{-3}$ $mbar$ CO_2, has a pH of 5.68 [143]. Such a pH is important as a possible buffer point for the hydrogen electrode carrying an external contamination.

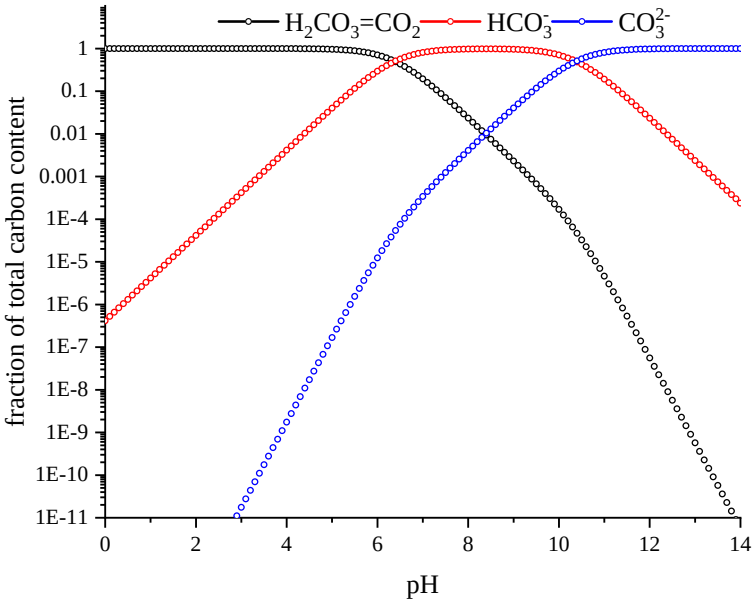

Figure 6.2: Acid base equilibrium of CO_2 and H_2O, calculated accordingly to [144], for a temperature of 293 K, with $k_2 = 4.17E^{-7}$ [145], $k_3 = 4.2E^{-11}$ [146, 144]. The total carbon amount is $[C] = [H_2CO_3] + [HCO_3^-] + [CO_3^{2-}]$.

Besides the chemical acid-base buffer of carbonic acid, a different mechanism involving the redox reaction of CO_2/CO that accepts H^+ also leads to a stabilized pH. Based on the thermodynamic data in [147], the standard potentials for CO_2 reduction can be estimated for the reactions given in Eq. 6.9a - 6.9f [148], adapted here to acidic conditions. Some of the standard potentials are located in a reasonable range of the applied potentials. Of course, this is true in the case where standard conditions apply to the palladium hydrogen electrode. Whether CO_2 reduction is feasible under the

restrictions of the APXPS is addressed in chapter 7. For instance, Eq. 6.9a - 6.9f are firstly interpreted to stabilize the surface pH and secondly to explain the variations in the $C\ 1s$ spectra, Fig. 4.4 - 4.7 and 4.9. Interestingly, the $C\ 1s$ spectra show significantly less variations when water vapor is added. As it is seen from the Eq. 6.9a - 6.9f, water is a product of the reduction process that shifts the equilibrium towards CO_2.

$$2CO_2 + 12H^+ + 12e^- \rightleftharpoons C_2H_4 + 4H_2O,\ \epsilon_0 = 0.08\ V\ vs.\ SHE \tag{6.9a}$$

$$CO_2 + 8H^+ + 8e^- \rightleftharpoons CH_4 + 2H_2O,\ \epsilon_0 = 0.17\ V\ vs.\ SHE \tag{6.9b}$$

$$CO_2 + 2H^+ + 2e^- \rightleftharpoons CO + H_2O,\ \epsilon_0 = -0.1\ V\ vs.\ SHE \tag{6.9c}$$

$$CO_2 + H^+ + 2e^- \rightleftharpoons HCOO^-,\ \epsilon_0 = 0.001\ V\ vs.\ SHE \tag{6.9d}$$

$$2CO_2 + 12H^+ + 12e^- \rightleftharpoons C_2H_5OH + 3H_2O,\ \epsilon_0 = 0.09\ V\ vs.\ SHE \tag{6.9e}$$

$$2CO_2 + 18H^+ + 2e^- \rightleftharpoons C_3H_7OH + 5H_2O,\ \epsilon_0 = 0.1\ V\ vs.\ SHE \tag{6.9f}$$

Palladium is known as a catalyst to dehydrate formic acid, methanol, and acetic acid [149, 150, 151, 152, 153]. E.g., methanol decomposition is found to proceed on $Pd(111)$ in the steps of Eq. 6.10, giving various decomposition intermediates [150].

$$CH_3O_{ad} \rightarrow CH_2O_{ad} + H_{ad} \rightarrow CHO_{ad} + 2H_{ad} \rightarrow CO_{ad} + 2H_{ad} \tag{6.10}$$

Based on CO_2, the reverse reaction is given in Eq. 6.11 [154].

$$CO_2 + 6H^+ + e^- \rightleftharpoons CH_3OH + H_2O,\ \epsilon_0 = 0.02\ V\ vs.\ SHE \tag{6.11}$$

Taking the peak positions and -shifts of the measured $C\ 1s$ spectra, a comparison with the *NIST* database [155] leads to the assignments shown in Tab. 6.1. Due to the high number of different carbon species, a precise peak assignment cannot be done for the $C\ 1s$ spectra. Anyway, various hydrogenation products in response to an applied potential can be found.

Table 6.1: Possible C 1s assignment according to *NIST* database [155]. Abbreviations: Peak label (Lbl.), binding energy (B.E.), identification (Id.), on a: UHV, sputtered, internal carbon; b: UHV, non-sputtered external carbon; c: water, non-sputtered external carbon; d: water, sputtered, internal carbon, Reference (Ref.). See C 1s spectra in Fig. 4.4 - 4.9.

Lbl.	**B.E.** (eV)	**Id.**	***NIST* Assignment [155]**	**Ref.**
p_1	$284.8 - 284.6$	a, b, d	284.7 eV CH_3OH on $Pd(111)$ 105 K	[156]
		a, b, d	284.6 eV CH_3I on $Pd(100)$ 200 K	[157]
p_2	285.9	a	285.8 eV CH_3OH on $Pd(111)$ 110 K	[158]
			286.0 eV CO_2^- Fe polycrystalline	[159]
p_3	$284 - 283.8$	a, b	283.9 eV C_2H_2 on $Pd(111)$ $99 - 350$ K	[160]
p_4	286.8	a	286.8 eV CH_3OH $Pd(100)$ 90 K	[161]
			286.4 eV CO_2^- $Ni(110)$ 150 K	[159]
p_5	≈289	b, c	289 eV $HCOOH$ $MgO(100)$ 293 K	[162]
			290.1 eV $CaCO_3$	[163]
p_6	≈ 288	b, c, d	287.9 eV CH_3OH $Pd(100)$ 90 K	[161]
		c, b, d	287.7 eV $HCHO$	[164]
p_7	285.1	b, c, d	various species C, CH_x	
p_8	289.3	b	289.3 eV CH_3COOH	[164]
p_9	≈ 285.7	b	285.8 eV CO on $Pd(110)$ 150 K	[165]

6.3 The Hydrogen Electrode on Iron Oxides

Stoichiometric magnetite (Fe_3O_4) exists in the inverse spinel structure [166] with the chemical composition of $Fe^{2+}Fe_2^{3+}O_4^{2-}$. It was found by *Mösbauer*

spectroscopy that non-stoichiometric magnetite has an identical crystallographic structure than stoichiometric magnetite. The cation occupation of interstitial sites within the oxygen unit cell[6] varying for non-stoichiometric magnetite [167]. While the Fe^{2+} cations occupy octahedral (oct) sites only, Fe^{3+} cations also occupy tetrahedral (tet) sites. The general magnetite composition can be written as $(Fe^{3+})_{tet}(Fe^{3+}_{1+2\lambda}Fe^{2+}_{1-3\lambda}\circ_{\lambda})_{oct}O_4^{2-}$, where $\circ$ is a vacancy and λ the vacancy parameter ranging from 0 to 1/3 [168]. For that reason, magnetite can be represented by mixing Fe^{3+} and Fe^{2+}, for instance with hematite Fe_2O_3 and wüstite ($Fe_{1-x}O,\ x = 0$) in its stoichiometric form as $(FeO)_1(Fe_2O_3)_1$ [167]. Apparantly, this was directly observed in Fig. 5.6 for the hydrogen electrode on iron oxides: Any magnetite spectrum is a linear combination of Fe, $Fe_{0.97\pm0.01}O$ and Fe_2O_3, precisely reconstructing the complex line shape over the full range of the $Fe\ 2p$ doublet. Thus, the XPS data provide accurate information about the chemical composition at different potentials. A true quantification is obtained when the $Fe_{0.97\pm0.01}O$ phase is corrected for its non-stoichiometric composition, see chapter 5. Concerning the hydrogen electrode on iron oxides, magnetite represents a redox couple of Fe^{2+}/Fe^{3+} to which a standard potential is assigned, e.g. [169, 170], depending on phase and stoichiometry.

Considering the different magnetite equilibria, an upper and a lower limiting case can be found with respect to the *Pourbaix* diagram for solid substances [169]: The upper limit is given by Eq. 6.12 [169].

$$3Fe_2O_3 + 2H^+ + 2e^- \rightleftharpoons 2Fe_3O_4 + H_2O,\ \epsilon_0 = 0.221\ V\ vs.\ SHE \quad (6.12)$$

[6] *"The unit cell consists of a cage of* 32 O^{2-} *ions in a face centred cubic arrangement"* [167].

The lower limit is given in its anhydrous and hydrous[7] state by Eq. 6.13 [169].

$$\begin{aligned} &Fe_3O_4 + 2H^+ + 2e^- \rightleftharpoons 3FeO + H_2O,\ \epsilon_0 = -0.197\ V\ vs.\ SHE \\ &hydrous, \qquad\qquad\qquad\qquad\qquad\quad \epsilon_0 = 1.208\ V\ vs.\ SHE \end{aligned} \tag{6.13}$$

Under standard conditions the activities of all involved substances are equal to unity. Here, the standard state of magnetite is taken as the stoichiometric magnetite, involving an equal activity for both FeO and Fe_2O_3. Replacing Fe_3O_4 (from Eq. 6.12 and 6.13) by $(FeO)_1(Fe_2O_3)_1$ yields in both cases Eq. 6.14. The corresponding standard potential, for its anhydrous and hydrous[8] state, can be found in [169].

$$\begin{aligned} &Fe_2O_3 + 2H^+ + 2e^- \rightleftharpoons 2FeO + H_2O,\ \epsilon_0 = -0.057\ V\ vs.\ SHE \\ &Fe(OH)_3 + H^+ + e^- \rightleftharpoons Fe(OH)_2 + H_2O,\ \epsilon_0 = 0.271\ V\ vs.\ SHE \end{aligned} \tag{6.14}$$

Eq. 6.14 is interpreted as the equilibrium between Fe_2O_3/FeO or $Fe(OH)_3/Fe(OH)_2$ within the inverse spinel structure of magnetite. The associated standard potential is obtained for stoichiometric composition while all other involved substances are under standard conditions. However, the electrode potential of non-stoichiometric magnetite is a function of its current composition. Therefore, the electrode potential (hydrous) is obtained by Eq. 6.15, where the index s refers to stoichiometric magnetite composition. Regarding the adsorption of water, it is assumed that the outer surface of the iron oxides are hydrated. For that reason Eq. 6.15 is considered for hydrous magnetite.

$$\epsilon = 0.271 + 0.059\ \log\left(\frac{[Fe(OH)_3/(Fe(OH)_3)_s]H^+}{[Fe(OH)_2/Fe(OH)_2)_s]H_2O}\right) \tag{6.15}$$

On basis of the above treatment, Fig. 6.3 can be divided into three parts: *Part I* is characterized by magnetite with an inverse spinel structure at high

[7]No equilibrium reaction is given in [169], see ibid.
[8]No equilibrium reaction is given in [169], see ibid.

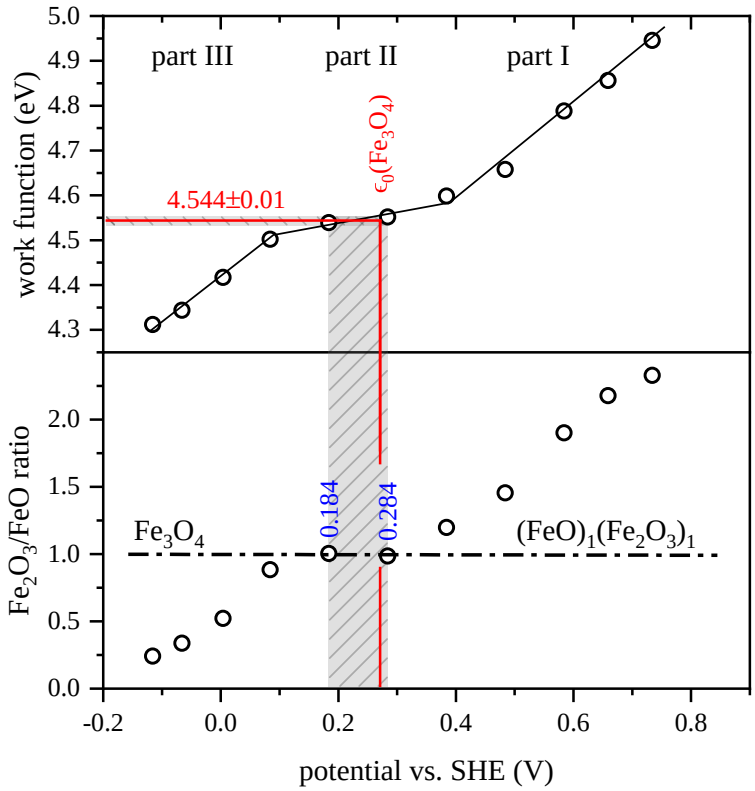

Figure 6.3: The work function (exit side) and its correlation to applied potentials (entry side) and chemical electrode composition (exit side). Same data as shown in Fig. 5.5.

fractions of Fe^{3+} states. An increase of H activity (i.e. a lower potential at the entry side) evokes a degradation of Fe^{3+}_{oct} states and vacancies while the Fe^{2+}_{oct} states are raised. The ratio Fe^{3+}/Fe^{2+} is given by $(2+2\lambda)/(1-3\lambda)$, therefore depending on λ, i.e. vacancies. At stoichiometric magnetite composition, the electrode potential of the iron electrode depends only on the H^+/H_2O ratio, compare Eq. 6.15, that includes zero vacancies since $\lambda = 0$. In *part II*, a further formation of Fe^{2+} states is obstructed since λ cannot attain negative values. For that reason, it is assumed here that the iron electrode cannot follow the hydrogen electrode in the way that e^- and H^+, assisted by the hydrogen electrode ($H \rightleftharpoons H^+ + e^-$), are used to reduce Fe^{3+} states. For instance, it is not clear whether the formation of H^+ is hindered while the potential on the exit side is lowered. The plateau in *part II* can be understood as a potential "*increase*", realized either by an increase of H^+ activity, by a different standard potential (i.e. reaction), or even by a decrease of H_2O activity. In the situation where the H^+ consumption is hindered, H^+ may be assumed to exist with an increased activity. On the one hand the electrode potential of the hydrogen electrode is lowered, on the other hand a new standard potential may be the result of crystallographic reorganization. In this process, presumedly H plays a crucial role through the incorporation of two H into tetraethal sites (four ligands). As the result, tetraethal sites turn into octahetral sites (six ligands). However, *part II* is interpreted as the decomposition of the inverse spinel structure and turning into a structure that allows the formation of further Fe^{2+} states. Such a structure might be comparable with a defective wüstite rock salt structure, which is characterized by different ratios of tetrahedral to octahedral sites, see [171]. At the transition from *part II* to *-III*, a new standard potential (i.e. reaction) allows the iron electrode to follow the hydrogen electrode again. So

far this is how the hydrogen electrode on iron oxides is interpreted here.

The observation of wide 1 : 1 relations, between the applied potential and the measured work function, can be understood as a stabilized surface pH. According to Eq. 6.12 - 6.14, the iron oxide reduction is related to the consumption of H^+ and the formation of H_2O that might stabilize the surface pH. Anyhow, the mechanism is likely to be more complicated, as it can be seen e.g. on the linear correlation of work function and ratio Fe_2O_3/FeO, Fig. 5.8, that is recently not understood. Based on the *Nernst* equation a logarithmic relationship is expected instead.

6.4 The Absolute Electrode Potential

As it was elucidated in chapter 3.2.2, the photoelectric work function is the absolute electrode potential referring to the position *just outside* the sample. For that reason, the photoelectric work function is equivalent to the absolute electrode potential ϵ^3_{abs}/e. According to the current state of literature, a direct measurement of the absolute electrode potential of the SHE ($\epsilon_{abs}(SHE)$) is not reported. In order to identify $\epsilon_{abs}(SHE)$ from the measured ϵ_{abs} and the applied potentials of the *thin film electrode*, three sources of error need to be considered:

1. Equilibrium or dynamic steady state condition?

2. What is the surface pH?

3. What is the dipole contribution?

In equilibrium, both sides have the same hydrogen activity but not necessarily the same surface pH. I.e. the potentials might be different. In steady state conditions with significant less hydrogen activity at the exit side, a linear

gradient in electrochemical potential across the entry and exit side causes an offset between the hydrogen activity at the entry- and exit side. Fast diffusion and thin membranes reduce the diffusion gradient. Thus, limit the size of the error. Hydrogen diffusion in palladium is fast: In the α-phase the diffusion coefficient at room temperature is $1.3E^{-7}$ cm^2/s [172] that gives a time lag[9] of only ≈ 80 s for a 80 μm thick membrane. The main obstruction to establish equilibrium is hydrogen recombination and desorption into the UHV. According to the *Polanyi-Wigner* equation [173], the desorption rate increases exponentially with the hydrogen coverage. If the equilibrium is affected by desorption, the work function trend is expected to converge at some point. I.e. it should bend downward on elevated hydrogen activities when compared to lower activities. Obviously, this is not observed under the most severe condition: for sputtered samples in UHV, Fig. 4.1. Here, hydrogen recombination is most likely to occur due to the high number of available sites for hydrogen ad-/desorption. The situation is different when the surface condition is changed. E.g. by an adsorbed layer that decrease the hydrogen permeation rate [174], also known as palladium poisoning and deactivation occuring by carbon monoxide [175, 176] or hydrocarbons [174]. Considering the case of a sputtered sample with an adsorbed water layer, Fig. 4.1, the work function deviation from the expected behavior can be interpreted as hydrogen desorption. However, as it was discussed earlier, the deviation can also be associated with a pH change.

Assuming equilibrium with an identical surface pH on both sides of the membrane, $\epsilon_{abs}(SHE)$ is obtained from the intersection. Under the same conditions but with a difference in the surface pH, the knowledge about the surface pH on the exit side is required with regard to the $\epsilon_{abs}(SHE)$.

[9] $t_{lag} = \Delta r^2/6D$, where Δr is the membrane thickness and D the diffusion coefficient [172].

The electrical double layer and the solution surface determine the absolute electrode potential [43]. For that reason, the condition for the immersed- (e.g. SHE), emersed electrode [35, 42, 37, 43], and the *thin film electrode* are different. It is also clear that different emersion techniques, such as emersion into UHV with virtually no water and emersion into a water-saturated atmosphere, influence the double layer structure [43]. The electrode potential for emersed electrodes into a water-saturated atmosphere was found to be below the value of immersed electrodes, which is understood as the top water layer largely orientated with its dipole moment pointing towards the vacuum[10] [43, 177]. Such a behavior is not found for all metals. As it was reported in [33, 140], the dipole moment of adsorbed water molecules is aligned almost parallel to the metal surface. The same tendency was found in this work for water adsorption on palladium, see chapter 6.1.2. However, when specific ions are present, a tendency for weakly adsorbed ions is observed, irrespective of its anion or cation nature. A large influence was found in the sequence of $SO_4^{2-} > Cl^- > I^-$ and $Cs^+ > K^+ > Na^+ > Li^+ > H^+$ that has the effect in decreasing the electrode potential upon emersion [43]. Quantitatively, the strongest effect is found by emersion from electrolyte solutions of H_2SO_4 with a potential change of $-0.32\ V$, and the smallest influence is observed for electrolyte solutions of NaI with $-0.07\ V$ [43].

The *thin film electrode* is not an emersed electrode. The double layer which is formed *in situ/operando* is void of dissolved ions other than H^+. For this reason, only a minor influence can be expected according to [43]. When water is bonded chemically, e.g. the hydrogen electrode of hydrous iron oxides, the dipole influence is expected to have an even lower influence. Anyhow, a direct comparison to an immersed electrode (SHE) can include some uncertainty.

[10] With the (negative) oxygen towards the metal [43, 177].

The surface pH of the hydrogen electrode on palladium is unknown. Based on the double layer capacitance, the following estimation can be made: At $pH = 0$, one monolayer of water can be assumed to have 1/55 of $9.8E^{18}$ H^+-molecules per m^2, compare [82]. The standard potential of palladium is 915 mV [178]. Palladium can be considered as hydrogen-free at a potential of 550 mV vs. SHE or higher. At 0 mV vs. SHE, the double layer capacity C_d in the order of 20 to 50 $\mu F/cm^2$, and the elementary charge e to $1.6E^{-9}$ C, the surface pH is calculated to exist in the range from -0.6 to -1.0, see Eq. 6.16.

$$pH = -log\left(\frac{0.550 \cdot C_d}{1.6E^{-19} \cdot 1/55 \cdot 9.8E^{18}}\right) \approx -0.6\ to\ -1.0 \tag{6.16}$$

The work function of the hydrogen electrode on palladium is 4.39 eV when polarized to 0 mV vs. SHE, Fig. 6.1. With the estimate in Eq. 6.16, the pH-corrected value is: $\epsilon_{abs}(SHE) = 4.343\ eV$. Note that the dipole contribution is not considered.

Concerning the hydrogen electrode on iron oxides at stoichiometric magnetite composition, a reference point is suggested to be found that correlates chemical states, work function, and applied potentials with the standard electrode potential of the $Fe(OH)_3/Fe(OH)_2$ equilibrium, Eq. 6.14. The standard potential deviates only about $\approx 10\ mV$ from the applied potential (entry side). Assuming that the applied potential is identical to the potential on the exit side, the absolute electrode potential of the SHE is obtained by subtracting the standard potential (0.271 V vs. SHE) from the work function (4.554 eV), Fig. 6.3, giving: $\epsilon_{abs}(SHE) = 4.283\ eV$. Also here, the dipole contribution is not considered.

The *IUPAC* recommended value for the absolute electrode potential of the SHE, emerged from *Transatti's* work, is $4.44 \pm 0.025\ eV$. When compared

to other works, reported values show a span of 0.42 eV, see Tab. 2.1. Under certain assumptions, the values obtained in this work are lower than usually reported. Nevertheless, they represent a direct determination of the absolute electrode potential under *in situ/operando* conditions.

Chapter 7

Summary and Outlook

This work comprises the development and introduction of a completely new transferable electrochemical set-up, denoted as the *thin film electrode*. For the first time the opportunity is given to investigate the (electrode|liquid|gas) interface with monolayer-sensitivity by analytical methods which conventionally operate under UHV conditions only.

In a first step, a miniaturized reference electrode was developed, with so far unprecedented long-time stability and precision, that enables a reliable and secure use together with the *thin film electrode*, even under UHV conditions. In a second step, the *thin film electrode* was developed. In a third step, the *thin film electrode* was used in an APXPS instrument that gave the opportunity to perform photoemission spectroscopy at ambient pressure. Novel experimental results were obtained from hydrogen electrodes. It was shown that chemical analysis and absolute electrode potentials in dependency of applied electrochemical potentials are correlated. In particular, the concept of the absolute electrode potential was elucidated and directly applied via photoelectric work function measurements. The *IUPAC* recommended value for the absolute electrode potential of the SHE is $4.44 \pm 0.025\ eV$. The values reported in literature show a span of $0.42\ eV$. So far, no direct determination was possible and the overall error is influenced by error propagation due to the indirect determination steps. In this work, absolute electrode potentials are directly measured and similar values (4.39 and $4.42 \pm 0.005\ eV$) are obtained for applied entry potentials at $0\ V$ vs. SHE. It is thought that these

values are compromised by surface acidification. Thus, require a pH correction for standard conditions. For the hydrogen electrode on iron oxides, a reference point was found by means of photoemission spectroscopy, which allowed to correlate chemical states, work function, and applied potentials with a reported standard electrode potential. Under certain assumptions, the absolute electrode potential of the SHE is obtained to 4.283 eV.

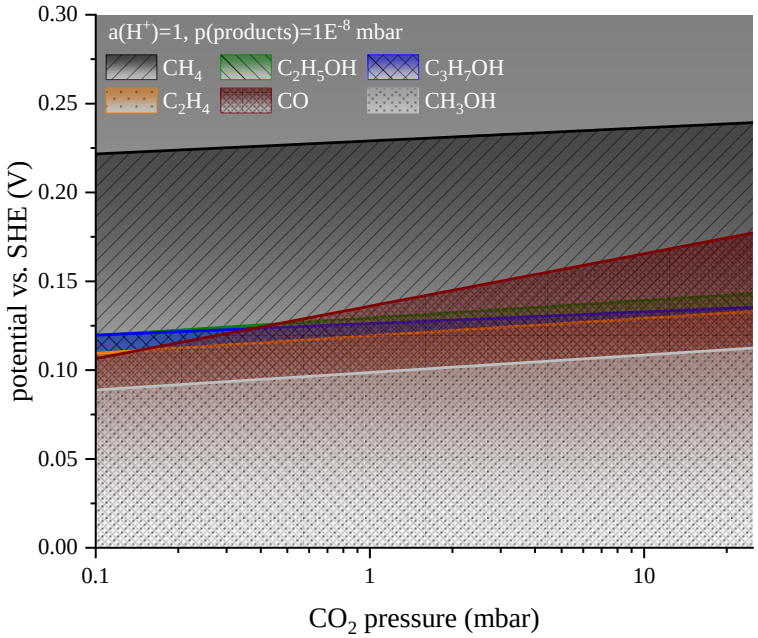

Figure 7.1: Equilibrium potentials for CO_2 reduction in APXPS ($HCOO^-$ is above the CH_4 potential).

The concept of the *thin film electrode* can be extended to other materials, reactions, and analysis methods. It was found that alterations in the C $1s$ spectra in response to applied potentials are unambiguously the effect of electrochemical-/catalytic hydrogenation. This observation can be related to CO_2/CO reduction. Based on the standard potentials for CO_2 reduction, Fig. 7.1 shows the feasibility for CO_2 reduction in future APXPS studies.

Besides the concept of the *thin film electrode*, a completely different electrochemical set-up can be realized when a *window sample* is used. In future, such a set-up can be used to investigate the (electrode|double layer|bulk electrolyte) interface. Thus, tackling the transition from a thin film towards a bulk electrolyte.

Appendix A

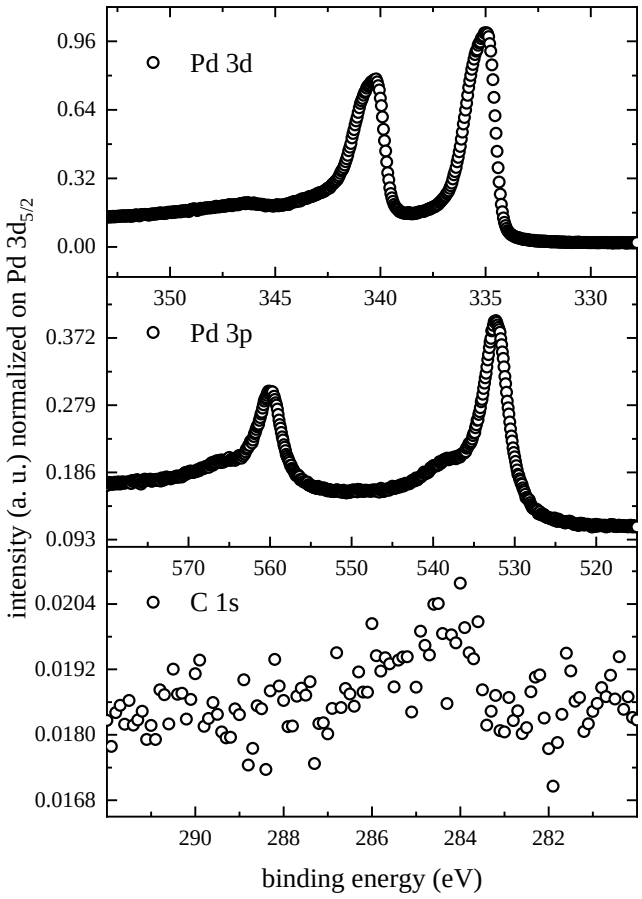

Figure A.1: XPS spectra of *clean* palladium at room temperature in UHV ($4E^{-10}$ $mbar$). Monochromated Al $K\alpha$ source. Binding energy referenced on the *Fermi edge* of Ag. Nominal palladium purity is 99.95 %. Iterative preparation: Annealing at 973 K for 10 min, followed by Ar-sputtering at room temperature (last step annealing). Spectra are measured in the order of Pd $3d$, Pd $3p$, C $1s$.

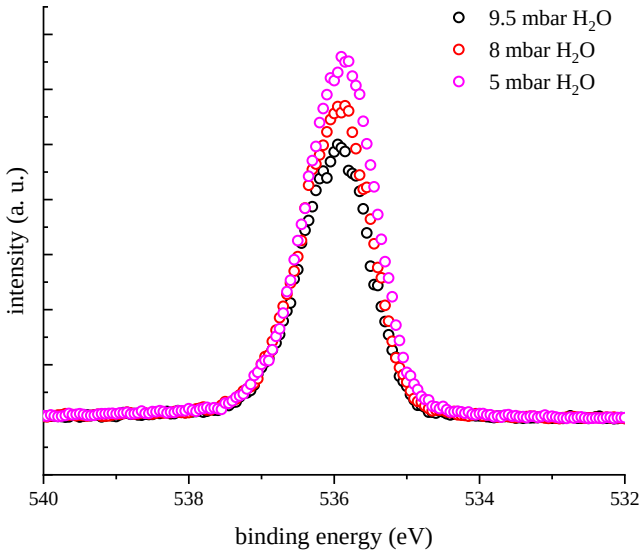

Figure A.2: XPS spectra of water vapor at room temperature. Monochromated *Al* $K\alpha$ source. Preparation: Ultrapure water, degassed with the freeze-pump-thaw technique.

Appendix B

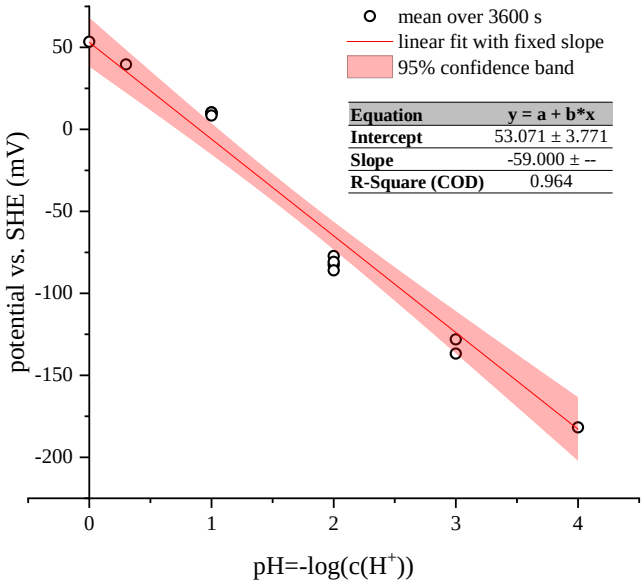

Figure B.1: pH response of the PdH_X electrode at $X = \alpha + \beta$, the onset of the $\alpha + \beta$-phase. The potential width of the $\alpha + \beta$-phase is $\approx 10\ mV$.

Appendix C

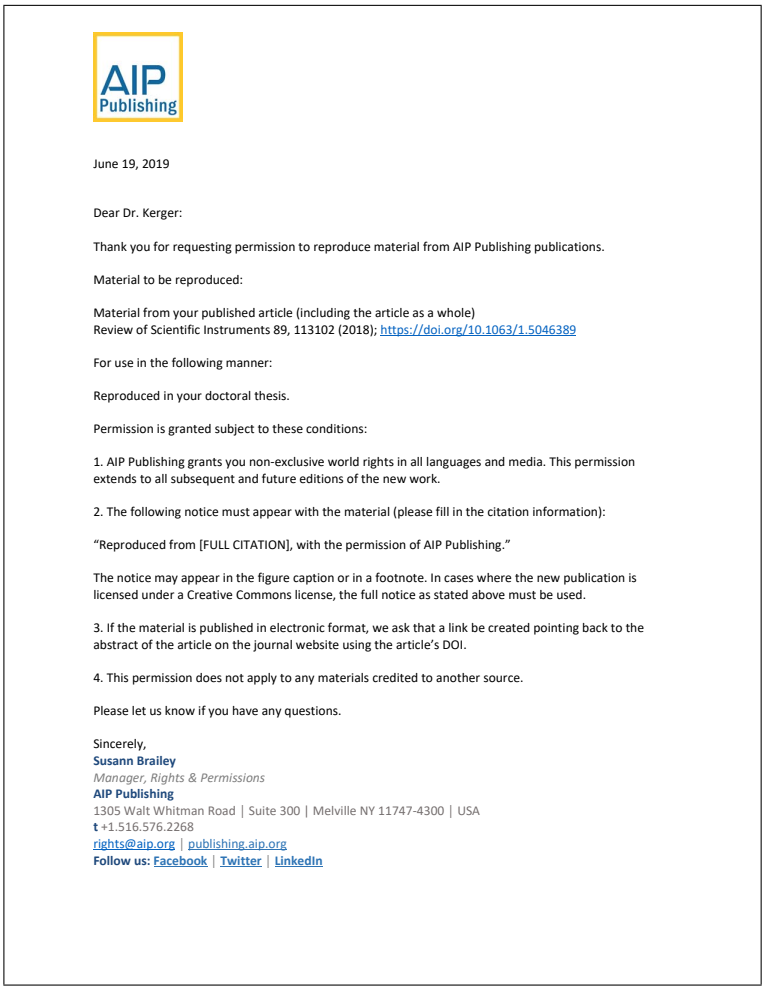

June 19, 2019

Dear Dr. Kerger:

Thank you for requesting permission to reproduce material from AIP Publishing publications.

Material to be reproduced:

Material from your published article (including the article as a whole)
Review of Scientific Instruments 89, 113102 (2018); https://doi.org/10.1063/1.5046389

For use in the following manner:

Reproduced in your doctoral thesis.

Permission is granted subject to these conditions:

1. AIP Publishing grants you non-exclusive world rights in all languages and media. This permission extends to all subsequent and future editions of the new work.

2. The following notice must appear with the material (please fill in the citation information):

"Reproduced from [FULL CITATION], with the permission of AIP Publishing."

The notice may appear in the figure caption or in a footnote. In cases where the new publication is licensed under a Creative Commons license, the full notice as stated above must be used.

3. If the material is published in electronic format, we ask that a link be created pointing back to the abstract of the article on the journal website using the article's DOI.

4. This permission does not apply to any materials credited to another source.

Please let us know if you have any questions.

Sincerely,
Susann Brailey
Manager, Rights & Permissions
AIP Publishing
1305 Walt Whitman Road | Suite 300 | Melville NY 11747-4300 | USA
t +1.516.576.2268
rights@aip.org | publishing.aip.org
Follow us: Facebook | Twitter | LinkedIn

Figure C.1: Copyright permission from AIP Publishing

Bibliography

[1] P.W. Atkins. *Physical chemistry.* Oxford University Press Oxford, 1978.

[2] D. Baehr. *Thermodynamik Grundlagen und technische Anwendungen.* Springer Berlin Heidelberg, Berlin, Heidelberg, 2005.

[3] C.H. Hamann and W. Vielstich. *Elektrochemie.* Wiley-VCH, 2005.

[4] C. Weißmantel and C. Hamann. Springer: Berlin, Heidelberg, New York, 1980.

[5] W. Schottky and H. Rothe. *Physik der Glühelektroden.* Number 13, 2 in Handbuch der Experimentalphysik. 1928.

[6] E. Lange and K.P. Mischenko. Z. Phys. Chem. 1930.

[7] E. Lange. Über elektrochemische Grundbegriffe, insbesondere der Elektrode Metall/Lösung. *Zeitschrift für Elektrochemie und angewandte physikalische Chemie*, 55(2):76–92, 1 1951.

[8] K.J. Vetter. Springer Berlin Heidelberg, 1961.

[9] W. Schottky. *Phys. Z.*, (15):872, 1914.

[10] R. Parsons. *Modern Aspects of Electrochemistry*, volume 1. Ed., J. O'M. Bockris, Butterworths, London, 1954.

[11] S. Trasatti. The "absolute" electrode potential—the end of the story. *Electrochimica Acta*, 35(1):269 – 271, 1990.

[12] E.A. Kanevsky. *Zh. Fiz. Khim*, 22:1397, 1948.

[13] E.A. Kanevsky. It is possible to develop the thermodynamic theory of electrode potential. *Zh. Fiz. Khim*, 24:1511–1514, 1950.

[14] E.A. Kanevsky. *Zh. Fiz. Khim*, 27:296, 1953.

[15] A.J. Bard, R. Parsons, and J. Jordan. Standard potentials in aqueous solution 1985. *M. Dekker*.

[16] J. O'M. Bockris and S.D. Argade. Work function of metals and the potential at which they have zero charge in contact with solutions. *The Journal of Chemical Physics*, 49(11):5133–5134, 1968.

[17] J. O'M. Bockris and S.U.M. Khan. Fermi levels in solution. *Applied Physics Letters*, 42(1):124–125, 1983.

[18] A.N. Frumkin and B.B. Damaskin. Real free-energy of electron solvation under conditions of equilibrium of electrode with solution. *Doklady Akademii Nauk SSSR*, 221(2):395–398, 1975.

[19] A. Frumkin and B. Damaskin. Real free solvation energy of an electron in a solution in equilibrium with the electrode and its dependence on the solvent nature. *Journal of Electroanalytical Chemistry and Interfacial Electrochemistry*, 79(2):259 – 266, 1977.

[20] R. Gomer and G. Tryson. An experimental determination of absolute half-cell emf's and single ion free energies of solvation. *The Journal of Chemical Physics*, 66(10):4413–4424, 1977.

[21] D.L. Rath and D.M. Kolb. Continuous work function monitoring for electrode emersion. *Surface Science*, 109(3):641 – 647, 1981.

[22] D.M. Kolb. UHV techniques in the study of electrode surfaces. *Zeitschrift für Physikalische Chemie*, 154(12):179–199, 1987.

[23] H. Gerischer and W. Ekardt. Fermi levels in electrolytes and the absolute scale of redox potentials. *Applied Physics Letters*, 43(4):393–395, 1983.

[24] H. Reiss and A. Heller. The absolute potential of the standard hydrogen electrode: a new estimate. *The Journal of Physical Chemistry*, 89(20):4207–4213, 1985.

[25] S. Trasatti. The absolute electrode potential: An explanatory note (recommendations 1986). *Pure and Applied Chemistry*, 58(7):955–966, 1986.

[26] S. Trasatti. Structure of the metal/electrolyte solution interface: new data for theory. *Electrochimica acta*, 36(11-12):1659–1667, 1991.

[27] W.N. Hansen and G.J. Hansen. Reference states for absolute half-cell potentials. *Phys. Rev. Lett.*, 59:1049–1052, 1987.

[28] E.A. Kanevsky. *Zh. Fiz. Khim*, 25:854, 1951.

[29] A. Frumkin. Remark on the paper of S. Trasatti: The concept of absolute electrode potential. An attempt at a calculation. *Journal of electroanalytical chemistry (1959)*, 66(2):150–154, 1975.

[30] S. Trasatti. *Advances in Electrochemistry and Engineering*, 10:213, 1976.

[31] H. Reiss. The absolute potential of the standard hydrogen electrode: a new estimate. *Journal of Physical Chemistry*, 89:4213, 1985.

[32] R. Parsons. *Standard Potentials in Aqueous Solution*. CRC Press, 1985.

[33] N. Sato. In *Electrochemistry at Metal and Semiconductor Electrodes*. Elsevier Science, Amsterdam, 1998.

[34] R. Gomer. *The Journal of Chemical Physics*, 66:4424, 1977.

[35] W.N. Hansen and D.M. Kolb. The work function of emersed electrodes. *Journal of Electroanalytical Chemistry and Interfacial Electrochemistry*, 100(1):493 – 500, 1979.

[36] W.N. Hansen and G.J. Hansen. Absolute half-cell potential: A simple direct measurement. *Phys. Rev. A.*, 36:1396–1402, 1987.

[37] E.R. Kötz, H. Neff, and K. Müller. A UPS, XPS and work function study of emersed silver, platinum and gold electrodes. *Journal of Electroanalytical Chemistry and Interfacial Electrochemistry*, 215(1):331 – 344, 1986.

[38] W. Donald, R. Leib, J. O'Brien, M. Bush, and E. Williams. Absolute standard hydrogen electrode potential measured by reduction of aqueous nanodrops in the gas phase. *Journal of the American Chemical Society*, 130(11):3371–3381, 2008.

[39] J.V. Coe. Fundamental properties of bulk water from cluster ion data. *International reviews in physical chemistry*, 20:58, 2001.

[40] M. D. Tissandier. The proton's absolute aqueous enthalpy and Gibbs free energy of solvation from cluster-ion solvation data. *The Journal of Physical Chemistry A*, 102:7794, 1998.

[41] D. Asthagiri. Absolute hydration free energies of ions, ion–water clusters, and quasichemical theory. *The Journal of Chemical Physics*, 119:2707, 2003.

[42] H. Neff and R. Kötz. Photoelectron spectroscopic study of emersed gold electrodes. *Journal of Electroanalytical Chemistry and Interfacial Electrochemistry*, 151(1):305 – 310, 1983.

[43] Z. Samec, B.W. Johnson, and K. Doblhofer. The absolute electrode potential of metal electrodes emersed from liquid electrolytes. *Surface Science*, 264(3):440 – 448, 1992.

[44] D. Cahen and A. Kahn. Electron energetics at surfaces and interfaces: Concepts and experiments. *Advanced Materials*, 15(4):271–277, 2003.

[45] Lord Kelvin G.C.V.O. D.C.L. LL.D. F.R.S. M.R.I. V. Contact electricity of metals. *The London, Edinburgh, and Dublin Philosophical Magazine and Journal of Science*, 46(278):82–120, 1898.

[46] W.A. Zisman. A new method of measuring contact potential differences in metals. *Review of Scientific Instruments*, 3(7):367–370, 1932.

[47] M. Rohwerder and F. Turcu. High-resolution Kelvin probe microscopy in corrosion science: Scanning Kelvin probe force microscopy (SKPFM) versus classical scanning Kelvin probe (SKP). *Electrochimica Acta*, 53(2):290 – 299, 2007.

[48] H.G. Yamins and W.A. Zisman. A new method of studying the electrical properties of monomolecular films on liquids. *The Journal of Chemical Physics*, 1(9):656–661, 1933.

[49] N.V. Alov. Fifty years of x-ray photoelectron spectroscopy. *Journal of Analytical Chemistry*, 60(3):297–300, Mar 2005.

[50] S. Hofmann. *Auger- and x-ray photoelectron spectroscopy in materials science: A user-oriented guide*. Springer Series in Surface Sciences. Springer Berlin Heidelberg, 2012.

[51] H. Hertz. *Phys*, 31:421–447, 1887.

[52] W. Hallwachs. On the effect of light on electrostatically charged bodies. *Ann. Phys*, 33:301–312, 1888.

[53] P. Lenard and M. Wolf. Zerstäuben der Körper durch das ultraviolette Licht. *Annalen der Physik*, 273(7):443–456, 1889.

[54] P. Lenard. The light electrical effect. *Ann Phys*, 8(5):149–198, 1902.

[55] A. Einstein. On a heuristic point of view about the creation and conversion of light. *Annalen der Physik*, 17(6):132–148, 1905.

[56] H.R. Robinson and C.L. Young. V. The influence of chemical state on critical x-ray absorption frequencies. *The London, Edinburgh, and Dublin Philosophical Magazine and Journal of Science*, 10(62):71–75, 1930.

[57] R. Steinhardt and E. Serfass. X-ray photoelectron spectrometer for chemical analysis. *Analytical Chemistry*, 23(11):1585–1590, 1951.

[58] K. Siegbahn and C. Nordling. ESCA, atomic, molecular and solid state structure studied by means of electron spectroscopy. *Nov. act. uppsaliensis*, 1967.

[59] R. Schlaf. Calibration of photoemission spectra and work function determination. Electrical Engineering Department University of South Florida. `http://rsl.eng.usf.edu/Documents/Tutorials/PEScalibration.pdf`. Accessed July 2019.

[60] K.D. Sevier. *Low Energy Electron Spectrometry*. Wiley, 1972.

[61] F. Hadjarab and J.L. Erskine. Image properties of the hemispherical analyzer applied to multichannel energy detection. *Journal of Electron Spectroscopy and Related Phenomena*, 36(3):227 – 243, 1985.

[62] D. Roy and D. Tremblay. Design of electron spectrometers. *Reports on Progress in Physics*, 53(12):1621–1674, dec 1990.

[63] J. Sitte. Relation between reference levels, work functions and contact potential differences in photoelectron spectroscopy. *Chemical Physics Letters*, 42(1):131 – 132, 1976.

[64] M.P. Seah, I.S. Gilmore, and S.J. Spencer. XPS: binding energy calibration of electron spectrometers 4-assessment of effects for different x-ray sources, analyser resolutions, angles of emission and overall uncertainties. *Surface and Interface Analysis*, 26(9):617–641, 1998.

[65] M.P. Seah and D. Briggs. Instrument calibration for AES and XPS. *Surface analysis by Auger and X-ray photoelectron spectroscopy*, pages 167–189, 2003.

[66] O.I. Klyushnikov. Method to determine the work function using x-ray photoelectron spectroscopy. *Journal of Structural Chemistry*, 39(6):944–947, Nov 1998.

[67] M.P. Seah and W.A. Dench. Quantitative electron spectroscopy of surfaces: A standard data base for electron inelastic mean free paths in solids. *Surface and Interface Analysis*, 1(1):2–11, 1979.

[68] A. Muñoz, J.C. Oller, F. Blanco, J.D. Gorfinkiel, P. Limão Vieira, and G. García. Electron-scattering cross sections and stopping powers in H_2O. *Phys. Rev. A*, 76:052707, Nov 2007.

[69] T. Majeed and D.J. Strickland. New survey of electron impact cross sections for photoelectron and auroral electron energy loss calculations. *Journal of Physical and Chemical Reference Data*, 26(2):335–349, 1997.

[70] D. Briggs and J.T. Grant. *Surface analysis by Auger and x-ray photoelectron spectroscopy*. Chichester IM Publications, 2003. Published by IM Publications and Surface Spectra Limited.

[71] F. Paschen. Über die zum Funkenübergang in Luft, Wasserstoff und Kohlensäure bei verschiedenen Drücken erforderliche Potentialdifferenz. *Annalen der Physik*, 273(5):69–96, 1889.

[72] IUPAC. Compendium of Chemical Terminology, 2nd ed. (the "Gold Book"). Compiled by A. D. McNaught and A. Wilkinson. *Blackwell Scientific Publications*, 1997.

[73] H. Ishii, K. Sugiyama, E. Ito, and K. Seki. Energy level alignment and interfacial electronic structures at organic/metal and organic/organic interfaces. *Advanced Materials*, 11(8):605–625, 1999.

[74] N.D. Lang and W. Kohn. Theory of metal surfaces: Charge density and surface energy. *Phys. Rev. B*, 1:4555–4568, Jun 1970.

[75] N.D. Lang and W. Kohn. Theory of metal surfaces: Work function. *Phys. Rev. B*, 3:1215–1223, Feb 1971.

[76] N.D. Lang and W. Kohn. Theory of metal surfaces: Induced surface charge and image potential. *Phys. Rev. B*, 7:3541–3550, Apr 1973.

[77] P. Kerger, D. Vogel, and M. Rohwerder. Electrochemistry in ultra-high vacuum: The fully transferable ultra-high vacuum compatible electrochemical cell. *Review of Scientific Instruments*, 89(11):113102, 2018.

[78] K. Jousten, W. Jitschin, F. Sharipov, and R. Lachenmann. *Wutz Handbuch Vakuumtechnik*. Vieweg + Teubner Praxis. Vieweg+Teubner Verlag, 2009.

[79] Pfeiffer Vacuum GmbH. Pfeiffer Vacuum GmbH, 2013.

[80] H. Rottländer, W. Umrath, and G. Voss. Leybold GmbH, 2016.

[81] S. Evers and M. Rohwerder. The hydrogen electrode in the "dry": A kelvin probe approach to measuring hydrogen in metals. *Electrochemistry Communications*, 24:85 – 88, 2012.

[82] K.W. Allen, D.R. Lewis, and K.G.A. Pankhurst. Adsorption of water vapour on palladium. *J. Chem. Soc. A*, pages 3028–3031, 1971.

[83] T. Imokawa, K.J. Williams, and G. Denuault. Fabrication and characterization of nanostructured pd hydride ph microelectrodes. *Analytical Chemistry*, 78(1):265–271, 2006. PMID: 16383336.

[84] D.D. Macdonald, P.R. Wentrcek, and A.C. Scott. The measurement of pH in aqueous systems at elevated temperatures using palladium

hydride electrodes. *Journal of the Electrochemical Society*, 127(8):1745–1751, 1980.

[85] T.A. Webster and E.D. Goluch. Electrochemical detection of pyocyanin in nanochannels with integrated palladium hydride reference electrodes. *Lab Chip*, 12:5195–5201, 2012.

[86] J.F.D Kelly, R.A. Goffe, and A.C.C. Tseung. Internally charged palladium hydride reference electrode: II Automatically controlled palladium hydride electrode. *Medical and Biological Engineering and Computing*, 19(3):333–339, 1981.

[87] R.A. Goffe and A.C. Tseung. Internally charged palladium hydride reference electrode—part 1: The effect of charging current density on long-term stability. *Medical and Biological Engineering and Computing*, 16(6):670–676, 1978.

[88] S. Evers, C. Senöz, and M. Rohwerder. Hydrogen detection in metals: a review and introduction of a kelvin probe approach. *Science and technology of advanced materials*, 14(1):014201, 2013.

[89] K.S. Kim, A.F. Gossmann, and N. Winograd. X-ray photoelectron spectroscopic studies of palladium oxides and the palladium-oxygen electrode. *Analytical Chemistry*, 46(2):197–200, 1974.

[90] E. Lundgren, G. Kresse, C. Klein, M. Borg, J.N. Andersen, M. De Santis, Y. Gauthier, C. Konvicka, M. Schmid, and P. Varga. Two-dimensional oxide on pd(111). *Phys. Rev. Lett.*, 88:246103, Jun 2002.

[91] D. Vijayshankar, T.H. Tran, A. Bashir, S. Evers, and M. Rohwerder. Hydrogen permeation as a tool for quantitative characterization of oxy-

gen reduction kinetics at buried metal-coating interfaces. *Electrochimica Acta*, 189:111 – 117, 2016.

[92] J.-N. Longchamp, T. Latychevskaia, C. Escher, and H.-W. Fink. Low-energy electron transmission imaging of clusters on free-standing graphene. *Applied Physics Letters*, 101(11):113117, 2012.

[93] R.S. Weatherup, B. Eren, Y Hao, H. Bluhm, and M.B. Salmeron. Graphene membranes for atmospheric pressure photoelectron spectroscopy. *The Journal of Physical Chemistry Letters*, 7(9):1622–1627, 2016. PMID: 27082434.

[94] S. Garaj, W. Hubbard, A. Reina, J. Kong, D. Branton, and J.A. Golovchenko. Graphene as a subnanometre trans-electrode membrane. *Nature*, 467(7312):190, 2010.

[95] J. Scott Bunch, S.S. Verbridge, J.S. Alden, A.M. van der Zande, J.M. Parpia, Harold G. Craighead, and P.L. McEuen. Impermeable atomic membranes from graphene sheets. *Nano Letters*, 8(8):2458–2462, 2008.

[96] Y. Gorlin, B. Lassalle-Kaiser, J.D. Benck, S. Gul, S.M. Webb, V.K. Yachandra, J. Yano, and T.F. Jaramillo. In situ x-ray absorption spectroscopy investigation of a bifunctional manganese oxide catalyst with high activity for electrochemical water oxidation and oxygen reduction. *Journal of the American Chemical Society*, 135(23):8525–8534, 2013.

[97] R. Jaeckel and B. Wagner. Photo-electric measurement of the work function of metals and its alteration after gas adsorption. *Vacuum*, 13(12):509 – 511, 1963.

[98] S. Trasatti. *Chim. Ind. Milan*, 53:559, 1972.

[99] S. Trasatti. Electronegativity, work function, and heat of adsorption of hydrogen on metals. *J. Chem. Soc., Faraday Trans. 1*, 68:229–236, 1972.

[100] S. Trasatti. Work function, electronegativity, and electrochemical behaviour of metals: Iii. electrolytic hydrogen evolution in acid solutions. *Journal of Electroanalytical Chemistry and Interfacial Electrochemistry*, 39(1):163 – 184, 1972.

[101] H. Conrad, G. Ertl, and E.E. Latta. Adsorption of hydrogen on palladium single crystal surfaces. *Surface Science*, 41(2):435 – 446, 1974.

[102] B.E. Nieuwenhuys, R. Bouwman, and W.M.H. Sachtler. The changes in work function of group Ib and VIII metals on xenon adsorption, determined by field electron and photoelectron emission. *Thin Solid Films*, 21(1):51 – 58, 1974.

[103] R. Schlaf, H. Murata, and Z.H. Kafafi. Work function measurements on indium tin oxide films. *Journal of Electron Spectroscopy and Related Phenomena*, 120(1):149 – 154, 2001.

[104] J.C. Riviere. *Solid States Surface Science*, volume 1, edited by M. Green, M. Dekker, New York, NY, USA. 1969.

[105] A.M. Bradshaw and F.M. Hoffmann. The chemisorption of carbon monoxide on palladium single crystal surfaces: IR spectroscopic evidence for localised site adsorption. *Surface Science*, 72(3):513 – 535, 1978.

[106] V.V. Kaichev, I.P. Prosvirin, Valerii I. Bukhtiyarov, H. Unterhalt, G. Rupprechter, and H.-J. Freund. High-pressure studies of

CO adsorption on Pd(111) by x-ray photoelectron spectroscopy and sum-frequency generation. *The Journal of Physical Chemistry B*, 107(15):3522–3527, 2003.

[107] F. Solymosi, A. Erdöhelyi, and M. Lancz. Surface interaction between H_2 and CO_2 over palladium on various supports. *Journal of Catalysis*, 95(2):567 – 577, 1985.

[108] J.B. Heywood. Pollutant formation and control in spark-ignition engines. In *Energy and Combustion Science*, pages 229 – 258. Pergamon, 1979.

[109] *CasaXPS Software, Version 2.3.19PR1.0.* Casa Software Ltd., 2018.

[110] M. Oku and K. Hirokawa. XPS observation of $Fe_{1-x}O$ at temperatures between 25 and 800 $°C$. *Journal of Applied Physics*, 50(10):6303–6308, 1979.

[111] N.S. McIntyre and D.G. Zetarukr. X-ray photoelectron spectroscopic studies of iron oxides. *Analytical Chemsitry*, 49(11):1521 – 1529, 1977.

[112] M. Descostes, F. Mercier, N. Thromat, C. Beaucaire, and M. Gautier-Soyer. Use of XPS in the determination of chemical environment and oxidation state of iron and sulfur samples: constitution of a data basis in binding energies for Fe and S reference compounds and applications to the evidence of surface species of an oxidized pyrite in a carbonate medium. *Applied Surface Science*, 165(4):288 – 302, 2000.

[113] A.P. Grosvenor, B.A. Kobe, M.C. Biesinger, and N.S. Mc Intyre. Investigation of multiplet splitting of Fe 2p XPS spectra and bonding

in iron compounds. *Surface and Interface Analysis*, 36(12):1564–1574, 2004.

[114] T. Yamashita and P. Hayes. Analysis of XPS spectra of Fe^{2+} and Fe^{3+} ions in oxide materials. *Applied Surface Science*, 254(8):2441 – 2449, 2008.

[115] H.J.T. Ellingham. Transactions and communications. *Journal of the Society of Chemical Industry*, 63(5):125–160, 1944.

[116] E.A. Gulbransen and R. Ruka. Kinetics of solid phase reactions in oxide films on iron — the reversible transformation at or near 570°c. *JOM*, 2(12):1500–1508, Dec 1950.

[117] A.J. Pignocco and G.E. Pellissier. Low-energy electron diffraction studies of oxygen adsorption and oxide formation on a (001) iron surface. *J. Electrochem. Soc.*, 112(12):1188 – 1194, 1965.

[118] A.J. Pignocco and G.E. Pellissier. Leed studies of oxygen adsorption and oxide formation on an (011) iron surface. *Surface Science*, 7(3):261 – 278, 1967.

[119] J.F. Moulder, W.F. Stickle, P.E. Sobol, and K.D. Bomben. *Handbook of X-ray Photoelectron Spectroscopy*. ULVAC-PHI, Inc, 1995.

[120] I.S. Molchan, G.E. Thompson, P. Skeldon, R. Lindsay, J. Walton, E. Kouvelos, G.E. Romanos, P. Falaras, A.G. Kontos, M. Arfanis, E. Siranidi, L.F. Zubeir, M.C. Kroon, J. Klöckner, B. Iliev, and T.J.S. Schubert. Microscopic study of the corrosion behaviour of mild steel in ionic liquids for CO_2 capture applications. *RSC Adv.*, 5:35181–35194, 2015.

[121] *CasaXPS Manual*. Casa Software Ltd., 2009.

[122] J. Tafel. Über die Polarisation bei kathodischer Wasserstoffentwicklung. *Zeitschrift für physikalische Chemie*, 50(1):641–712, 1905.

[123] T. Erdey-Grúz and M. Volmer. Zur Theorie der Wasserstoff Überspannung. *Zeitschrift für physikalische Chemie*, 150(1):203–213, 1930.

[124] A. Frumkin. Wasserstoffüberspannung und Struktur der Doppelschicht. *Zeitschrift für physikalische Chemie*, 164(1):121–133, 1933.

[125] A. Frumkin. Remarks on the theory of over-voltage. *Acta physicochim. URSS*, 7:475, 1937.

[126] R. Kirchheim. Hydrogen solubility and diffusivity in defective and amorphous metals. *Progress in Materials Science*, 32(4):261 – 325, 1988.

[127] C. Senöz, S. Evers, M. Stratmann, and M. Rohwerder. Scanning Kelvin Probe as a highly sensitive tool for detecting hydrogen permeation with high local resolution. *Electrochemistry Communications*, 13(12):1542 – 1545, 2011.

[128] R. Dus, E. Nowicka, and R. Nowakowski. The response of work function of thin metal films to interaction with hydrogen. *Acta Physica Polonica A*, 114, 12 2008.

[129] T.C. Leung, C.L. Kao, W.S. Su, Y.J. Feng, and C.T. Chan. Relationship between surface dipole, work function and charge transfer: Some exceptions to an established rule. *Phys. Rev. B*, 68:195408, Nov 2003.

[130] J.D. Jackson. *Classical Electrodynamics*. Wiley: New York, 1975.

[131] F. Gossenberger, T. Roman, K. Forster-Tonigold, and A. Gross. Work function change of platinum electrodes induced by halide ad-1 sorption. 2013.

[132] R.J. Behm, K. Christmann, and G. Ertl. Adsorption of hydrogen on Pd(100). *Surface Science*, 99(2):320 – 340, 1980.

[133] W. Dong, V. Ledentu, P. Sautet, A. Eichler, and J. Hafner. Hydrogen adsorption on palladium: a comparative theoretical study of different surfaces. *Surface Science*, 411(1):123 – 136, 1998.

[134] P.K. Schmidt, K. Christmann, G. Kresse, J. Hafner, M. Lischka, and A. Gross. Coexistence of atomic and molecular chemisorption states. *Phys. Rev. Lett.*, 87:096103, Aug 2001.

[135] M. Lischka and A. Groß. Hydrogen on palladium: A model system for the interaction of atoms and molecules with metal surfaces. *Recent Developments in Vacuum Science and Technology*, 37(661):2, 2003.

[136] R. Suhrmann. Neue Untersuchungen zum Palladium-Wasserstoff-Problem. *The Science of Nature*, 46(21):600, 1959.

[137] U. Muschiol, P.K. Schmidt, and K. Christmann. Adsorption and absorption of hydrogen on a palladium (210) surface: a combined LEED, TDS, $\Delta\Phi$ and HREELS study. *Surface science*, 395(2-3):182–204, 1998.

[138] S. Axnanda, M. Scheele, E. Crumlin, B. Mao, R. Chang, S. Rani, M. Faiz, S. Wang, A. Alivisatos, and Z. Liu. Direct work function measurement by gas phase photoelectron spectroscopy and its application on PbS nanoparticles. *Nano Letters*, 13(12):6176–6182, 2013.

[139] S. Axnanda, E.J. Crumlin, B. Mao, S. Rani, R. Chang, P.G. Karlsson, M.O.M. Edwards, M. Lundqvist, R. Moberg, P. Ross, et al. Using "tender" x-ray ambient pressure x-ray photoelectron spectroscopy as a direct probe of solid-liquid interface. *Scientific reports*, 5:9788, 2015.

[140] J. Cerdá, A. Michaelides, M.L. Bocquet, P.J. Feibelman, T. Mitsui, M. Rose, E. Fomin, and M. Salmeron. Novel water overlayer growth on Pd(111) characterized with scanning tunneling microscopy and density functional theory. *Phys. Rev. Lett.*, 93:116101, Sep 2004.

[141] M. Eigen, K. Kustin, and G. Maass. Die Geschwindigkeit der Hydratation von SO_2 in wäßriger Lösung. *Z. Phys. Chem.*, 30:130–136, 1961.

[142] K.S. Johnson. Carbon dioxide hydration and dehydration kinetics in seawater. *Limnology and Oceanography*, 27(5):849–855, 1982.

[143] H.T. Byck. Effect of dissolved CO_2 on the pH of water. *Science*, 75(1938):224–224, 1932.

[144] A.F. Hofmann, F.J.R. Meysman, K. Soetaert, and J.J. Middelburg. A step-by-step procedure for pH model construction in aquatic systems. *Biogeosciences*, 5(1):227–251, 2008.

[145] H.S. Harned and R. Davis Jr. The ionization constant of carbonic acid in water and the solubility of carbon dioxide in water and aqueous salt solutions from 0 to 50. *Journal of the American Chemical Society*, 65(10):2030–2037, 1943.

[146] H.S. Harned and Samuel R. Scholes Jr. The ionization constant of HCO_3-from 0 to 50. *Journal of the American Chemical Society*,

63(6):1706–1709, 1941.

[147] J.A. Dean and N.A. Lange. *Lange's Handbook of Chemistry*, volume 13. McGraw-Hill, 1985.

[148] Y. Hori. *Electrochemical CO_2 Reduction on Metal Electrodes*, pages 89–189. Springer New York, New York, NY, 2008.

[149] D.M. Ruthven and R.S. Upadhye. The catalytic decomposition of aqueous formic acid over suspended palladium catalysts. *Journal of Catalysis*, 21(1):39 – 47, 1971.

[150] N. Kruse, M. Rebholz, and J.H. Block. Studien zum Methanol-Zerfall an Palladium. *Chemie Ingenieur Technik*, 63(6):615–618, 1991.

[151] N. Aas and M. Bowker. Adsorption and autocatalytic decomposition of acetic acid on Pd(110). *J. Chem. Soc., Faraday Trans.*, 89:1249–1255, 1993.

[152] M. Bowker, C. Morgan, and J. Couves. Acetic acid adsorption and decomposition on Pd(110). *Surface Science*, 555(1):145 – 156, 2004.

[153] M. Borasio, O. Rodríguez de la Fuente, G. Rupprechter, and H.-J. Freund. In Situ Studies of Methanol Decomposition and Oxidation on Pd(111) by PM-IRAS and XPS Spectroscopy. *The Journal of Physical Chemistry B*, 109(38):17791–17794, 2005.

[154] R. Kortlever, J. Shen, K.J.P. Schouten, F. Calle-Vallejo, and M.T.M. Koper. Catalysts and reaction pathways for the electrochemical reduction of carbon dioxide. *The Journal of Physical Chemistry Letters*, 6(20):4073–4082, 2015.

[155] NIST x-ray photoelectron spectroscopy database, NIST standard reference database number 20. *National Institute of Standards and Technology*, retrieved 20.08.2019.

[156] J.-J. Chen, Z.-C. Jiang, Y. Zhou, B.R. Chakraborty, and N. Winograd. Spectroscopic studies of methanol decomposition on Pd[lcub]111[rcub]. *Surface Science*, 328(3):248 – 262, 1995.

[157] F. Solymosi and K. Révész. Spectroscopic study on the adsorption and dissociation of CH3I on Pd(100): thermal and photo effects. *Surface Science*, 280(1):38 – 49, 1993.

[158] R.J. Levis, J. Zhicheng, and N. Winograd. Thermal decomposition of methanol absorbed on palladium{111}. a new reaction pathway involving methyl formation. *Journal of the American Chemical Society*, 111(13):4605–4612, 1989.

[159] G. Illing, D. Heskett, E.W. Plummer, H.-J. Freund, J. Somers, T. Lindner, A.M. Bradshaw, U. Buskotte, M. Neumann, and et al. Starke. Adsorption and reaction of CO_2 on Ni{110}: X-ray photoemission, near-edge x-ray absorption fine-structure and diffuse leed studies. *Surface Science*, 206(1-2):1–19, 1988.

[160] H. Hoffmann, F. Zaera, R.M. Ormerod, R.M. Lambert, J.M. Yao, D.K. Saldin, L.P. Wang, D.W. Bennett, and W.T. Tysoe. A near-edge x-ray absorption fine structure and photoelectron spectroscopic study of the structure of acetylene on Pd(111) at low temperature. *Surface Science*, 268(1):1 – 10, 1992.

[161] F. Solymosi, A. Berkó, and Z. Tóth. Adsorption and dissociation of

CH_3OH on clean and K-promoted Pd(100) surfaces. *Surface Science*, 285(3):197 – 208, 1993.

[162] H. Onishi, C. Egawa, T. Aruga, and Y. Iwasawa. Adsorption of Na atoms and oxygen-containing molecules on MgO(100) and (111) surfaces. *Surface Science*, 191(3):479 – 491, 1987.

[163] S.L. Stipp and M.F. Hochella. Structure and bonding environments at the calcite surface as observed with x-ray photoelectron spectroscopy (XPS) and low energy electron diffraction (LEED). *Geochimica et Cosmochimica Acta*, 55(6):1723 – 1736, 1991.

[164] U. Gelius, P.F. Hedén, J. Hedman, B.J. Lindberg, R. Manne, R. Nordberg, C. Nordling, and K. Siegbahn. Molecular spectroscopy by means of ESCA III. carbon compounds. *Physica Scripta*, 2(1-2):70–80, 1970.

[165] L. Pedocchi, M.R. Ji, S. Lizzit, G. Comelli, and G. Rovida. CO adsorption on Pd: An XPS and density functional approach. *Journal of Electron Spectroscopy and Related Phenomena*, 76:383 – 387, 1995.

[166] E.J.W. Verwey. Cation arrangement in a few oxides with crystal structures of the spinel type. *Recueil des Travaux Chimiques des Pays-Bas*, 55(6):531–540, 1936.

[167] J.M. Daniels and A. Rosencwaig. Mössbauer spectroscopy of stoichiometric and non-stoichiometric magnetite. *Journal of Physics and Chemistry of Solids*, 30(6):1561 – 1571, 1969.

[168] F.C. Voogt, T. Hibma, G.L. Zhang, M. Hoefman, and L. Niesen. Growth and characterization of non-stoichiometric magnetite $Fe_{3-\delta}O_4$

thin films. *Surface Science*, 331-333:1508 – 1514, 1995. Proceedings of the 14th European Conference on Surface Science.

[169] M. Pourbaix. Atlas of electrochemical equilibria in aqueous solutions. *NACA*, 1974.

[170] S.C. Pang, S.F. Chin, and Marc A.A. Redox equilibria of iron oxides in aqueous-based magnetite dispersions: Effect of pH and redox potential. *Journal of Colloid and Interface Science*, 311(1):94 – 101, 2007.

[171] R.M. Hazen and R. Jeanloz. Wüstite (Fe1-x O): A review of its defect structure and physical properties. *Reviews of Geophysics*, 22(1):37–46, 1984.

[172] M.A.V. Devanathan and Z. Stachurski. The adsorption and diffusion of electrolytic hydrogen in palladium. *Proceedings of the Royal Society of London. Series A, Mathematical and Physical Sciences*, 270(1340):90–102, 1962.

[173] M. Polanyi. Bildung und Zerfall von Molekülen. *The European Physical Journal A*, 33(1):429–434, 1925.

[174] R.G. Musket. Effects of contamination on the interaction of hydrogen gas with palladium: A review. *Journal of the Less Common Metals*, 45(2):173 – 183, 1976.

[175] H. Sakai, T. Nakajima, N. Yoshida, and S. Kishimoto. Poisoning effect of carbon monoxide on the desorption process of hydrogen from palladium. *Reaction Kinetics and Catalysis Letters*, 19(3):297–301, 1982.

[176] Brian D.A. and Aicheng C. The role of palladium in a hydrogen economy. *Materials Today*, 14(6):282 – 289, 2011.

[177] P.A. Thiel and T.E. Madey. The interaction of water with solid surfaces: Fundamental aspects. *Surface Science Reports*, 7(6-8):211–385, 1987.

[178] A.J. Bard. *Standard Potentials in Aqueous Solution*. CRC Press, 2017.

Curriculum Vitae

Personal Information

Name	Philipp Kerger
Email	kerger@mpie.de

Education

2014–today	PhD-student, mechanical engineering, Ruhr Universität Bochum Thesis: *"Absolute Electrode Potentials–The Thin Film Electrode"*
2017	Affiliate, Lawrence Berkeley National Laboratory, Advanced Light Source, USA CA, 6 month
2014–today	Pre-doctoral research fellow of the Max-Planck-Institut für Eisenforschung GmbH, department of Interface Chemistry and Surface Engineering, off-site doctorate
2012	Intern, Airbus Helicopters (Eurocopter Group), 3 months
2011	Doctoral program: Introduction to FEM simulations; Synthesis and characterization of materials, Saarland University
2011	Intern, Leffer GmbH & Co. KG, 6 weeks
2010–2014	Student Assistant, Prof. Dr. Vehoff, later Prof. Dr. mont. Motz, Saarland University
2007–2014	Student of Materials Science and Engineering at Saarland University Thesis: *"Analyse des Kornwachstums von PED-Nickel: Experiment, Theorie, Simulation"* Thesis: *"Zur Wärmbehandlung an gepulstem, elektrodeponiertem, nanokristallinem Nickel und dem möglichen Einfluss von Partikeln einer zweiten Phase"*
1999–2007	A Level, Baccalauréat Deutsch-Französisches Gymnasium Saarbrücken

Languages

German	Mother tongue
French	Fluent (full working proficiency)
English	Fluent (full working proficiency)

Publications

2018 P. Kerger, D. Vogel, and M. Rohwerder. Electrochemistry in ultra-high vacuum: The fully transferrable ultra-high vacuum compatible electrochemical cell. *Review of Scientific Instruments*, 2018

2018 A. Altin, M. Krzywiecki, A. Sarfraz, C. Toparli, C.A. Laska, P. Kerger, A. R. Žeradjanin, K.J.J. Mayrhofer, M. Rohwerder, and A. Erbe. Cyclodextrin inhibits zinc corrosion by destabilizing point defect formation in the oxide layer. *Angewandte Chemie International Edition*, 2018

2017 A.R. Head, O. Karslıoğlu, T. Gerber, Y. Yu, L. Trotochaud, J. Raso, P. Kerger, and H. Bluhm. CO adsorption on Pd(100) studied by multimodal ambient pressure x-ray photoelectron and infrared reflection absorption spectroscopies. *Surface Science*, 2017

2016 S.K. Kato, S. Matam, P. Kerger, L. Bernard, C. Battaglia, D. Vogel, M. Rohwerder, and A. Züttel. The origin of the catalytic activity of a metal hydride in CO_2 reduction. *Angewandte Chemie International Edition*, 2016

2015 P. Kerger, D. Rathmann, M. Marx, and C. Motz. How to produce a desired bimodal microstructure for optimized mechanical properties: Investigation of the mechanisms of abnormal grain growth in pulsed electro-deposited nickel. *International Journal of Materials Research*, 2015

Presentations

2019 P. Kerger, D. Vogel, and M. Rohwerder. Electrochemistry in UHV and ambient conditions. In-Situ Analytik, Jülich Forschungszentrum, Germany, 2019 (invited)

2018 O. Karslıoğlu, A.R. Head, J. Raso, T. Gerber, Y. Yu, L. Trotochaud, P. Kerger, and H. Bluhm. CO+NO+O_2 Reaction on Pd(100): New insights from APXPS. 5th Annual Ambient Pressure X-ray Photoelectron Spectroscopy Workshop, Berlin Germany, 2018

2018 K. Schweinar, S. Beeg, P. Kerger, C. Corrêa da Silva, J. Cao, M. Amati, L. Gregoratti, P. Zeller, and D. et al Schlögl, R.; Raabe. Correlative atom probe tomography and in-situ scanning photoemission electron microscopy applied to catalytically active materials. Atom Probe Tomography and Microscopy, Gaitherburg, USA, 2018

2017 P. Kerger, D. Vogel, and M. Rohwerder. Liquid thin film electrode in UHV and under ambient pressure conditions. 4th Annual Ambient Pressure X-ray Photoelectron Spectroscopy Workshop, Shanghai, China, 2017

2016 P. Kerger, D. Vogel, and M. Rohwerder. Using a novel in-situ/operando chemical cell to investigate surface reactions such as the reduction of oxygen and surface oxides. 11th International Symposium on Electrochemical Micro and Nanosystem Technologies, Brussels, Belgium, 2016

2016 P. Kerger, D. Vogel, and M. Rohwerder. Using a novel in-situ/operando chemical cell to investigate surface reactions such as the reduction of oxygen and surface oxides. AVS 63rd International Symposium Exhibition, Nashville, USA, 2016

Petty Patent

2016 P. Kerger and M. Rohwerder. Electrochemical in-situ/operando-cell for multi-purpose analyses. 20 2016 104 543, 2016